A Thesis Submitted for the Degree of PhD at the University of Warwick

Permanent WRAP URL:

http://wrap.warwick.ac.uk/80148

Copyright and reuse:

This thesis is made available online and is protected by original copyright.

Please scroll down to view the document itself.

Please refer to the repository record for this item for information to help you to cite it.

Our policy information is available from the repository home page.

For more information, please contact the WRAP Team at: wrap@warwick.ac.uk

warwick.ac.uk/lib-publications
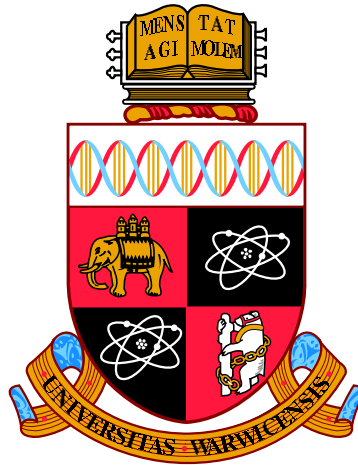
Simulating Collective Motion from Particles to Birds

by

Adam Morrison Miller

Thesis

Submitted to the University of Warwick

for the degree of

Doctor of Philosophy

Physics and Complexity Science

August 2015

THE UNIVERSITY OF
WARWICK

Contents

Acknowledgments

My heartfelt thanks go to the friends I've made over my time at Warwick. In particular Mike Irvine (for making me laugh so hard I cried), Jamie Harris (for sharing my love of golf and pub quizzes), Peter Dawson (ditto), Ben Collyer, Dan Sprague and Mike Maitland plus the wider Compexity community. More thanks go to all those I have shared an office with, for brightening up my days:

Year 1 Mike Irvine, Dan Peavoy and Martine

Year 2 Mike Irvine, Mike Maitland, and occasionally Marcus Ong

Year 3 Mike Irvine, Mike Maitland, Liz Buckingham Jeffrey and Diana Khoromskaia

Year 4 Mike Irvine, Ben Collyer, Dan Sprague and Alistair Tucker

You all made my time here very special, if not exactly enjoyable. Of course, a considerable amount of thanks go to my partner Katie, without whom I would never have come even this far (by refusing to let me quit without handing something in). This thesis was typeset with $\LaTeX 2_\varepsilon$[1] by the author.

Declarations

The computer models this work is based on were entirely coded by me. The 3D flocking simulation is based on a 2D model of Pearce et al. [2014], which was developed for 3D by me (i.e. all geometric and integration algorithms, either designed or selected by me and what was meant by the 3D analogue). Some of the 3D flocking results appear in that paper. The analysis of the 3D work was done in collaboration with Matthew Turner (my PhD supervisor). The 2D 2-step flocking models were entirely devised, implemented and analyzed by me. The photothermothoresis simulation code of a model developed in collaboration with Matthew Turner, was written by me with guidance from Arran Tamsett based on his continuum model.

Abstract

The main work of this thesis is the construction of a 3D computer model of animal flocking based on vision. The model took an additional input, to those usually considered in tradition models: the projection of all other flock members on to an individual's field of view. Making 2D models is easy (in fact 4 new ones are included in this thesis), but we should be drawing parallels with experimental data for behaviour in animal systems and we should be cautious indeed when drawing conclusions, based on those models. It is common in the literature not to compare model behaviours with measurable quantities of natural flocks. However this work makes a concerted effort to do so in the case of the 3D model. A direct comparison was made in this work between the simulations and an empirical study of starling flocks, of the scaling behaviour of the maximum distance through the flock and the number of flock members, for which the agreement was very good. Other flock properties were compared with the natural flocks, but with less satisfactory results. A careful literature survey was made to investigate and ultimately support the biological plausibility of the 3D projection model. Biological and physiological plausibility is a factor not often considered by computational modellers. A series of novel and related 2D computer flocking models were investigated with hopes to find a single flocking rule that could manifest the most important features of collective motion and thereby be highly parsimonious. The final part of this thesis concerns a 2D computer model of photothermophoresis based on langevin dynamics, which it may be possible to use to find evidence of a density transition found in the continuum model. There was some evidence that a transition from a transparent diffuse state to an opaque compact one may exist for the discrete particle simulation.

Chapter 1

Introduction

1.1   Modelling in Biology

To paraphrase Sumpter, there are two approaches to modelling biological phenomena, functional and mechanistic [Sumpter, 2010]. To take a mechanistic approach is to ask *how* do these organisms *do* something. To take a functional approach is to ask *why*. In the case of flocking behaviours there are many theories as to the why and also as to the how. In this work the focus is mainly on the *how*, but it is important to think about the *why*, as understanding the function of a behaviour can be informative as to how the behaviour is produced. What we are looking for when constructing models are the behavioural rules that result in an organizational effect (characteristic of the swarm) [Parrish et al., 2002]. Hence most models of swarming avoid the details of the biomechanics of the individual's movements and the effects of the surrounding medium and instead deals with a series of movement *decisions* made at discrete points in time. These decisions are made based on behavioural rules and it is these behavioural rules that we would like to determine, by inference from observed behaviour.

1.2   Collective Behaviour in Nature

The natural world is teeming with examples of collective behaviour and in particular collective motion. The flocking of birds, swarming of fish, the marching of locusts and
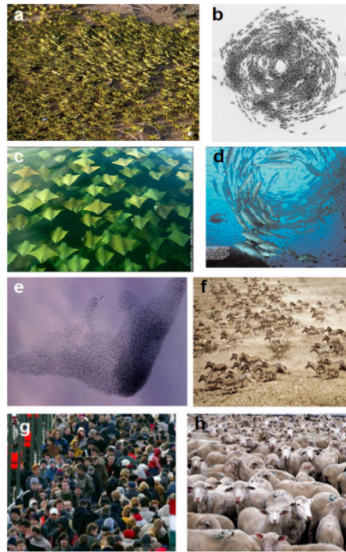
Figure 1.1: The natural world is teeming with examples of collective motion. a) marching wingless locusts, b) rotating army ants, c) a 3D array of golden rays, d) a fish vortex, e) starlings avoiding a predatory bird, f) a zebra herd, g) self-organized human 'traffic lanes', h) stationary sheep with alignment interactions. Taken from Vicsek and Zafeiris [2012].

the dynamics of crowds have all attracted the attention of investigators [Ballerini et al., 2008a; Faria et al., 2010; Buhl et al., 2006; Helbing and Molnár, 1995]. A recent review of investigations into natural collective motion, covering experiments, methods, models and simulations has been given by Vicsek and Zafeiris [2012].

Animal swarms fall into a category of physical systems called 'Active Matter'. They are active in the sense that they are driven by an internal store of energy that they convert into locomotion, i.e. they are self-propelled particles. Agent-based models from Reynolds boids model and, in the physics literature, starting with Vicsek's self-propelled particle model onwards, have proven popular methods of investigating the rules governing collective motion [Reynolds, 1987; Vicsek et al., 1995]. These models focus on the rules governing the motions of individuals acting autonomously, but responding in such a way as to exhibit collective motion (which is an emergent property). When designing such models, rules are formulated to reproduce observed properties of flocks. There are many aspects of the observed collective behaviours that could be used to form models, including positional preferences for neighbours and behavioural matching (aka allelomimesis), most noticeable in highly aligned orientations of neighbouring individuals in translating flocks.

There are at least two possible levels of behaviour that give rise to movement rules:

1. Behaviours with an immediate benefit to the individual that modify position with regards to neighbours, such as collision avoidance, or reduced exposure to predators.

2. Behaviours that benefit the group as a whole but do not necessarily improve the individual's position.

These individual level behaviours are encoded into models typically by using three types of rules:

- Alignment: individuals align with their neighbours.

- Cohesion (or attraction): individuals are attracted to nearby flock-mates.

- Separation (or repulsion): individuals avoid collision with nearby flock-mates.

These rules are often included together in models and may have different domains of effect, such as in Reynold's or Couzin's models [Reynolds, 1987; Couzin et al., 2002], or they may have a functional dependence on distance, i.e. $f_{ij}(r)$ [Grégoire et al., 2003; Mogilner et al., 2003].

The idea of 'neighbours' is very important, particularly for the alignment interaction. It is considered that individuals respond only to nearby or 'neighbouring' flock-mates to determine their headings at the next moment. Neighbours can be defined as those flock members within a certain distance of a focal individual. It may not be obvious, but we actually need to define what we mean by distance.

A brief note on terminology is that it has become common to refer to 'metric' and 'topological' distances in the literature. This can be confusing as both of these are metrics in a mathematical sense. A 'metric' interaction here, is purely a function of distance, e.g. two particles interact if they are within a fixed radius. In contradistinction, a 'topological' interaction does not depend exclusively on the distances involved, but on some geometrical criterion, e.g. one particle interacts with another if the other is less than the fourth nearest neighbour (not necessarily a symmetric relationship). This topological definition says nothing about the absolute distances between the two particles, but only how the particles are located in space relative to other particles.

Following Vicsek and Reynolds, alignment has typically been introduced via the velocity update rule for an individual, by taking an average over their neighbours' velocities. The neighbourhood has usually been through a metric distance, which is an

additional model parameter and without biological foundation. Ballerini et al. [2008a] found that a topological as opposed to a metric distance, provides a more appropriate definition of neighbour for their empirical data and therefore the Voronoi diagram (a topological construction) was used to determine neighbour relationships in this study.

Cohesion has generally been approached differently in the physics literature, although it can be implemented as 'move towards your neighbours if you are within a given radius' in the Reynolds style. In many cases cohesion has been induced by introducing an attractive potential between particles, which is a physicist's approach, but does not reflect a likely biological mechanism and assumes an interaction that varies with distance. Without a cohesive term, model flocks tend to disperse over time unless they are confined by boundary conditions which fixes the average density.

Separation can be enforced by a repulsive zone generated by repulsive short-range potentials. This is again an ad hoc approach which produces a desired biological effect, but with an implausible mechanism. Separation is important as it prevents overcrowding and collisions. If models have both an attractive and repulsive force, this leads to a potential well which fixes the flock density for all flock sizes as distances are then around the potential minimum. It is known however that density decreases with flock size for starlings as shown in Ballerini et al. [2008a].

Models can have different zones of interaction for alignment, cohesion and separation such as Reynold's original model and others e.g. Couzin et al. [2002]. Typically zones of repulsion are close to the focal individual, followed by the zone of alignment and then at the furthest distance a zone of attraction – to prevent flock dissipation. These models are simulated in discrete time and a mathematical description for the velocity update rule for individual i of n flock members, in these 'physicists' models' is:

$$\vec{v}_i = \phi_{\mathrm{a}} \left\langle \vec{v}(t) \right\rangle_{n_a} + \frac{1}{n} \sum_{j=1}^{n_{\mathrm{in}}} f_{ij} \frac{\vec{r}_{ij}(t)}{|\vec{r}_{ij}(t)|} + \phi_{\mathrm{e}} \vec{\eta}_i(t) \tag{1.1}$$

where $\left\langle \vec{v}(t) \right\rangle_{n_a}$ is the average velocity over the n_a neighbours in the alignment effect's range (to be defined later) and f_{ij} are repulsive or attractive dependent on which zone individual j is located in relation to individual i. $\vec{\eta}_i(t)$ is a noise vector, which approximates imperfect perception and decisions in biological agents. ϕ_{a}, ϕ_{e} are control parameters for the relative proportions of the alignment and noise terms. n_{in} the number of particles within the maximum interaction zone radius. The strengths of the interaction forces f_{ij} can vary depending on not just the distance, but also the angle, as there is a blind angle at the rear for fish and birds.
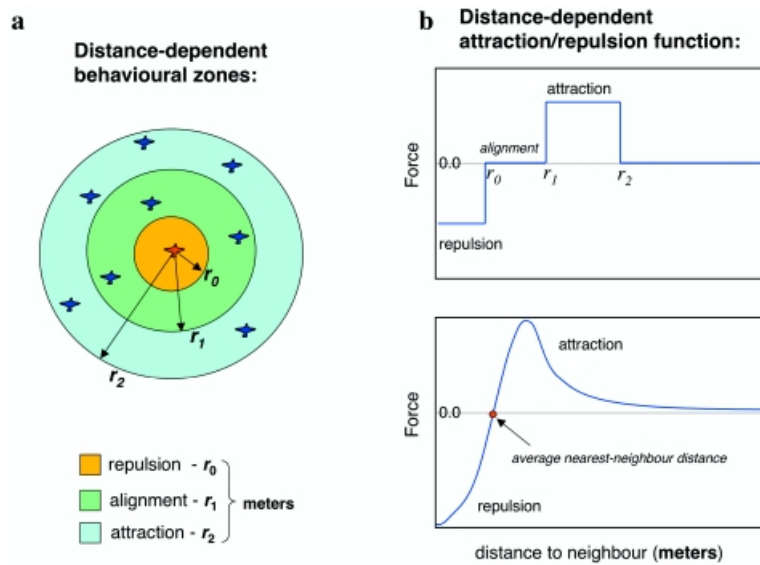
Figure 1.2: Interaction zones in typical flocking models [Giardina, 2008]. Force based models of flocking often have different sized zones of repulsion, alignment and attraction (a). It is thought that repulsion reflects collision avoidance and this is only necessary at close range and that attraction occurs between flock members at larger distances (to prevent the flock breaking up) and alignment to occur at intermediate distances. Of course these ranges can be adjusted depending on what biological system is being modelled. b) An example force profile and the effect it has on the distance to neighbouring individuals.

Agent-based models do not yield analytical solutions, however theoretical work has been done on continuum models. A continuum approximation approximating a flock as a fluid could be considered drastic as most biological flocks are on the macroscale or the mesoscale and individuals are not point particles (thereby excluding volume) this was the approach of Toner and Tu [1998]. Another theoretical approach has been to use statistical mechanics to investigate properties such as the flock order (the physics of spin systems has considerable analogies with this problem) [Tanner et al., 2003b,a]. An interesting theoretical model due to Tanner, represents flocks as networks (using a Delaunay triangulation) and information diffuses through the network described by the graph Laplacian (the network analogue of the diffusion operator). Tanner uses this model to prove that a Delaunay connected flock can remain connected in time with a very simple rule for maintaining distance. Ginelli and Chate [2010] found essentially the same result through simulation of a flock using a Delaunay triangulation neighbourhood for the alignment interaction. The flock size grew with time, due to the lack of a cohesion term in the model, but unlike with a metric interaction, the flock never became disconnected.

1.2.1   Starlings and STARFLAG

This work focuses on the common European starling (sturnus vulgaris) as an archetypal flocking animal. Starlings are famous for their 'murmurations'. These are aerial displays that can contain tens of thousands of birds and are visually very impressive, forming complex and ever changing shapes. Particularly large murmurations happen outside of the breeding season. They form just before dusk and last about half an hour. During which the thousands of starlings fly around the breeding site in huge flocks that change shape and density, with intermittent splitting and recombining of the flock. The display ends with the starlings roosting in trees for the night.

One reason for this focus is the STARFLAG project - a European Union funded project to record the positions of individuals in large starling flocks. From this recorded data, various measures were extracted, such as density and nearest neighbour distribution and anisotropy which are useful for comparisons with agent-based models [Cavagna et al., 2008b,a]. They used a trifocal stereography technique, i.e. a 3-camera setup to obtain the position data. The technique itself was not novel, but the algorithms to solve the correspondence problem between images of each bird (often obscured behind other birds) were [Cavagna et al., 2008b]. The two stereocameras were set 25 m apart on the base line, as illustrated in fig. 1.4. The set-up could achieve, with two targets at

Figure 1.3: The European starling *sternus vulgaris*, whose murmurations were the focus of the EU STARFLAG project.

a distance of $100\,\mathrm{m}$ from the baseline (a typical measurement distance) and a relative distance of $1\,\mathrm{m}$, an accuracy of $\pm 0.04\,\mathrm{m}$ on the relative distance, which is below 5% [Ballerini et al., 2008b].

1.2.2   Empirical Studies

A question that is of central importance in the study of flocking behaviours is "Is the nature of the interaction short or long ranged". The focus up until recently was on short range interactions Sumpter [2010]. However Pearce et al. [2014] studied the role of projection in control of bird flocks, there we suggested a long distance interaction to be responsible for flock cohesion (see chapter 2). In the case of starlings, members of the STARFLAG group have tried to address this question from their experimental positional data for starling flocks. They reported in Ballerini et al. [2008a] that the anisotropy in the angular distribution of nearest neighbours decays over a short range and the distribution is essentially uniform after approximately the 7th nearest neighbour The interaction cutoff, n_c, is the nth nearest neighbour whose angular position is found to be isotropically distributed in the individual's view. For the observed starling flock $n_c = 8.0 \pm 0.5$ (std error). Cavagna et al. [2014] pointed out that the use 'structural proxies' (such as in Ballerini et al. [2008a]) does not directly access the interaction. They instead used a maximum entropy method to fit experimental velocity correlation functions, which are inherently long-ranged and were able to infer short-range interactions. The velocity
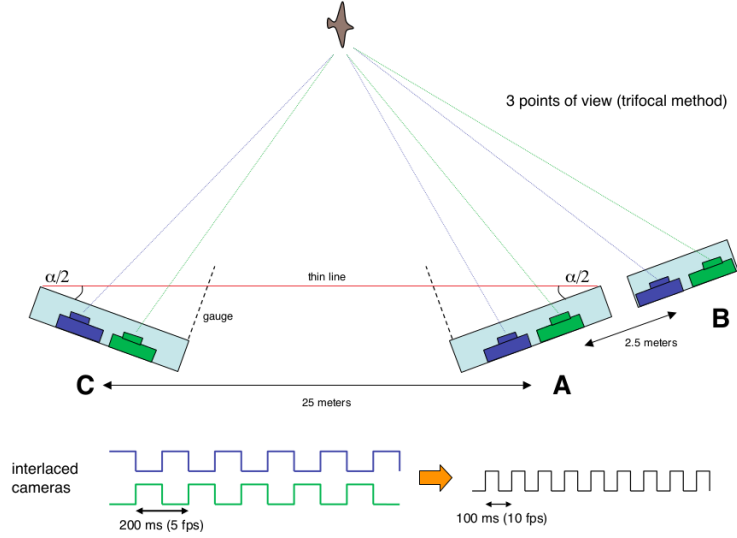
Figure 1.4: The 3-camera set up used by Cavagna et al. [2008b] to capture 3D position (and hence velocity) data for starling murmurations in Rome, Italy.The stereocameras Cameras A and C, are very precisely spaced along a supporting aluminium bar. A thin line was then attached to these cameras under high tension to fix the convergence angle. To solve the problem of matching images of individuals on A with those on C, a third camera B is used, which need not be aligned with A (or B, for that matter).

correlation function was defined as follows, where $\vec{s}_i$ is the unit direction vector for individual i and k_{ij} is the topological distance order (of j from i).

$$\hat{C}(n; \{\vec{s}_i\}) = \frac{1}{N} \sum_{i,j=1}^{N} \vec{s}_i \cdot \vec{s}_j \delta(k_{ij} - n) \tag{1.2}$$

$\hat{C}(n)$ does not decay to zero at large distances due to the directional order inherent in flocking. Hence to investigate the decay of velocity correlation information a connected correlation function is introduced, which essentially removes the order parameter squared and does decay to zero at large distances.

$$\hat{C}(n; \{\vec{s}_i\}) = \frac{1}{N} \sum_{i,j=1}^{N} \delta\vec{s}_i \cdot \delta\vec{s}_j \delta(k_{ij} - n) \tag{1.3}$$

where $\delta\vec{s}_i = \vec{s}_i - (1/N)\sum_k \delta\vec{s}_k$. It is important to note that this method makes no explicit assumption about the nature of the alignment interaction. Modelling the velocity analogously to spins in an Ising-type model, they found that a coupling strength $J(n)$
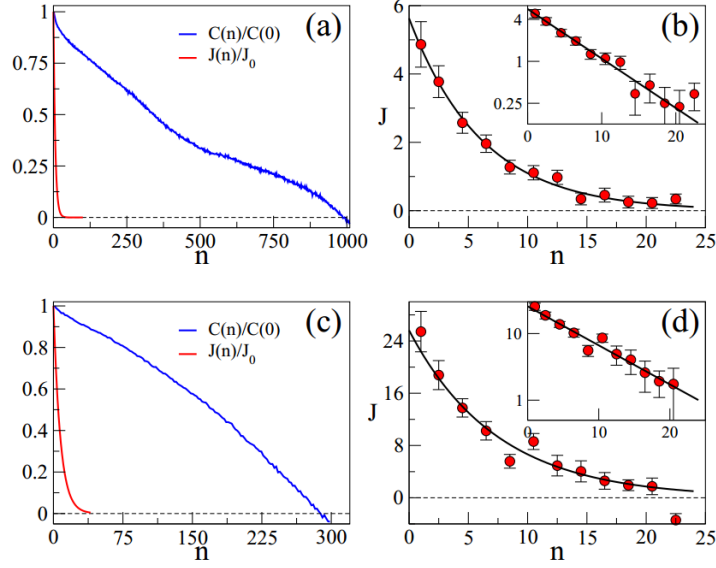
Figure 1.5: **Left** The connected correlation function $C(n)$ compared to the interaction $J(n)$. **Right** Close up of the interaction $J(n)$, the full line is an exponential fit to the data (see the inset). **Top** $N = 2126$, $J_0 = 5.63$ amd $n_c = 6.11$. **Bottom** $N = 717$, $J_0 = 25.63$ and $n_c = 7.41$. From Cavagna et al. [2014].

for the alignment decays exponentially with topological distance order n between birds.

$$J(n) = J_0 \exp\left(-n/n_c\right) \tag{1.4}$$

Where n_c is the topological (n-th) neighbour cut-off for the velocity interaction. Using this model for the velocity interaction between flock neighbours a linear fit to the decaying velocity correlation function for 2 empirical flocking events was found. This produced an estimate that $n_c = 6.5 \pm 0.9$ (standard error), with the maximum entropy (ME) method being used to discard more distant neighbours in the fit (see Fig. 1.5). Essentially the entropy is not decreasing with the addition of more distant neighbours and they contain no information even for noise fitting. From this they deduced the effective alignment interaction in starling flocks is short-ranged. When the analysis was repeated using the metric distance r they found the metric range r_c scales with the density and hence further justification of the argument in Ballerini et al. [2008a] that the interactions are topological and not metric to achieve this scale-free behaviour. Cavagna et al. [2014] extended their ME analysis to the question of whether the interaction is isotropic. They did this by defining θ_{ij} as the angle between $\vec{r}_{ij}$ and the flock's direction of motion $\vec{V}$. θ_{ij} was considered to be in the longitudinal sector (L) if $\cos\theta_{ij} > 1/2$ and in the transverse

9

sector (T) otherwise (a symmetrical relationship). Hence the longitudinal and transverse correlation functions could be defined:

$$\hat{C}^{L,T} = \frac{\sum_{i,j} \vec{s}_i \cdot \vec{s}_j \delta(k_{ij} - n)\Theta(\pm|\cos\theta_{ij}| \mp 1/2)}{\sum_{i,j} \delta(k_{ij} - n)\Theta(\pm|\cos\theta_{ij}| \mp 1/2)} \tag{1.5}$$

where $\Theta(x)$ is the Heaviside step function. Using the observed L and T correlation functions, they found that the interaction between first nearest neighbours in the transverse direction is slightly greater than that in the longitudinal direction. However this anisotropy already disappears at $n = 2$. This suggests they align more with neighbours at their sides, than in front or behind. This can be rationalized on the basis that collision avoidance is easier through alignment than speed changes for those neighbours at the sides. In Ballerini et al. [2008a] nearest neighbours were found to be more often at the sides of an individual and it would seem that alignment is the mechanism for this.

Note this does not invalidate our model in Pearce et al. [2014] as the STARFLAG work is concerned with *alignment* interactions and doesn't take into account cohesive interactions (such as the projection term described later), but it does give useful insights into how to model the alignment interaction. It is clear from a phenomonological point of view that the alignment interaction should be short range and topological in nature, such as one based on the Delaunay triangulation when in a large dense flock. From a mechanistic point of view one expects the interaction to be based on vision in birds, but the mechanism is not explicitly modelled in this work (other than excluding visually occluded neighbours).

1.2.3 Animal Groups

Many animal species live at least part of their time in communities; pelagic fish and ungulates for example. The groupings tend to undergo fission-fusion dynamics and have varying dynamical timescales [Couzin and Laidre, 2009]. Some species fission in daylight to forage and fuse at night for protection, whereas bird flocks often fission and fuse during the space of a minute. The underlying aggregation laws result in familiar distributions: when fusion is relatively high the distributions are often heavy-tailed; and when fission is relatively high the probability of finding a group of that size decays exponentially with the size [Gueron and Levin, 1995]. For fusion dominated heavy-tailed (power law-like distributions) there is no characteristic size of group, which implies that scalings of group properties are more important than properties at a fixed group size.

It has been suggested that groups form due to individuals seeking a target density

(STD) for neighbours in their immediate vicinity. That is to say they attempt to position themselves within the flock so that they obtain as closely as possible a target local density. This target density is assumed to be dependent on the environment and can be used to derive an integro-differential equation for swarming [Grünbaum, 1994]. As these equations only seek to reproduce the observed phenomena and not explain why there is a local target density, this is a mechanistic description of flocking phenomena.

1.2.4 Flocking

A problem with the flocking literature is that 'flocking' means different things to different authors. Heppner [1974b] introduced a taxonomy of airborne bird flocks, which primarily divides flocks into 'flight aggregations' and 'flight flocks'. With the distinction being that aggregations are for a common purpose, such as circling overhead a fish school, whereas flight flocks are groups of flying birds that undertake coordinated aspects of flight (e.g. take off, turning and landing). A higher order division of flight flocks is into 'line formations' such as geese and ducks and 'cluster formations' that have more three dimensional structure, such as starling flocks [Heppner, 1974a]. The sort of flocks or swarms that this work is concerned with are flight flock cluster formations according to this taxonomy and are often described in the literature as 'aggregations' and lead to *how* (mechanistic) questions, i.e. what are the rules that underly the behaviour [Bajec and Heppner, 2009]?

Perhaps we should ask *why* animals flock at all? The majority opinion is that flocking is an evolved behaviour that provides protection against predatory animals. This is known as the 'many eyes theory' and rests on the assumption that larger and more cohesive groups are more able to spot and respond to predators.

An alternative hypothesis is the 'selfish-herd theory' of Hamilton [1971], whereby the probability of being predated is reduced by the abundance of other targets in the group. This hypothesis naturally extends to spatial aspects. The ability to put another individual in between the predator and themselves, making the other a more vulnerable target can be advantageous. Although the other might have a better view of the approaching predator and be better able to respond! If we posit that a predator will tend to attack the nearest individual, then one that has a large empty space around themselves has a large domain of danger (DOD). Inside this zone the predator will be closest to that individual. Hence to reduce this DOD, flocks should compact towards the centre of mass. It has been found that sheep have a strong attraction to the centre of the flock when they are under predation (by a sheepdog...) [King et al., 2012]. Thus

11

the sheep aggregated into a single tight cluster with the sheep packed 'side-by-side'. In contrast the densest part of starling flocks tend to be at the edges. Consideration of selfish herd theory has lead to the observation that any 'good' flocking rule should result in statistically beneficial positions for the individuals that follow it [Viscido et al., 2002]. That is to say, the rules do not necessarily always improve the survivability in a given encounter with a predator, but on average, the domain of danger should be reduced.

The 'confusion effect' is a further potential driver towards the evolution of flocking behaviour. A large number of fast moving prey could potentially overwhelm the sensory apparatus of the predator. This confusion could prevent the predator intercepting the prey, particularly if the agents are birds in flight, where movement is in 3 dimensions.

1.2.5 Models and Simulation

Hildenbrand et al. [2010] created a highly detailed flocking model to deal specifically with starling flocks. It incorporated some additional physical constraints on the particles movements, such as simply-modelled fixed wing flight and 'banking' into turns (no instantaneous changes of direction). The model is a social force model and incorporates attraction to a roosting site (as large murmurations occur shortly before roosting at night), which is particular to starlings. The inter-bird separation, number of interacting neighbours and the thickness of the flock are all tuned to reproduce observed features, whereas most of the aerodynamic parameters are inferred from theory and experiment. This is clearly a heavily parametrized model, but most of the parameters are determined in a principled way. Hildebrandt *et al* explicitly increase the cohesion force when at the edge of the flock by multiplying a centrality measure by fixed magnitude. The centrality measure used is the length of the average vector of the direction to a bird's neighbours.[1] The model reproduces qualitative empirical features, such as flat flocks that tilt sideways while turning and also quantitative features such as the independence of density with flock size [Ballerini et al., 2008a,b].

1.3 Bird Vision

The visual system in the brain evolved to process the projection of visual data. It did not evolve to give an accurate description of the external world, it evolved to give a functional one and inconsistencies could be permitted and that representation is far

---

[1]This can be viewed as a similar behaviour to the projection term defined later. When a bird has an isotropic neighbour distribution, there will be no movement. However at the edge of the flock there is a strong impetus to move inwards.
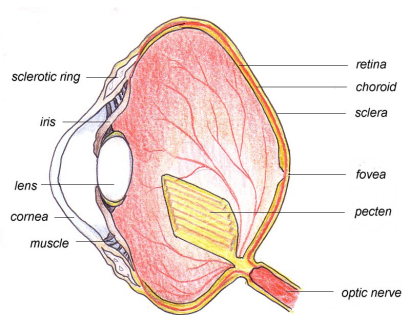
Figure 1.6: The avian eye has a unique structure, the pecten oculi. It is believed to nourish the retina. It is also pigmented and may protect the retina from UV light. The rest of the eye is similar to other vertebrates. Light enters the eye through the pupil, is refracted by the cornea, focused by the lens and then illuminates the retina. The retina is covered in rod and cone cells that detect the light and this information is carried by the optic nerve to the rest of the brain, after some basic processing involving compression.

from perfect. This also partly due to the physiological limits of the sensing apparatus and both effects should be considered.

1.3.1 Vertebrate Vision and the Brain

In birds the most parsimonious mechanism for decision making during collective flight is vision and models that wish to be biologically plausible should be vision-based [Bajec and Heppner, 2009]. A basic understanding of the structure of the visual systems in birds will enhance our ability to make judgements about the plausibility of vision-based flocking models. Most of the comments made are true for all vertebrates and when they only apply to birds this will be clarified. It is important to understand that the eyes are a part of the brain, they contain neurons, both to transmit stimulus to the brain and to do some low-level processing. In fact, the retina and optic nerve begin developmentally as outgrowths of the brain. Light falls on the eye and is mostly diffracted by the cornea, the fine focusing is done by the lens. This focused light then falls on the retina, where it is detected by the receptor cells. These cells are called rods and cones. Rods and cones are active in different regions of luminosity; rods being active at low luminosity (i.e. dark) and cones at high luminosity (i.e. light). The cone cells quickly relax and are therefore more responsive to changes in stimuli than rod cells. Humans have 3 types of cone cell, with 3 different pigments that respond to different parts of the visible spectrum, allowing

13

for colour vision. However, nearly all birds are tetrachromatic – they have four cone cells and some birds are even UV sensitive, because of it.[2] Between the rod and cone cells and the optic nerve are several types of neurone that integrate over and compress the signal from the individual neurons to the capacity of the optic nerve. These are the bipolar cells which pass signals to the retinal ganglion cells, mediated by horizontal cells and amacrine cells that integrate across layers, helping to regulate output. More rod cells are integrated over than cone cells, to give a coarser resolution, but with greater photon sensitivity. Rod and cone cells are not evenly distributed over the retina, the density of cones is smaller at the periphery and there is an area of high density called the fovea. The fovea is typically aligned with the object of current attention to provide the highest resolution image. This region of high resolution is only a few degrees of the visual field, as can be easily demonstrated in humans by keeping your eyes fixed on a word and seeing how many words away from it you can read. The region of foveal vision is roughly the size of your thumb when held at arm's length. Not all bird species have foveas, some have areas of retinal specialisation. These are similar to the fovea in that they contain concentrically increasing densities of cone cells, but without the reduction in surrounding blood vessels and invagination of the fovea. Other birds, have a visual streak, a band-like area stretching across the retina [Fern'andez-Juricic, 2012].

A particular piece of the vertebrate anatomy that is of interest, is the super colliculus or tectum. It is a layered structure located in the midbrain and contains topographic maps of the world in egocentric and retinotopic coordinates in each layer (i.e. a representation of the projection on the retina, is stored in each layer). The super colliculus uses input from the map to direct responses of the body toward the stimulus in real space. For a long time, research concentrated on the role the super colliculus has in directing fast eye movements below perception, known as saccades. But it is also known to direct head-turns and arm movements in primates and most importantly, whole body turns in rats, fish and *birds*. In birds and fish this is one of the largest regions of the brain suggesting an important role. The large size of the midbrain in birds is usually accounted for by the need to control wing movement during flight (although, why then in fish?). That this region of the avian brain is concerned with visual processing and body turns is suggestive that it could be where flocking rules are enacted in the avian brain.

---

[2]Pigeons are perhaps pentachromatic, as they have 5 distinctly pigmented cone cells.
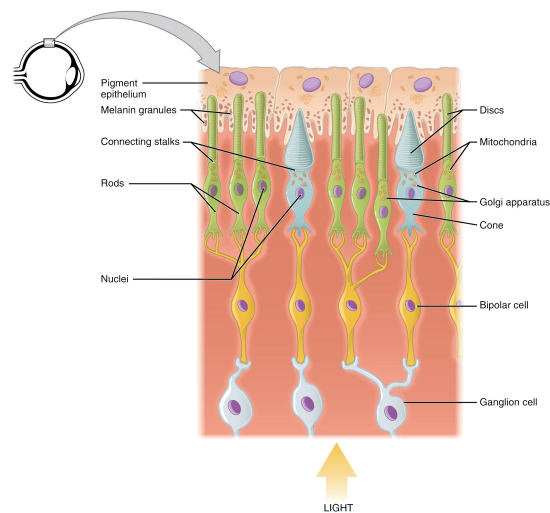
Figure 1.7: The vertebrate retina is made up of several layers of neurones with the rod and cone cells on the side nearest the body, such that the light must travel through the neurones to reach them. This is because they need to be adjacent to the pigment epithelium which supplies them with nutrients to allow them to continue reacting to light. 1414 Rods and Cones" by OpenStax College - Anatomy & Physiology, Connexions Web site. http://cnx.org/content/col11496/1.6/, Jun 19, 2013.. Licensed under Creative Commons Attribution 3.0 via Wikimedia Commons - http://commons.wikimedia.org/wiki/File:1414_Rods_and_Cones.jpg#mediaviewer/File:1414_Rods_and_Cones.jpg
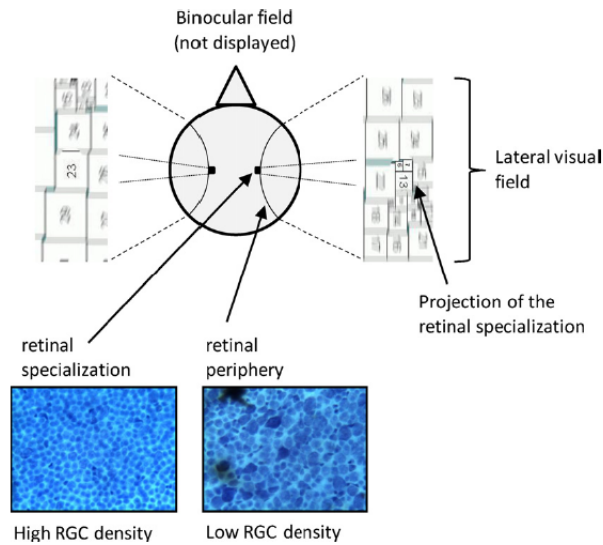
Figure 1.8: Apart from the narrow area around the fovea, the visual field is sampled at a comparatively low resolution. This can be seen through the relative low density of the retinal ganglion cells, outside the region of retinal specialisation [Fern'andez-Juricic, 2012].

1.3.2 Visual Field Size and Acuity

Birds, particularly predatory birds such as hawks and eagles, have proverbially high visual acuity – the ability to resolve (visually) small objects at high contrast. As mentioned previously, the density of cone cells decreases away from the fovea and the resolution of the visual stimulus decreases (see Fig. 1.8). This leads to a very narrow region of high visual acuity – only a few degrees. In addition to a central fovea, about half of bird species have a second fovea, the temporal fovea, and are termed 'bifoveal'. Swifts, terns and hummingbirds are bifoveal and this is believed to help with judging speed and distance (particularly depth perception). Starlings however are monofoveal. This is because the temporal fovea is further forward and provides binocular vision. Starlings however use their lateral visual field to avoid predators. Birds with laterally placed eyes have a very wide visual field, as the head does not occlude much of their rear vision [Fern'andez-Juricic, 2012] (see Fig. 1.9). This contrasts with predatory birds, with front facing eyes who need their better depth perception (from stereopsis) to dive accurately on their prey and don't themselves need to worry about searching the sky for predators.
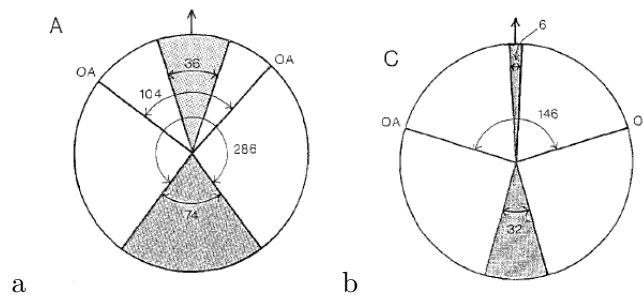
Figure 1.9: Visual field of European starlings in a horizontal plane. Light grey is region of binocular vision and dark grey is the blind region. a is the maximum amount of binocular vision whereas b is the minimum. Note the wide lateral visual field [Martin, 1986].

Contrast Sensitivity Contrast Sensitivity (CS) is the ability to discriminate between adjacent patches of visual stimuli, based on their relative, as opposed to absolute, luminances. Considering the impressive visual acuity of birds it is surprising that they have poor spatial contrast sensitivity relative to humans and other mammals [Ghim and Hodos, 2006]. It is unknown why this is the case. The study of Ghim and Hodos [2006] explicitly looks at starlings among other bird species. This suggests that birds at near positions in an individual's view, whom are likely to have similar luminances, if they overlap would appear as one object. Although, of course, shape recognition may allow them to be recognised as two birds. As more overlaps occur, however, the shape clues will be reduced and distinguishing individual birds becomes less likely.

1.3.3 Vision and Movement

It may come as a surprise, but visual movements in nearly all animals are not smooth, but are characterized by sudden motion followed by periods of visual stability. These sudden movements are called saccades and the reason that vision works like this is, that if motion is too fast it causes visual blur (due to the long response time of the photoreceptor cells - like a long exposure time on a camera). Hence the direction of gaze moves quickly, then stays steady to acquire an image, rather like the frames of an old-fashioned movie reel. In humans these saccades occur at a rate of 3 per second, but the experience of them is suppressed by the brain and it is estimated humans are blind for 10% of the time due either to blur or 'saccadic supression' without even knowing it. Birds do not have the same range of eye movements as humans and most need to move their whole heads to perform saccadic movements and stabilisation [Land, 1999]. An interesting thing to note is that if an image stays perfectly still in the human retina, it

17

gradually fades from perception (this does not occur naturally and requires an apparatus that can keep an image stationary with respect to the retina) [Riggs et al., 1953].

1.3.4 Optical Flow

In 'The Ecological Approach to Visual Perception' Gibson suggested that the motion of light from objects across the retina contains information about its motion and distance [Gibson, 1986]. For example, an approaching object will expand in the visual field, providing information on speed (assuming the size of the object is known). Also movement across the field of view, i.e. a translation, specifies the direction of movement of an object. Hence time differences in the visual field are the basis of the theory and this is described as 'optical flow'. Optical flow has been taken outside of its original psychological context to describe methods of computer vision, including collision avoidance, object motion detection and time-to-collision calculations. There are now many algorithms for image processing based on optical flow, the basis of most is some method to compute a numerical image gradient that is an approximation to the flow field.

1.3.5 Specification for Visual Models of Bird Flocking

The saccadic nature of visual movement suggests that models should focus on image frames, either singly or in groups, as during the periods of fixation or 'frames', is when image capture occurs. The theory of optical flow introduced by Gibson leads us to consider that the flow field may be an important quantity for determining relative motion. Evidence of low contrast sensitivity and the possibility that some bird species don't object complete, i.e. they find it difficult to distinguish nearby objects of similar luminance and may have conceptual difficulties distinguishing objects partly obscured by other objects in front or behind. This implies that many starlings in the flock may appear to be simply parts of large patches of indeterminate size and distance. Due to the high visual acuity and the visual system's ability attuned to distinguish edges, it is likely these patches would have well defined edges in the visual field.

1.3.6 Comments

A neighbour distance ranking or 'n-th nearest neighbours' are often used to characterise topological range. It is not clear to the author that starlings use such a rule, as opposed to another topological distance metric. Even if they do so, the rule is most probably visual and only through 'accident' appears to be a topological rule. Unless of course they have some perception of where their n-th nearest neighbours are located, stored

and updated regularly in their brains, which seems unlikely but not impossible. A physicist might argue that if the effect is the same then it doesn't matter, what the underlying evolutionary motivation for the rule is. The question here is whether different mechanisms of achieving this topological range are distinguishable. Even if they are, there remains an interesting question for the neuroscientist about how and where this processing occurs in the brain, i.e. where in the avian brain is this representation of near neighbourhood stored, if indeed it is? There is strong evidence that the human brain stores its current position on a kind of lattice of cells in the hippocampus. These are known as grid cells and have been found to exist in rats [Doeller et al., 2010].[3] There could potentially be a similar piece of neural architecture in starlings that represents the topological positions of their neighbours.

A difficult question to approach is how aware the bird is of the stimuli producing flocking behaviour. Is it essentially an autopilot mechanism? Whereby the visual system of the bird controls the flight. Or to what degree is the behaviour instinctive or learned? For instance, baby birds may flap their wings as they fall from the nest, in an instictive manner, but they need practice to be able to fly. Would a flock of starlings raised in captivity flock differently to wild starlings? Unfortunately these questions will not be (and cannot be) answered in this work.

---

[3]The 2014 Nobel Prize for Physiology was given for the discovery of grid cells.

Chapter 2

A 3D Visual Model of Flocking

A variation on an old joke goes as
follows:
Engineers study interesting real world
problems but fudge their results.
Mathematicians get exact results but
only study toy problems.
But computer scientists, being neither
engineers nor mathematicians, study
toy problems and fudge their results.

Gary William Flake – *The
Computational Beauty of Nature*
(1998)

2.1   Introduction

Until recently the difficulty in obtaining 3D data for the positions of flocking animals
has resulted in scarce data for direct comparison between theory and experiment. Hence
comparisons have usually been made between models [Cavagna et al., 2008b]. However
the EU STARFLAG project was able to develop a new technique and algorithms for
finding the positions of birds in flocks of up to several hundred, by using a 3 camera
set up [Cavagna et al., 2008a] (see §1.2.2). While the observed data is useful, there are
limits to the capabilities of the set up and individuals in the interior of very dense flocks
cannot be distinguished. This limits the flocks which can be observed to those that
are sufficiently diffuse (hence flocks are frequently rejected, introducing a possible bias).

The birds they chose to investigate were common European starlings, *sturnus vulgaris* – a bird well known for it's 'murmurations', or flocking behaviour, shortly before roosting for the night. Starlings are known to flock in groups of up to tens of thousands, but these flock sizes are too large for the STARFLAG techniques to be applied. Work has also been done on the analysis of photographs of starling flocks in this group, which is of course an instantaneous 2D projection of a flock containing information about the flock density, but does not have the stereoscopic information required to reconstruct the shape of the flock (and hence the inhomogeneities in flock density along different axes of the flock).

The model described in the following section is a 3D model and can be *directly* compared with the measurements of flock properties taken by the STARFLAG project, which, as stated in the introductory chapter, has not been the general practice when making computational models of natural flocks. The main thrust of this chapter is these direct comparisons and a description of the methods to account for biases in measurements of geometrical properties of flocks due to the ratio of flock surface to interior (particularly a problem in 3D) is given in §2.3.

It is found that there are parameter sets for the 3D model that reproduce the observed anisotropy in flock dimensions §2.6.3, the anisotropy of the nearest neighbour angular distribution (i.e. relative position) §2.6.4 and the scaling of the flock size with the number of individuals N §2.6.1, of natural starling flocks. These features of the model are due to the novel visually inspired 'projection' term described in the following section.

In addition to these empirically verifiable properties of flocks, convincing models should have parameter regimes where the flock is highly aligned and not overly disperse, which are investigated through a parameter study in §2.4.3.

2.2   Model Description

A 3D particle based computer model of animal flocking was constructed. It is an agent based model with N identical agents each with identical equations of motion. The equations of motion contain standard contributions for alignment and noise (reflecting the imprecise biological nature of the agents), together with an additional contribution from the edges of occluded regions in each individual's field of view. This additional contribution controls the flock density and is rooted in consideration of the response of visual system of birds to visual stimuli.

The 3D simulations were realised using an algorithm written in C++. The model

is a discrete time model with a fixed individual velocity v_0 and position update rule similar to the Vicsek model [Vicsek et al., 1995]. It is important to wait a sufficiently long time before measurement so that any transient behaviour, before a steady state is reached, has passed. This is discussed in §2.4.1.

The N individuals were initially placed randomly in a cube with a number density of 0.01 individuals per unit cube (dimensionless) and were assigned random directions. A velocity update rule was then applied to obtain subsequent positions. Individuals, can pass through each other, which are referred to as 'phantoms'. The velocity of individual i at the $t+1$ timestep is defined to be:

$$\vec{v}_{i,t+1} = \phi_a \frac{\langle \vec{v}_t \rangle_{n_i}}{\|\langle \vec{v}_t \rangle_{n_i}\|} + \phi_p \vec{\delta}_{p,i} + \phi_e \vec{\eta}_i \tag{2.1}$$

It is useful to define a parameter vector $\vec{\phi} = (\phi_a, \phi_p, \phi_e)$, where $0 \leq \phi_{a,p,e} \leq 1$ are control coefficients. It is assumed that it is the relative proportion of these terms that is important not their absolute values, hence scaling the parameters by a constant does not change the results of the model e.g. $\vec{\phi} = (0.8, 0.1, 0.1)$ is equivalent to $(1.6, 0.2, 0.2)$. The three terms appearing on the RHS of Eq. 2.1 are, respectively:

a) The alignment term, $\frac{\langle \vec{v}_t \rangle_{n_i}}{\|\langle \vec{v}_t \rangle_{n_i}\|}$. This is the average direction over the n_i individuals indexed by j that are neighbours of i at the previous timestep, i.e.:

$$\frac{\langle \vec{v}_t \rangle_{n_i}}{\|\langle \vec{v}_t \rangle_{n_i}\|} = \frac{\sum_{j=1}^{n_i} \vec{v}_{j,t}}{\|\sum_{j=1}^{n_i} \vec{v}_{j,t}\|} \tag{2.2}$$

Neighbours need to be defined to implement the alignment term and the Delaunay triangulation leads to a natural conception of 'neighbour' due to it being the dual graph to the Voronoi construction, in which all points nearer to a focal individual than any other belong to that individual's Voronoi cell, hence neighbours defined through the Voronoi construction are those that share edges between their Voronoi cells [Pion and Teillaud, 2014]. This neighbour assignment is the first 'Voronoi shell' of individuals and provides a simple criterion distinguishing near and far flock members, with the nearest (shell) flock members assumed to be most relevant perceptually. This Voronoi method of assigning neighbours is used in Ginelli and Chate [2010]. The CGAL library was used to provide the triangulation [Pion and Teillaud, 2014]. As this model aims to be based on visual perception, the Delaunay triangulation was considered to be more appropriate than simply choosing n nearest neighbours. Cavagna and Giardina [2008] gathered evidence from the literature that birds may have a cognitive limit on the number of

neighbours of whose positions they can keep track of at any one time to be approximately 7 individuals. This accorded well with their findings of non random neighbour positions up to approximately the seventh nearest neighbour in starling flocks. Hence by following the STARFLAG argument an alternative approach would be to use an average velocity taken over the 7 nearest neighbours. See §2.8 for a comparison of models employing neighbour identification algorithms based on Delaunay and nearest neighbour flocks in 2D.

b) a term based on the visual projection of the entire flock onto the view of flock member i, $\vec{\delta}_{p,i}$. An illustration of the projection term is shown in Fig. 2.1 – note, that an individual's view sphere is larger than its projection. The model is vision based and the view of an individual is assumed to be the surface of the unit sphere surrounding the particle centre. The spherical cap[1] projected by an individual j onto i's view is defined by a solid angle given by $\Gamma = 2\pi \left(1 - \frac{R}{\sqrt{1+R^2}}\right)$, where $R = |\mathbf{r}_{ij}|$ is the distance between the individuals. Hence Γ defines the angular size of the projection in 3D. This is equivalent to an individual j being viewed as a disk of unit radius with its normal vector always pointing towards the focal individual i. Individuals were treated as isotropic bodies that obscure a line of sight from any other individual that passes through it (this is not the same projection that a sphere would give). This results in the projection of (dark) circular caps onto the unit spherical view of other individuals. The interior of any of these caps represent directions where an individual is unable to trace a line of sight to infinity (the light sky). These caps can overlap, leading to a patterning of the surface of each spherical view into 'dark' and 'light' regions [Pearce et al., 2014]. The boundaries of the occluded regions on the surface of the ith individual are then unions of arcs of circles in 3D, collectively the set of contours C_i. The projection term appearing in the equation of motion is

$$\underline{\delta}_{p,i} = \frac{\int_{\{C_i\}} \hat{\vec{r}} dl}{\int_{\{C_i\}} dl} \tag{2.3}$$

where each integral is over infinitesimal line elements $\mathrm{d}l$ that trace along the curve(s) C_i separating the 'dark' and 'light' regions on the surface of the unit sphere and $\hat{\vec{r}}$ is the outward pointing unit vector at each point along those curves. This integral is equivalent to taking the centre of mass (c.o.m.) of the circular arcs that make up these boundaries. The projection term will always have magnitude less than 1. The effect of this projection term in the equation of motion is:

1. Individuals at the edge of the flock will move inwards, due to the projection of

---

[1] The region of a sphere lying above or below a given plane.

the flock onto their view having an average direction (i.e. their view won't be isotropic). This prevents the flock from dissipating.

2. Individuals attempt to achieve a homogeneous view. This leads to an average steady state density for the flock, with a characteristic scaling behaviour.

To get a feel for the projection term, imagine yourself flying in a flock of starlings surrounded by clear blue sky. Your view is spherical and we will imagine there is no Earth beneath you, only more sky. What do you see? In all cases you see a 2D projection of your surroundings, like a 'fish eye' lens photograph. If you are outside the flock, you see a dark region containing birds, probably with many gaps and the rest is just clear blue sky. To stay with your fellows, you must fly towards that dark region. Now, you are inside the flock, at the very centre, what do you see? This time your view looks the same in all directions and it is not clear where you should fly to stay in the centre of the flock. If you are inside the flock and your view has more boundary in one region it is likely that the flock is denser there and you should wish to move towards it. In this way the flock cohesion and density is controlled. A strength of the model is that, as this is a visual model, only other individuals that can be *seen* generate any response.

c) a random unit vector $\vec{\eta}$, with elements $\eta_x \sim \text{unif}(-1, 1)$ s.t. $\|\vec{\eta}\| = 1$.
The position update was therefore

$$\vec{x}_{t+1} = \vec{x}_t + v_0 \Delta t \, \frac{\vec{v}_{t+1}}{|\vec{v}_{t+1}|} \tag{2.4}$$

The only effect of the timestep is to rescale the flock sizes, due to larger or smaller distances travelled, but this is not relevant to the behaviour as all the interaction terms scale in the linearly with the timestep. Hence Δt the length of the discrete time step, is taken to be 1 for simplicity.

2.3 Making Neighbour-based Measurements in 3D

It is desired to measure the instantaneous volumes and density of the flock. Therefore a bounding surface often called the flock edge or border must be established. The proportion of flock members on the edge of the flock also strongly influences neighbour based statistics, e.g. nearest neighbour distances. These effects are less strong in 2D than they are in 3D due to the increased proportion of edges to bulk in 3D, which means edge effects can usually be ignored in 2D with moderate numbers of individuals.
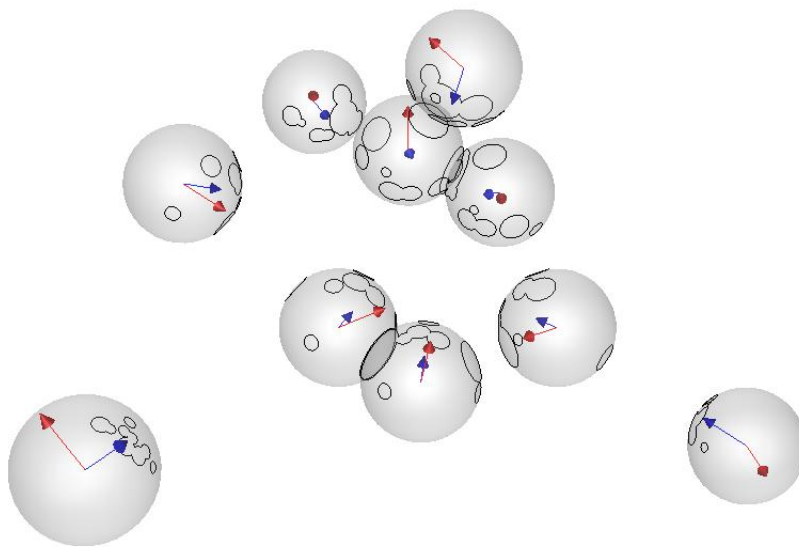
Figure 2.1: An example of the algorithm in the center of mass coordinate frame. Spheres represent an individual's view; red arrows are $\vec{v}_{i,t+1}$; blue arrows are $\vec{\delta}_{p,i}$. The parameters are $\vec{\phi} = (0.3, 0.1, 0.6)$, $N = 30$.
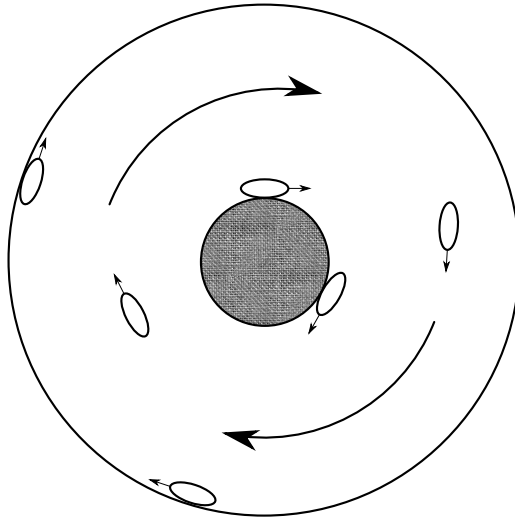
Figure 2.2: Border Bias in a Milling Fish Configuration: The yellow area represents a school of fish in a milling, or toroidal, configuration: all animals rotate clockwise around an empty core. Animals on the external border lack neighbours on their left, whereas animals on the internal border lack neighbours on their right. However, animals on the external border are much more numerous than animals on the internal border. As a consequence, if we include all animals in the statistics of nearest neighbours, we find that on average animals have a lower probability to have their nearest neighbour to their left. This result would be the opposite for a school rotating counter-clockwise, showing that it is not a fundamental feature of the inter-individual interaction, but rather an artefact due to the undue mixture of structural (nearest neighbour location) and morphological (toroidal shape) results [Cavagna et al., 2008a]

2.3.1 The problem of Borders

Flocks are 3D objects and defining the edge of the flock is not as simple a problem as it may appear at first glance. It is in fact a problem similar to measuring the coastline of the UK, the smaller your ruler is, the smaller the concavities you can measure and the longer the coastline. There will be a considerable difference in the edges of the UK if one uses a 1000 mile ruler to a 1 mm ruler. Some measurements are affected by the border of the flock. For instance, it is very obvious that volume and density measurements depend crucially on the location of the border as this specifies the volume. Taking the convex hull of a point cloud containing large concavities will result in large regions devoid of particles, which is clearly not what is wanted when measuring these properties.

Individuals on the edge of a flock are in a special position and their relative proportions influence neighbour related statistics. Cavagna et al. [2008a] ask us to consider fish milling in 2D, i.e. moving circularly, with an empty core at the centre (see

Fig. 2.2). If one were then to measure the average angle to the nearest neighbour, one would find that there are more neighbours to the right if the fish are moving clockwise or to the left if they are moving anticlockwise. The point to grasp, is that this a bias due to *geometry* not *biology*. Clearly the larger the fish swarm, the smaller the discrepancy would be, as more fish would be in the bulk and not at the borders, where conditions are special. To make clear statements about the biology or the model, we must first eliminate geometrical bias. This bias originating from the edge of the flock, becomes a bigger problem in 3D, due to dimensionality, as the ratio of the border to the bulk becomes larger. Consider an approximately spherical random distribution, centred about the origin with a fixed density ρ. To maintain such a fixed density, r must scale with N, the number of random points, as follows:

$$A = 4\pi r^2 \tag{2.5}$$

$$V = \frac{4}{3}\pi r^3 \tag{2.6}$$

$$\rho = \frac{N}{V} = \frac{3N}{4\pi r^3} \tag{2.7}$$

$$\implies r = \left(\frac{3N}{4\pi\rho}\right)^{1/3} \tag{2.8}$$

Hence the surface area, A, to volume, V, ratio scales as

$$\frac{A}{V} = (36\pi\rho)^{\frac{1}{3}} N^{-\frac{1}{3}} \tag{2.9}$$

$$\propto N^{-\frac{1}{3}} \tag{2.10}$$

This demonstrates that the individuals near the boundary surface make up a non-negligible fraction of the total points that is slowly decreasing with N, relative to the 2D case where the equivalent ratio scales as $N^{-\frac{1}{2}}$. This scaling means that simulations at larger N are necessary in 3D to obtain good statistics on neighbour relationships, such as nearest neighbour distances and averages of properties over nearest neighbours.

That statistics calculated over neighbours are affected by the boundary is also obvious if you consider nearest neighbour distances. If the nearest neighbour is $2\,\mathrm{m}$ from an individual, but the individual is $1\,\mathrm{m}$ from the boundary, then it is possible that the individual could have had a nearer neighbour at, say, $1.5\,\mathrm{m}$ on the far side of the boundary if the individual had instead been in the bulk. Being near the border biases against distances longer than the distance to the border. Three further examples are given by Cavagna et al. [2008a] of flock properties that are affected by border bias:

that nearest neighbour distances increase with the total number of individuals as N;[2] the cumulative distribution of the neighbour distance is biased; and the orientation of velocities created by randomly pairing random points within a domain with the same aspect ratio of a starling flock show anisotropy.

Once again, assuming the distribution of individuals is approximately spherical (a best case scenario with minimal surface area to volume ratio), a density of 1 per unit[3] requires $N \sim 10^4$ before the volume surface area to volume ratio becomes less than a half:

$$\rho = 1, \frac{A}{V} = 1/2 \quad \implies \quad (36\pi)^{1/3} N^{-1/3} = 1/2 \tag{2.11}$$

$$\implies \quad N \sim 10^4 \tag{2.12}$$

and $N \sim 10^8$ for less than 0.01 (or 1%):

$$\rho = 1, \frac{A}{V} = 0.01, \quad \implies \quad (36\pi)^{1/3} N^{-1/3} = 0.01 \tag{2.13}$$

$$\implies \quad N \sim 10^8 \tag{2.14}$$

Clearly higher N is required to reach the same ratios at lower densities. Here the simulations only use at most $N = 10^3$, due to computational constraints. We therefore need to remove the border bias to get reliable measurements of nearest neighbour properties.

2.3.2 Methods to Remove Boundary Bias in Statistics over Neighbours

Alpha Shapes

The problem of edge effects when averaging over neighbouring points is well known in spatial statistics and there are methods to reduce this bias. The first step to the solution is to identify the boundary. As animal flocks are not necessarily convex, using a convex hull may not be an appropriate determination of the flock boundary. Instead Cavagna et al. [2008a] suggest using alpha shapes. A 3D alpha shape is a polyhedron formed from a point cloud (i.e. collection of points in 3D space). It is not necessarily convex – in fact that is the point. The alpha shape is an alternative to using a convex hull to define a point cloud's bounding polyhedron, which is preferable when the point cloud is not necessarily convex. Alpha shapes have a parameter α that in 3D is the squared-radius of a sphere and constrains the minimum size of concavity in the alpha shape. This is a

---

[2]Although separate analysis of their own data (after they have adjusted for the border bias), reveals the opposite trend.
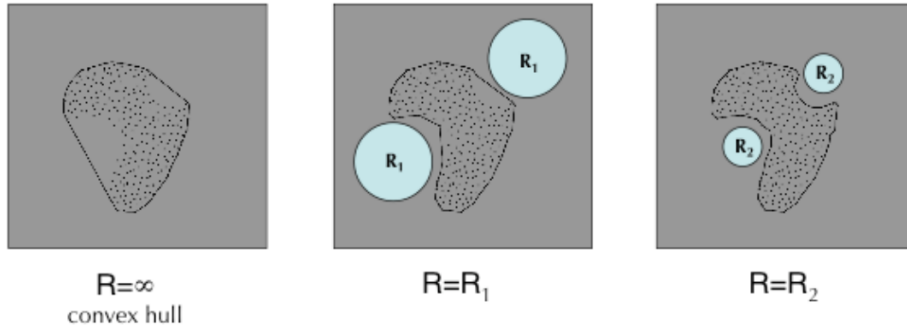
R=∞
convex hull

R=R₁

R=R₂

Figure 2.3: In 2D the α parameter which is the squared radius R^2 of the smallest disc that is allowed to touch 2 points in the aggregation (which are then boundary points). In this way concavities at roughly the scale of R are recovered. If R is much larger than the scale of the largest concavities, then the convex hull is recovered, which clearly contains large empty regions [Cavagna et al., 2008a].

'nibbling' parameter and controls how close to the points in the point cloud the alpha shape can be (see Fig 2.3 for a 2D explanation of the parameter). The collection of all possible spheres such that they do not contain any of the point set (except on their edges), leads to the alpha shape for the set. This can involve carving out points inside the set if there are holes smaller than the scale of $2\sqrt{\alpha}$ and allows for concavity in the exterior boundary also. As $\alpha \to 0$ the alpha shape tends to the point set (and hence will be disconnected). Alternatively as $\alpha \to \infty$ the alpha shape tends to the convex hull, as the spheres have infinite radius and cannot penetrate the interior of the point set.

The collection of spheres that results, is replaced by faces defined by the points intersecting the edges of the spheres and this is usually referred to as the alpha shape.[3] There is only one convex hull, but there are many possible alpha shapes. To construct an alpha shape the value of α must be fixed. Here, each simulated flock is considered to be a single flock, even if there are two or more sub-groupings separated by large distances relative to the inter-group distance. Then it is required that the optimal alpha value results in one connected alpha shape, encompassing all sub-groupings.

The alpha shape implementation used in this study is from the CGAL C++ library and is based on a Delaunay triangulation [Da and Yvinec, 2014]. For each value of α the alpha shape contains all the simplices of the triangulation such that the circumscribing sphere is empty and has a squared radius less than α.

See Fig. 2.4 for an illustration of the alpha shape algorithm applied to a cube

---

[3]Properly speaking, this is the alpha complex. The alpha shape has the curved surface defined by the spheres, but the usage here is common - cf. Edelsbrunner and Mücke [1994].
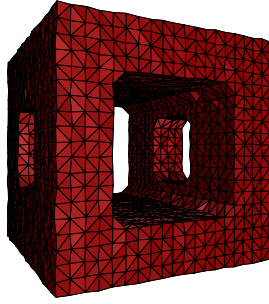
Figure 2.4: A 3D alpha-shape for a cube with two cuboid paths through it. The cube contains 5640 points that have been disturbed from their positions on a lattice a small amount of noise, $\Delta \mathbf{x} \sim \mathrm{unif}(-1/7\mathrm{h}, 1/7\mathrm{h})$, where h is the lattice spacing (there are some computational artifacts on a precise lattice). As can be seen using the optimally computed α-value results in a boundary that clearly distinguishes the inner concavities. Cf. the convex hull, which would be simply the cube.

with two cuboid paths hewn through it to introduce concavities. At the scale of the concavities, the volume of the alpha shape increases sharply, as those concavities become filled in. Concurrently, the number of points interior to the alpha shape (N_I) increases less sharply, as most of the volume added to the alpha shape is devoid of points when a genuine concavity is filled. This leads to a sharp drop for N_I/V at the width of the concavities, as can be seen in Fig. 2.5. As also can be seen in Fig. 2.5, the optimal α-value from the algorithm selects an α below the scale of the concavities as previously required and is the smallest α such that the alpha shape is fully-connected. The STARFLAG method would fix α just below the size of the smallest concavity, but as can be seen from the figure this makes very little difference to the α-value compared with the choice used here.

Once the boundary has been determined, a simple method to reduce the boundary bias is to determine the distance from each particle to the boundary and in any neighbour calculations, if a neighbour is further from the focal individual than the boundary, then it is discounted from the statistic (there are other methods where the individual would be down-weighted based on distance). This method is called the Hanisch method and is known to give similarly very good results for test problems (but slightly overweights near-neighbours) and has the virtue of simplicity over other methods [Cavagna et al., 2008a].
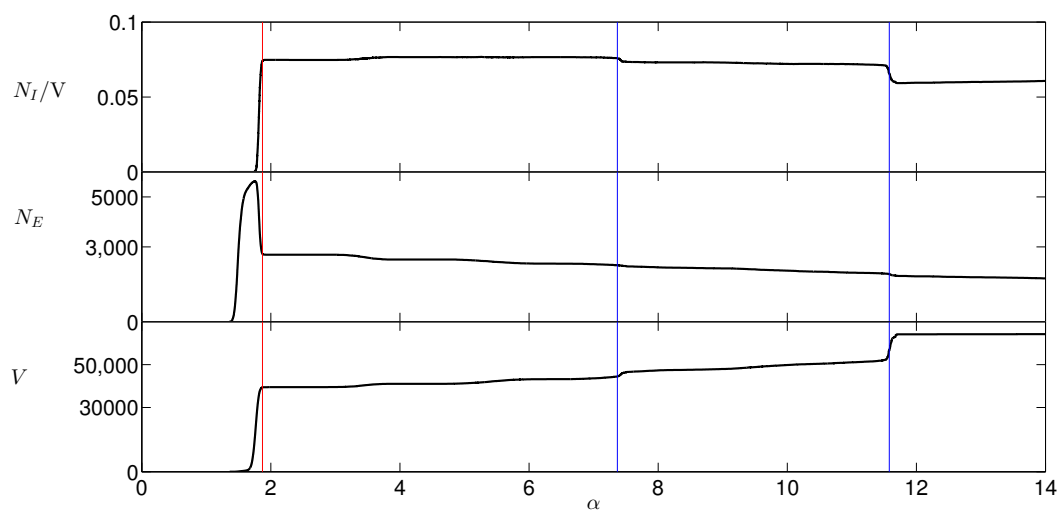
30

Figure 2.5: The blue lines indicate the α value corresponding to the widths of the introduced concavities and the red line is at the selected 'optimal' alpha value. Initially the number of edge points, N_E, rises as small alpha complexes are formed. Eventually these get large enough to connect together and the number of edge points decreases as they become interior to larger alpha complexes, until there is only one alpha complex, connected by the minimally sized facets at the optimum α-value. At this point the volume increases more slowly as the edge of the shape is adjusted less rapidly with increasing α until the large concavities are filled in, when V increases rapidly and N_I more slowly, resulting in the large drops in N_I/V, which had remained relatively constant after the optimal α-value.

2.4 Results

We analyze the flock opacity Ω, this is the average fraction of an individual's view filled by other flock members, over the N flock members.

$$\Omega = \left\langle \frac{A_{\mathrm{s}}}{4\pi r^2} \right\rangle_N \tag{2.15}$$

where A_{s} is the spherical surface area occulted by the flock. For a flock to be transparent $\Omega \ll 1$ and opaque $1 - \Omega \ll 1$.

A standard order parameter for collective motion is the average normalized velocity, Ψ [Vicsek et al., 1995].

$$\Psi = \frac{1}{N v_0} \left| \sum_{i=1}^{N} \vec{v}_i \right| \tag{2.16}$$

Where v_0 is the average absolute velocity of individuals in the system (in this model a constant, $v_0 = 1.0$). This order parameter is close to 1 when members of the flock are aligned in approximately the same direction and close to 0 when orientations are uniformly random.

A simple measure of the flock size is the maximum linear distance through the flock $r_{\max}$, i.e. the maximum separation between any 2 individuals in the flock.

2.4.1 Convergence

Before time series reach stationary states they often display transient behaviour that is not reflective of the stationary state. The flocks are not initialised with a density that is the steady state density for the model and hence the measured quantities will initially change quickly as this relaxation occurs. A common method of deciding if a measured quantity has reached convergence is to look at the running mean and variance of the quantity. If these become approximately constant and remain so, then heuristically, the quantity has reached an at least weakly time stationary state[4]. Once this state has been reached and any transient behaviour has finished measurement of of flock properties can begin.

For the $N = 200$ flocks, with the exception of $r_{\max}$ for $\vec{\phi} = (0.495, 0.495, 0.01)$, all the observed running mean traces (see Fig. A.1–A.5in A) converged within $\sim 10,000$ timesteps. The running variances have also peaked (at least for the first time) for the observed measured properties by 10,000 timesteps and appear close to equilibrated by

---

[4]A term from signals processing referring to a signal that has a stationary first and second moment, but is not necessarily stationary for all moments.

50,000 timesteps. Hence an equilibration period of 50,000 timesteps will be used for the measurement of these quantities. $r_{\max}$ for $\vec{\phi} = (0.495, 0.495, 0.01)$ takes a very long time to equilibrate due to the very small amount of noise in the simulation. Likewise, for other points on the parameter plane with very small amounts of noise the equilibration time for some quantities is expected to be longer than computationally accessible simulation times permit.

2.4.2 Autocorrelation Times

Time autocorrelation is defined as a property of a statistically time stationary process. This is because the correlations are in fluctuations relative to the time average of the stationary distribution (and this does not change). It is assumed here that the measured variables are stationary after a suitable 'equilibration' time. This seems reasonable, in at least the weak sense, i.e. the first two moments of the distributions are time stationary. The time autocovariance function is defined as

$$\chi(t) = \mathbb{E}[(X_{t'} - \mu)(X_{t'+t} - \mu)] \tag{2.17}$$

where μ is the time average of the random variable X_t. The above formula is correct but the preferred formula for the empirical time autocovariance function of a variable $x(t)$ used here is:

$$\chi(t) = \frac{1}{t_{\max} - t} \sum_{t'=0}^{t_{\max}-t} x(t')x(t'+t) - \frac{1}{t_{\max} - t} \sum_{t'=0}^{t_{\max}-t} x(t') \times \frac{1}{t_{\max} - t} \sum_{t'=0}^{t_{\max}-t} x(t'+t) \tag{2.18}$$

The mean in the second term uses the same subset of data as in the first term. As Newman points out, this results in $\chi(t)$ being slightly better behaved than otherwise [Newman and Barkema, 2010]. Eqn 2.18 is divided by $\chi(0)$ to give the true autocorrelation, which is normalized to 1 at $t = 0$. It is usual for the long-time tail of the autocorrelation function to be exponential:

$$\chi(t) \sim e^{-t/\tau_x} \tag{2.19}$$

where τ_x is the characteristic time of the decay or autocorrelation time for quantity x.

A simple method to estimate the autocorrelation time is to approximate short time behaviour by the long time behaviour and then to fit, by least squares, the gradient on a log-log plot. This method is sensitive to where the cut-off for the fit is made, as noise dominates at long time differences and the plot becomes non-linear. It is also not

Table 2.1: Measured correlation times for the opacity Ω in $N = 200$ flocks, using time to $1/e$ of initial value and integrated correlation time as measures. Measurements are averages over 5 repeats $\pm$ the standard error. (The standard error used is the standard deviation divided by the square root of the number of samples.)

N	ϕ_a	ϕ_p	ϕ_e	τ_h	τ_int
200	0.0	0.1	0.9	233.4 ± 7.5	252 ± 58
200	0.0	0.9	0.1	3.00 ± 0.00	7.55 ± 0.60
200	0.333	0.333	0.333	24.2 ± 0.3	19.7 ± 2.2
200	0.495	0.495	0.01	4361 ± 1468	3443 ± 1047
200	0.8	0.03	0.17	118.8 ± 15.6	268.0 ± 47.8

easily automated, due to the subjectivity in the cut-off. Instead, two simple estimates of the autocorrelation time were used here, which again approximate the short time behaviour by the long time behaviour. The integrated autocorrelation time is the sum of the autocorrelation function over the time series:

$$\int_0^\infty \frac{\chi(t)}{\chi 0} \mathrm{d}t = \int_0^\infty e^{-t/\tau} \mathrm{d}t = \tau_\mathrm{int} \tag{2.20}$$

which has been estimated from the discrete time sum. The other measure used is simply the first time, τ_h, such that the autocorrelation drops below e^{-1} .

$$\tau_\mathrm{h} = \min(t) \text{ s.t. } \frac{\chi(t)}{\chi(0)} < e^{-1} \tag{2.21}$$

The autocorrelation time is important, as 2τ is a reasonable criterion for the time between independent samples of a measured quantity x. It is usual to sample the time series with timesteps smaller than the correlation time of the variables that we wish to measure. Otherwise we cannot make good estimates of the correlation times for these variables. There are therefore fewer statistically independent samples than the number of timesteps in the simulations would suggest. It is important that the simulations have been run for long enough after the equilibration time for measurements to be taken and ideally would be run for many times longer than the longest correlation time in the system to get good quality moment statistics for the measured properties.

The autocorrelation times for the measured quantities using both approximations of τ seem to be less than a few hundred time steps, except for $\vec{\phi} = (0.495, 0.495, 0.01)$ which has very little noise in the velocity updates (see tables 2.1, 2.2 and 2.3). With the very small amount of noise (1%) the correlation times are estimated to be less than 5000 timesteps. Hence measurements over $100,000$ time steps will contain at least 10

Table 2.2: Measured correlation times for the velocity order parameter Ψ in $N = 200$ flocks, using time to $1/e$ of initial value and integrated correlation time as measures. Measurements are averages over 5 repeats $\pm$ the standard error. (The standard error used is the standard deviation divided by the square root of the number of samples.)

N	ϕ_a	ϕ_p	ϕ_e	τ_h	τ_{int}
200	0.0	0.1	0.9	1.0 ± 0.0	1.01 ± 0.05
200	0.0	0.9	0.1	1.0 ± 0.0	1.05 ± 0.07
200	0.333	0.333	0.3333	2.0 ± 0.0	3.08 ± 0.43
200	0.495	0.495	0.01	399.0 ± 98.3	673.5 ± 73.2
200	0.8	0.03	0.17	2.0 ± 0.0	6.02 ± 0.57

Table 2.3: Measured correlation times for the measure of flock size r_{max} in $N = 200$ flocks, using time to $1/e$ of initial value and integrated correlation time as measures. Measurements are averages over 5 repeats $\pm$ the standard error. (The standard error used is the standard deviation divided by the square root of the number of samples.)

N	ϕ_a	ϕ_p	ϕ_e	τ_h	τ_{int}
200	0.0	0.1	0.9	185.0 ± 5.8	199.6 ± 23.2
200	0.0	0.9	0.1	163.4 ± 5.6	173.1 ± 12.0
200	0.333	0.333	0.333	45.8 ± 0.8	37.1 ± 7.7
200	0.495	0.495	0.01	3739 ± 955	2831 ± 628
200	0.8	0.03	0.17	461.4 ± 57.8	458.2 ± 81

independent measurements of these quantities and typically orders of magnitude more.

2.4.3 Parameter Space Diagrams

Diagrams were constructed, showing the order parameter (Ω, Ψ) and $r_{\max}$ vary with the control parameters in the velocity update equation, Eqn 2.1. These are analogous to phase planes in equilibrium statistical physics, where order parameters are controlled through canonical variables of the system, such as entropy (which is related to the noise control parameter ϕ_e here). These diagrams show relationships between the values of the control parameters and the measured variables and help give an overview of the types of behaviour the model outputs can display. There are 3 control parameters, but only 2 degrees of freedom as it is the relative proportions of these terms that determines the model output, rather than their absolute values (as the velocity is normalized). Hence the parameter values for ϕ_a, ϕ_p, ϕ_e could be constrained such that:

$$\phi_{\mathrm{a}} + \phi_{\mathrm{p}} + \phi_{\mathrm{e}} = 1 \tag{2.22}$$

allowing our results to be displayed in the $\phi_{\mathrm{a}}, \phi_{\mathrm{p}}$ parameter space with ϕ_{e} following by construction. Parameter planes were calculated for a flock of $N = 200$ members, with a $50,000$ timestep burn-in, followed by $100,000$ timesteps of data gathering.
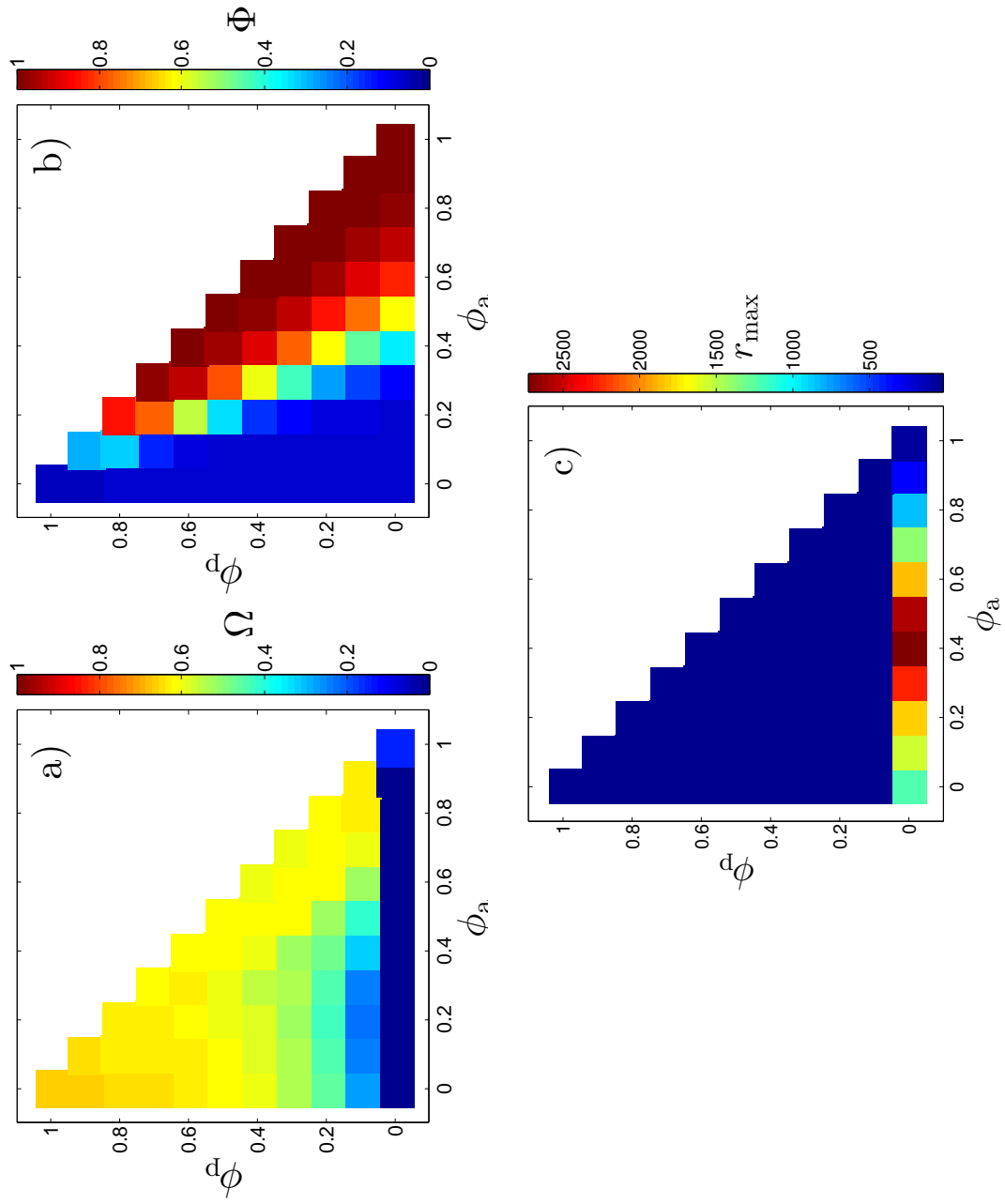
These parameter space diagrams are given in Fig. 2.6.

Figure 2.6: Parameter space diagrams for $N = 200$ flocks. Mean values of a) opacity, Ω, b) normalized velocity, Φ, c) maximum member-member distance, r_{max}.

As Fig. 2.6 a) shows, the opacity, Ω, is controlled by the projection term across a wide range of parameter values and does not go to zero. When there is a contribution from ϕ_p to the individual velocities the flock is neither opaque, nor very transparent (as it is when $\phi_p = 0$). Natural starling flocks observed through simple photographic analysis are found to be in this 'marginally opaque' state [Pearce et al., 2014]. It has been conjectured that this state has the advantage of allowing members to see out of the flock approximately half the time (as $\Omega \sim 0.5$), allowing flock members in the interior, which is the safest position according to selfish herd theory, to spot predators, feeding opportunities, etc.

As in the 2D model [Pearce et al., 2014] the maintenance of the marginal opacity prevents flock dissipation, as can be seen from Fig. 2.6 c), with dissipation being obvious only when no projection term is present. This is without introducing forces of attraction and instead, being vision-based, is more directly biologically-inspired.

If the equations of motion did not promote a marginal (or full) opacity the density of the flock could reduce, leading to flock dissipation. Fig. 2.6 b) demonstrates that the model still allows for highly aligned flocks and that the region of high flock cohesion overlaps with that of marginal opacity. It is therefore possible to have highly aligned flocks with a density controlled by the projection term.

2.4.4 Model Outputs

Observed Behaviour

Trajectories

What has captivated most researchers in this area is the visualization of the flocks and the observed behaviour as each individual follows its internal equation of motion. The control parameters can be varied continuously, hence there is an infinite set of model parameter combinations. However, certain areas of the parameter space are of especial interest, because the observed trajectories have the appearance of collective animal motions we are familiar with, such as bird flocks, fish schools or insect swarms. In particular, those areas where there are both high order and cohesive flocks (see Fig. 2.11), which are properties of starling flocks and also parameter regimes that give rise to low alignment but are still cohesive, somewhat reminiscent of a swarm of midges (see Fig. 2.7).

In Figs. 2.7–2.11 snapshots of the individual positions are taken at 10 timestep intervals from $t = 50,000$ to $50,050$. When there is very little noise in the system this leads to long-lived formations as can be seen in Fig. 2.8. Interestingly the flock is thin with dense edges, which are observed traits of real flocks. When the projection
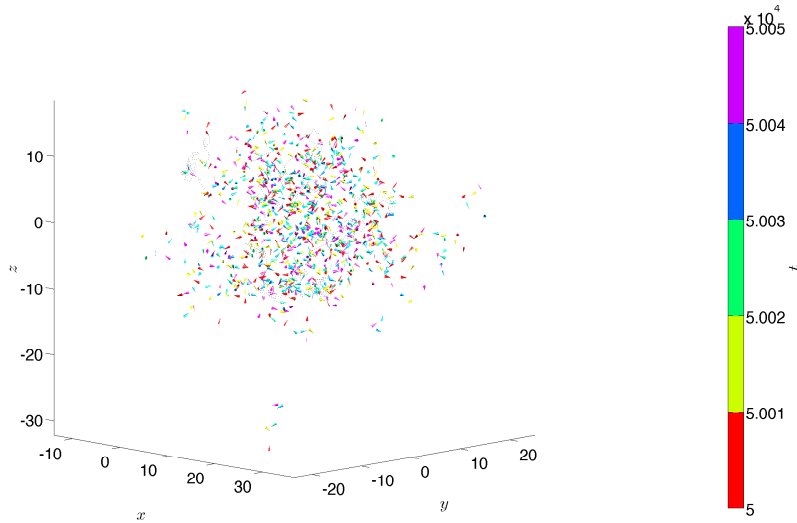
Figure 2.7: Snapshots with the number of timesteps between them $\tau = 10$, for $\vec{\Phi} = (0.0, 0.1, 0.9)$ and $N = 200$, starting at $t = 50000$ and hence the range represents 50 timesteps. The dotted lines are trajectories for 10% of the flock.

term is present, with only 1 % noise ($\phi_a = 0.01$), the flock exhibits no coherent motion (see Fig. 2.9). With equal proportions of the control parameters (ϕ_a, ϕ_p, ϕ_e), there is a clear direction of motion and cohesion, but $\vec{\Phi} = (0.333, 0.333, 0.333)$ Fig. 2.10 has considerably more directional noise in the trajectories than $\vec{\Phi} = (0.495, 0.495, 0.01)$ Fig. 2.8. In Fig. 2.11 the parameters $\vec{\Phi} = (0.8, 0.03, 0.17)$ give a diffuse but aligned flock in 2D and they also produce a flock with similar characteristics in 3D.

2.4.5   Long Time Behaviour

Centre of Mass Trajectories, Order Parameter and Measured Variable Traces
The centre of mass (c.o.m.) trajectories together with the opacity Ω, velocity order parameter Ψ, and maximum distance through the flock r_{max}, have been plotted for the parameter values used previously in the trajectories section (again with $N = 200$), because they demonstrate the variety of animal-like flocking behaviours the model can generate. See Figs. 2.12–2.16. It is clear from the c.o.m. plots that each flock goes through multiple noise-induced changes of direction, with the trajectory for $\vec{\phi} = (0.495, 0.495, 0.01)$ changing more slowly due to the very small quantity of noise (1%) (See Fig. 2.13). Hence increasing ϕ_p leads to more changes in direction for the whole flock. Clearly the directional correlation time for the flock is long with small amounts of noise and
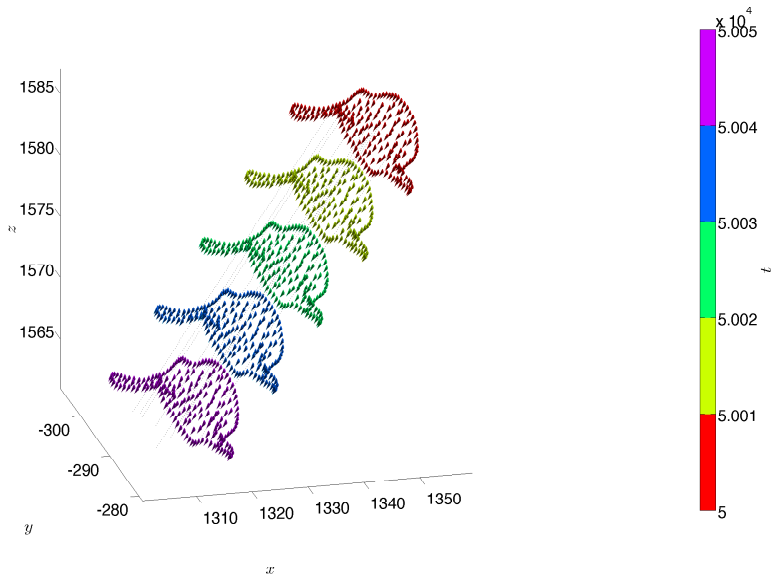
Figure 2.8: Snapshots with the number of timesteps between them $\tau = 10$, for $\vec{\Phi} = (0.495, 0.495, 0.01)$ and $N = 200$, starting at $t = 50000$ and hence the range represents 50 timesteps. The dotted lines are trajectories for 10% of the flock.
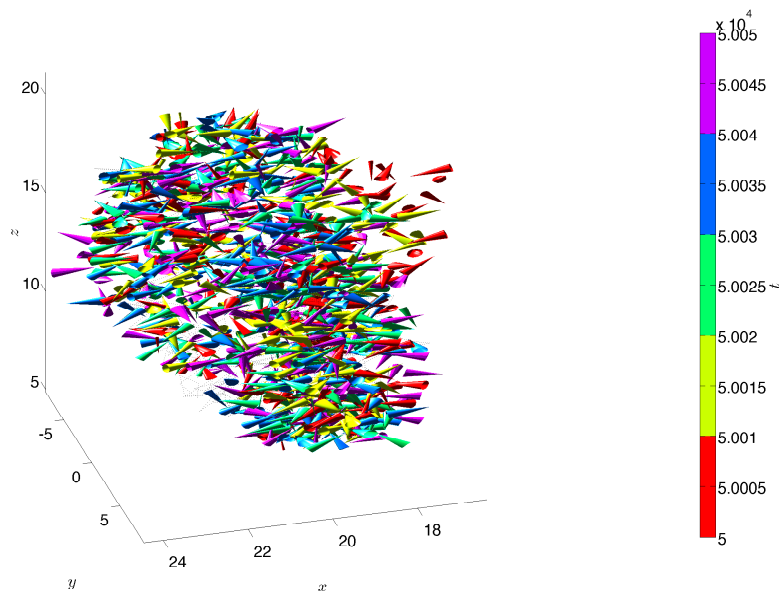

Figure 2.9: Snapshots with the number of timesteps between them $\tau = 10$, for $\vec{\Phi} = (0.0, 0.9, 0.1)$ and $N = 200$, starting at $t = 50000$ and hence the range represents 50 timesteps. The dotted lines are trajectories for 10% of the flock.
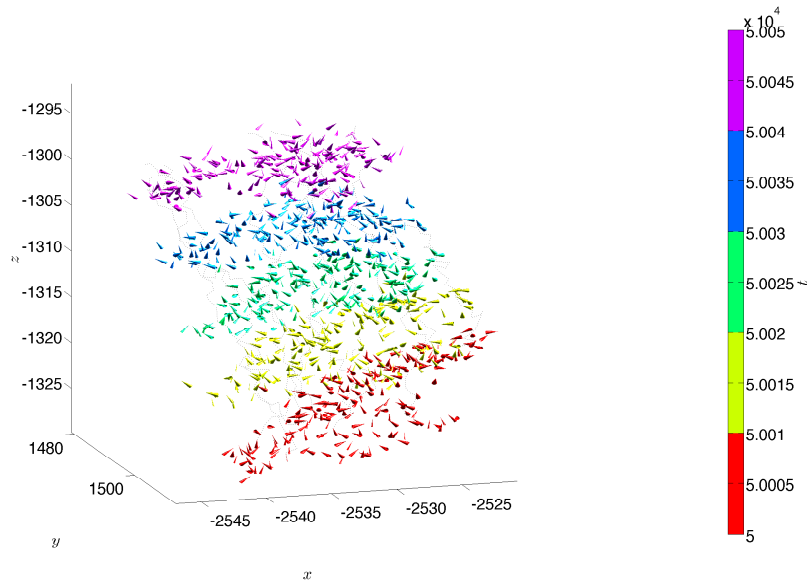
Figure 2.10: Snapshots with the number of timesteps between them $\tau = 10$, for $\vec{\Phi} = (0.333, 0.333, 0.333)$ and $N = 200$, starting at $t = 50000$ and hence the range represents 50 timesteps. The dotted lines are trajectories for 10% of the flock.
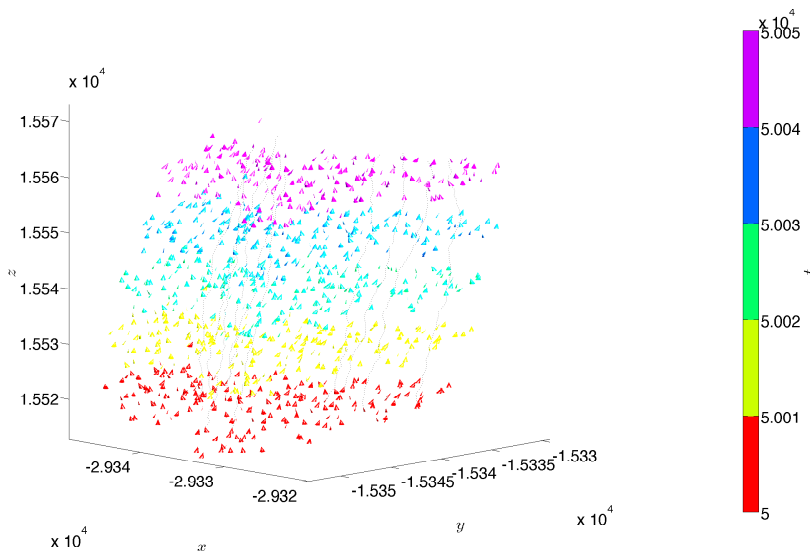

Figure 2.11: Snapshots with the number of timesteps between them $\tau = 10$, for $\vec{\Phi} = (0.8, 0.03, 0.17)$ and $N = 200$, starting at $t = 50000$ and hence the range represents 50 timesteps. The dotted lines are trajectories for 10% of the flock.

less statistically independent measurements are made in an equal number of time steps. For very small quantities of noise the behaviour is pathological as the system does not equilibrate due to these very long correlation times.

2.5   Scaling of Simulation Flock Size and Marginal Opacity

For most of the opacity parameter space diagram the value of the opacity is less than 1 but not close to 0 (i.e 'marginally opaque'). As N is increased the opacity Ω also increases. For intermediate values of N, Ω varies linearly with $1/N$ ($N > 500$ is used for the linear fit). This scaling predicts that Ω will reach a limiting value with increasing N, which is still marginally opaque (see Fig. 2.17). Whereas $r_{\max}$ increases more quickly and does not appear to approach a limiting value.

Figure 2.12: Trajectory of the centre of mass of the flock for $\vec{\Phi} = (0.0, 0.1, 0.9)$ and $N = 200$ for 150,000 timesteps. In the traces below, $r_{\max}$ is the maximum distance through the flock, Φ is the order parameter and Ω is the opacity.
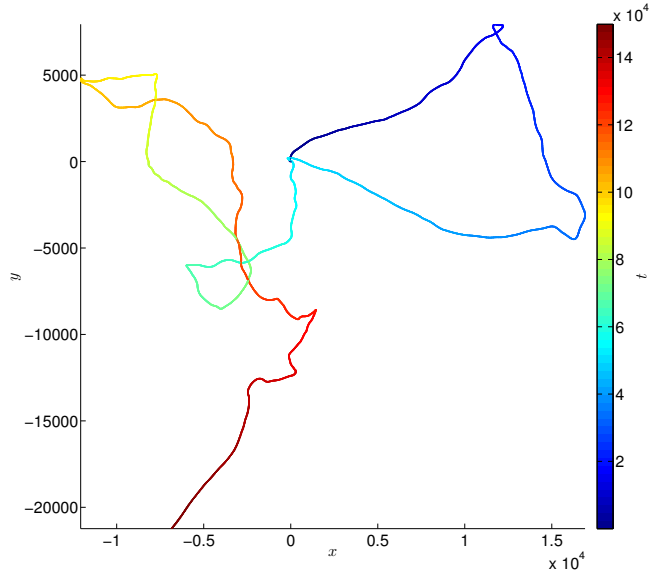
Figure 2.13: Trajectory of the centre of mass of the flock for $\vec{\Phi} = (0.495, 0.495, 0.01)$ and $N = 200$ for 150,000 timesteps. In the traces below, r_{max} is the maximum distance through the flock, Φ is the order parameter and Ω is the opacity.
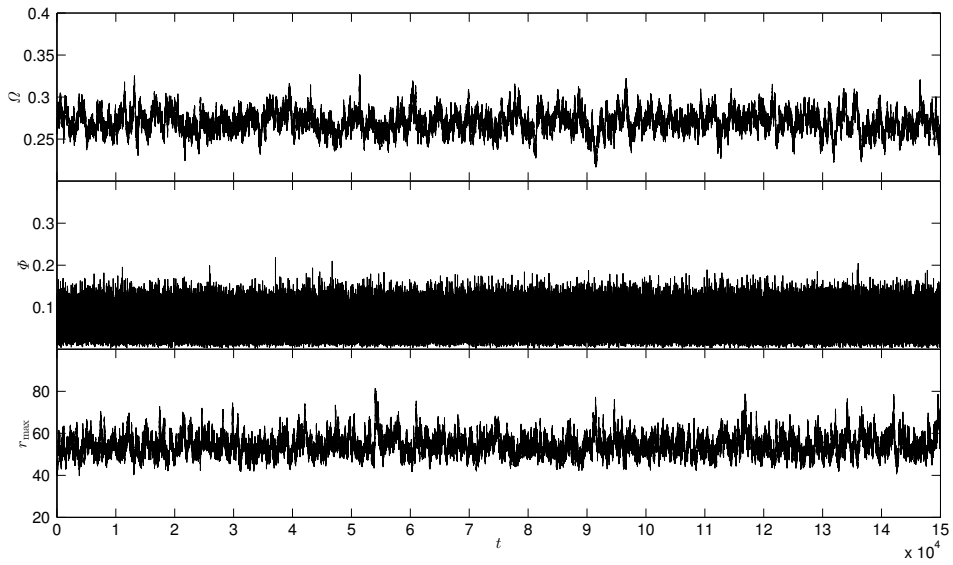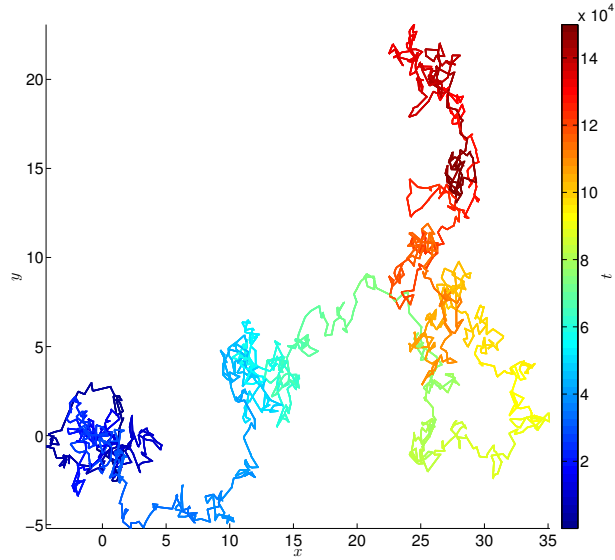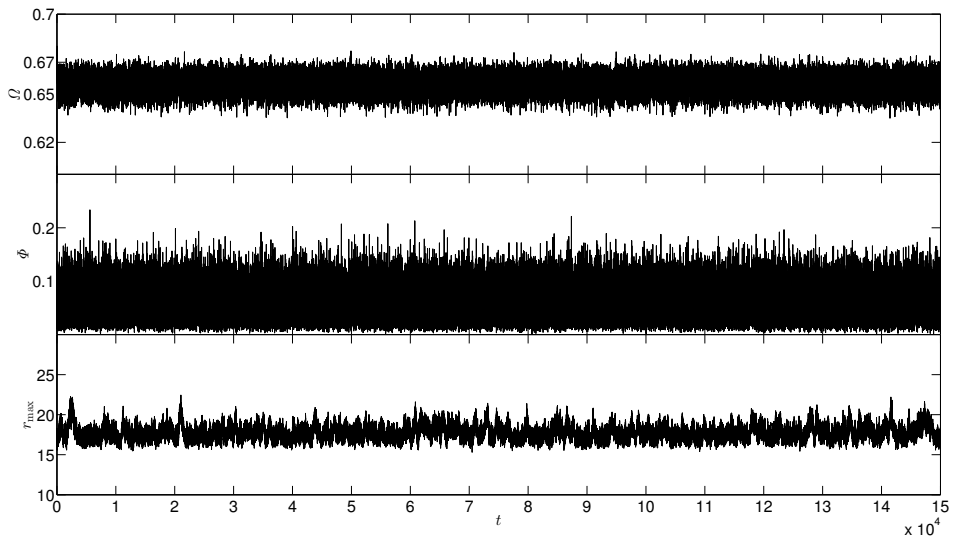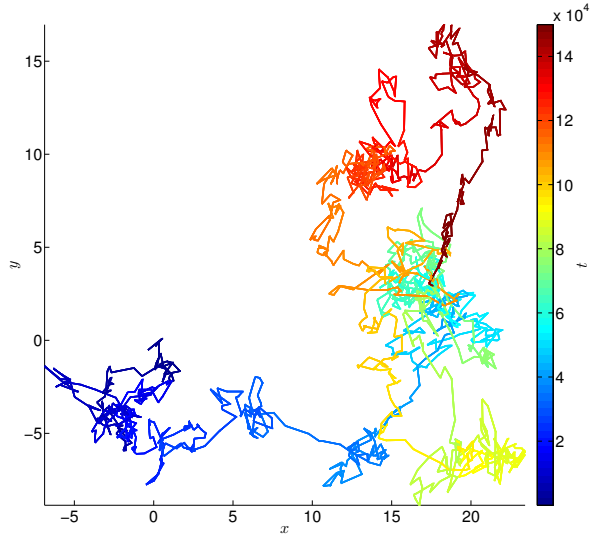
Figure 2.14: Trajectory of the centre of mass of the flock for $\vec{\Phi} = (0.0, 0.9, 0.1)$ and $N = 200$ for 150,000 timesteps. In the traces below, $r_{\max}$ is the maximum distance through the flock, Φ is the order parameter and Ω is the opacity.

45

Figure 2.15: Trajectory of the centre of mass of the flock for $\vec{\Phi} = (0.333, 0.333, 0.333)$ and $N = 200$ for 150,000 timesteps. In the traces below, $r_{\max}$ is the maximum distance through the flock, Φ is the order parameter and Ω is the opacity.
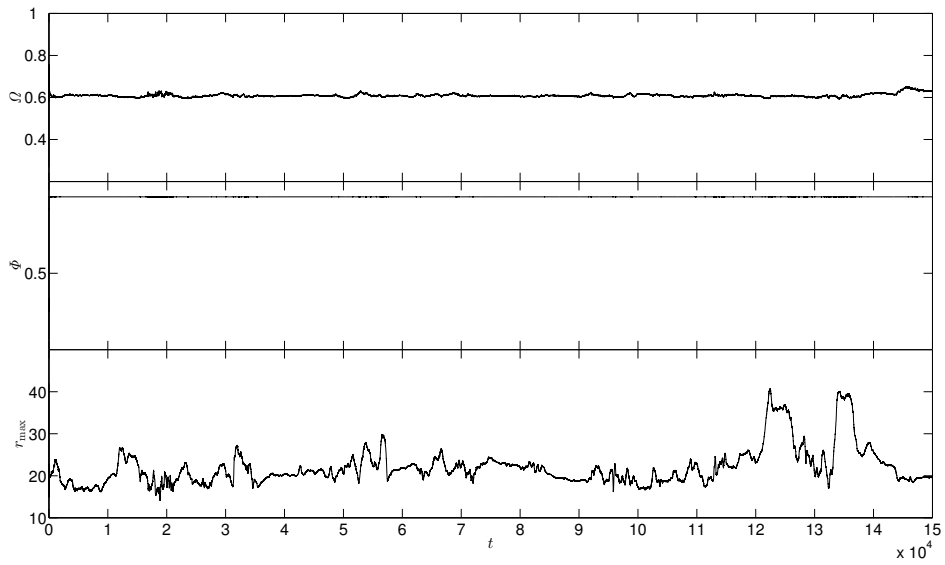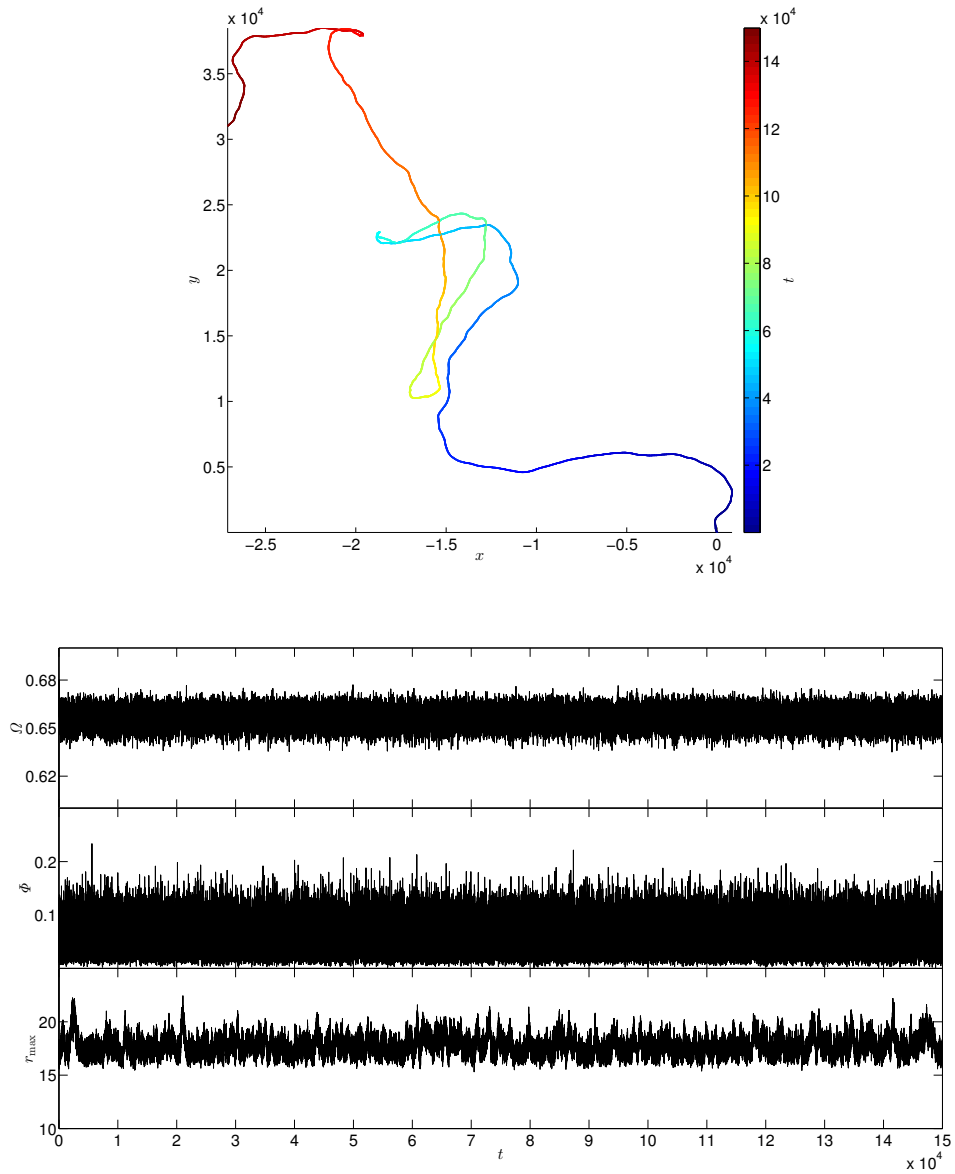
Figure 2.16: Trajectory of the centre of mass of the flock for $\vec{\Phi} = (0.8, 0.03, 0.17)$ and $N = 200$ for 150,000 timesteps. In the traces below, $r_{\max}$ is the maximum distance through the flock, Φ is the order parameter and Ω is the opacity.
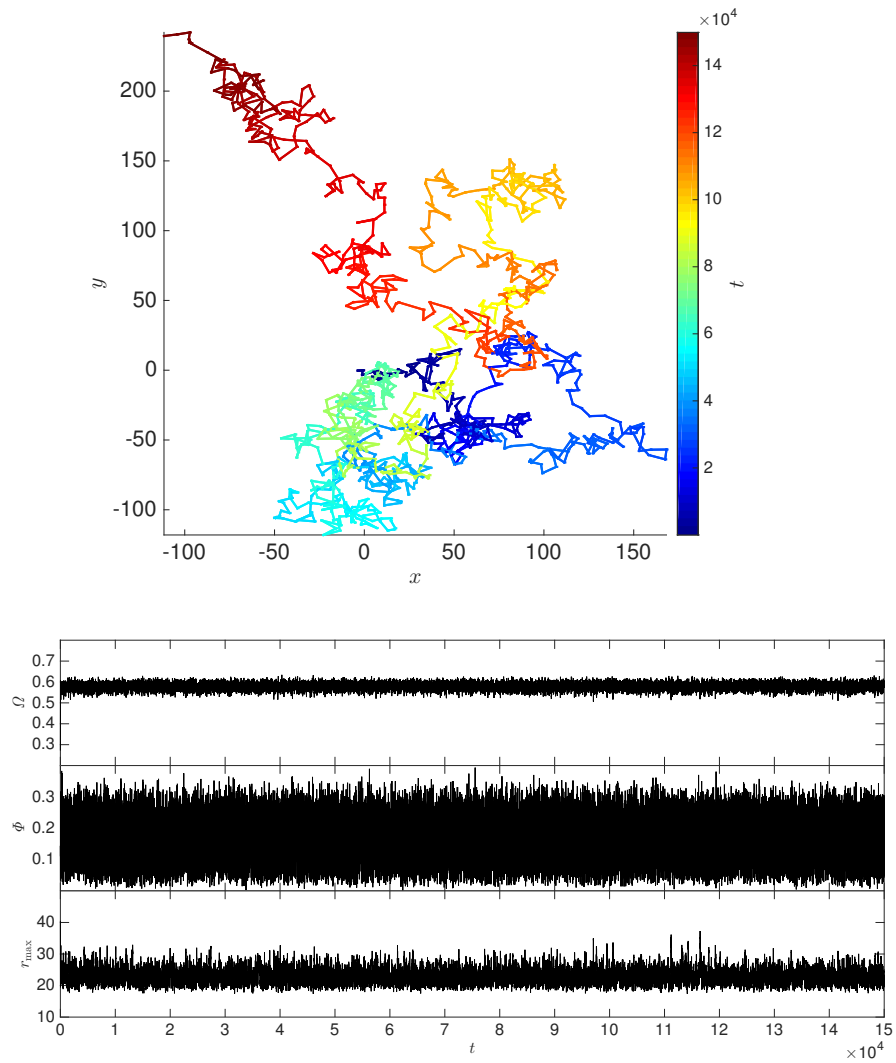
47
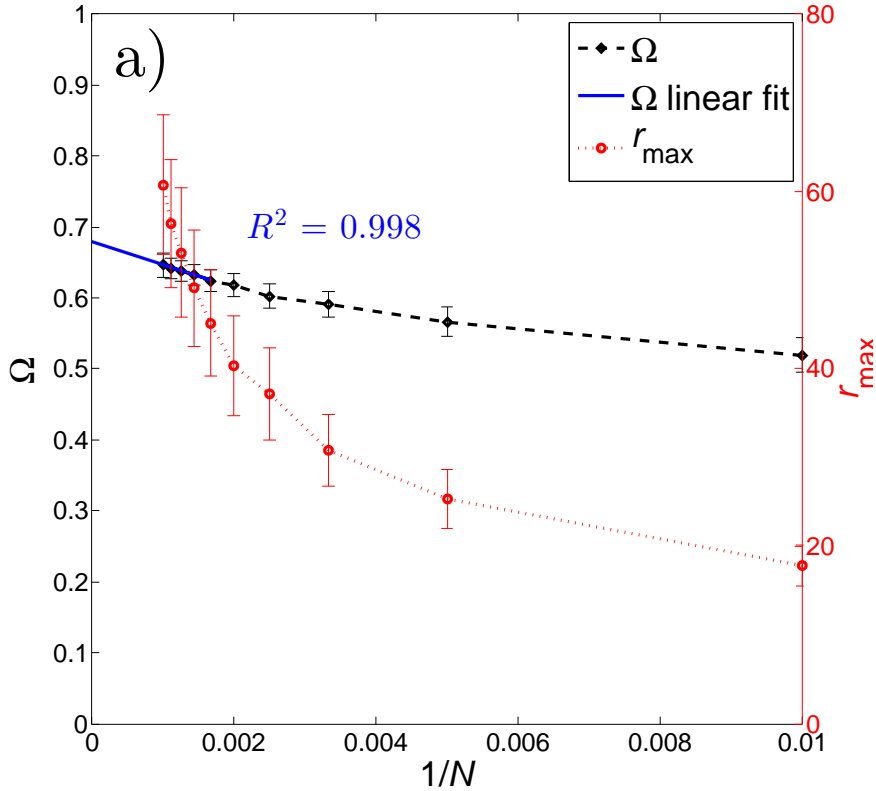
Figure 2.17: Opacity, Ω, scales as $1/N$ for large simulated flocks, whereas the flock size, $r_{\max}$, scales more slowly. The linear fit to the simulated Ω is for $N > 500$. $\vec{\phi} = (0.8, 0.03, 0.17)$ The error bars are the standard deviation for the pooled data from 5 runs.

2.6 Comparison with Empirical Data

There are two 3D flock property data sets from the STARFLAG group. One from each of the Ballerini papers. The control of the flock size by the $\vec{\delta}_{p,i}$ is a key feature of the model and a good comparison between simulated and natural flocks for the scaling of $r_{\max}$ with number of flock members N is suggestive that the model is capturing the nature of the cohesion interaction in natural flocks.

1. Ballerini et al. [2008a] The first data set is for $r_{\max}$ or the maximum linear distance between two individuals in the flock and was measured during the simulations. This is a global property of the flock and is the most directly comparable between

empirical and simulated measurements. There are also more empirical data points available.

2. Ballerini et al. [2008b] The second data set is for r_1 the (average) nearest neighbour distance. This data was calculated after adjusting for edge effects, using an improved Hanisch method (weights based on the distance to the border of the flock). This requires calculation of the alpha-shape for the flock.

The following analyses use linear least square fits to the data and logs of the data. The errors on the inferred parameters are the standard errors.

2.6.1 Predicted Scaling of the Linear Flock Size $r_{\max}$

A linear flock size R for a spherical flock is a 1D measure of flock size and would be simply the radius. For the case of a non-spherical flock a linear flock size is defined here as $r_{\max}$, i.e. the maximum distance between any 2 individuals in the flock $\max_{ij}(r_{ij})$. It is predicted from a simple mean field argument that R the linear flock size should increase as a power of N, from the assumption of maintaining marginal opacity.

$$r_{\max} \propto N^x \tag{2.23}$$

The mean field argument goes as follows. Consider a line of sight out from near the centre of a homogeneous, isotropic flock. The probability that the chosen line of sight contains only sky and no individuals is Poisson distributed

$$P_{\text{sky}} = e^{-\rho b^{d-1} R} \tag{2.24}$$

b is the radius of an individual (or other linear measure of cross-sectional area) and $\rho = N/R^d$ for a d-dimensional density and linear flock size R.

The hypothesis of marginal opacity is that P_{sky} is not 1 (i.e. the flock is fully transparent) or 0 (fully opaque), but by definition is still $\mathbb{O}(1)$, a half say. The assumption of marginal opacity leads to

$$\rho \sim N^{-1/(d-1)} \tag{2.25}$$

or $\rho \sim N^{-1/2}$ in 3D. Assuming the linear flock size $R \sim r_{\max}$ then in 3D

$$\rho = \frac{N}{R^3} \quad \sim \quad N^{-1/3} \tag{2.26}$$

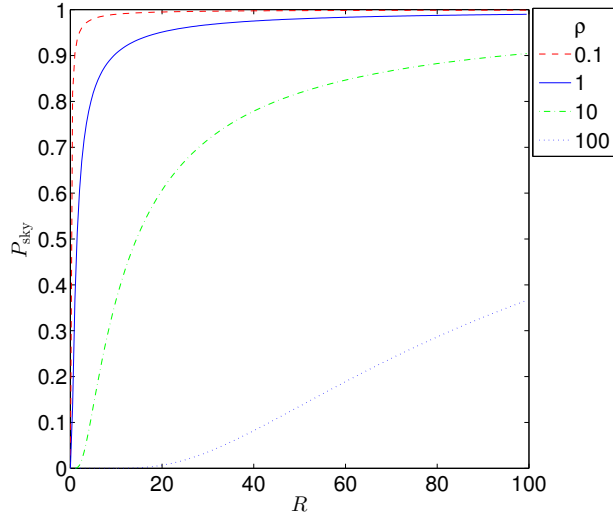$$\Rightarrow N^{1/2} \quad \sim \quad R \tag{2.27}$$

Figure 2.18: As the linear size R increases, a random arrangement of particles with fixed density transitions from a highly opaque state to a highly transparent state (as measured by the probability of seeing sky from the centre of the aggregation).

That bird flocks are not fully transparent ($\Omega << 1$) or opaque ($\Omega \sim 1$) is surprising. Firstly, because in an effectively infinite space, there is plenty of room to create an almost transparent flock and secondly if a 'metric' type interaction was used for flock cohesion, N would not need to be very large before the flock is almost fully opaque. For $b = 1$, comparable to the flock simulations, P_{sky} is plotted in Fig. 2.18. Increasing R at fixed density directly increases N. The figure shows that as the linear size R increases at a fixed density, a random arrangement of particles will transition from a highly opaque (small P_{sky}) to a highly transparent (large P_{sky}) state with a relatively small increase in R.

We will next test the predicted scaling of r_{max} for simulated and empirical data. A direct measurement of the scaling exponent x can be obtained from the gradient of a linear least square fit to the simulated and empirical data on a log-log plot. For the simulated r_{max} in Fig. 2.19a the exponent is found to be close to $1/2$, but just outside the 1σ error bounds, $x = 0.516 \pm 0.007$. The $R^2 = 0.999$ which is almost 1, resulting in this small error. The log-log estimate of the empirical x is $x = 0.61 \pm 0.072$ (see Fig. 2.19a). The error is $\sim 10\times$ larger than for the simulated x, due to the intrinsic noisiness of the data. The lower of the error bounds is 0.54. Once again, a scaling of a little over a half is plausible. We wouldn't expect to find the exact predicted scaling in either case, due to the model being mean field and the simulations are finite-sized. Also both
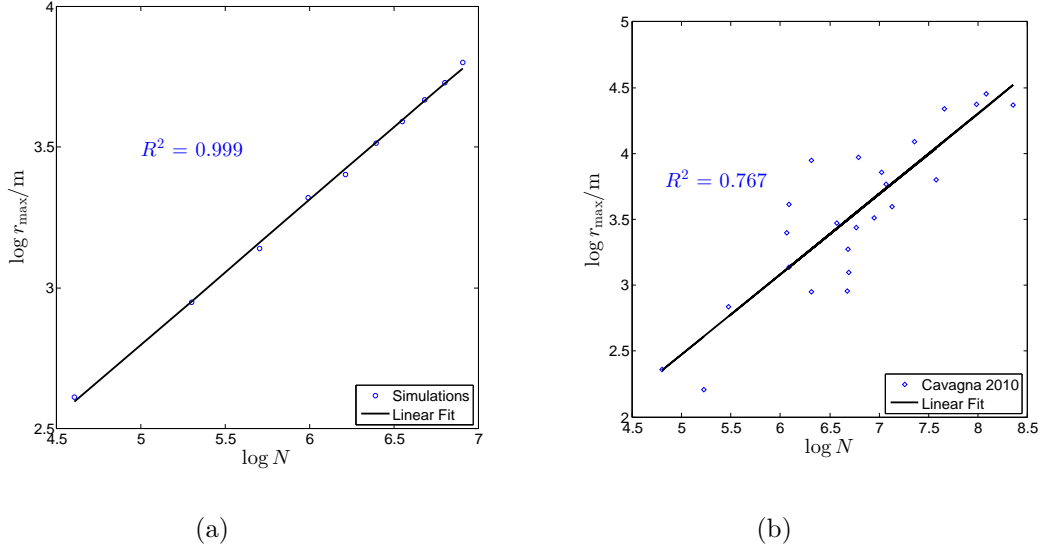
50

Figure 2.19: Calculating the $r_{\max}$ scaling with N from flocks simulated using the model described ($\vec{\phi} = (0.8, 0.03, 0.17)$) a) and empirical data from Ballerini et al. [2008a] b). The scaling of $r_{\max}$ with N can be inferred from the gradient of the plots. Hence $r_{\max} \propto N^x$ where in a) $x = 0.516 \pm 0.007$ and b) $x = 0.61 \pm 0.072$. Fitted values are $\mu \pm 1\sigma$.

the simulated and empirical flocks will be influenced by finite size effects and non-linear contributions from the interactions between individuals.

From Fig. 2.20a, the empirical $r_{\max}$ data appears to be linear in $\sqrt{N}$ as predicted for the maintenance of 'marginal opacity' ($R^2 = 0.78$). This also appears to be true for the simulated data ($R^2 = 0.998$). There is considerably more variance in the empirical data, which cannot be ascribed to the measurement accuracy, but is probably from the more complex flocking behaviours exhibited by birds in the natural environment as opposed to the simulated one. For birds at a distance of $100\,\mathrm{m}$, the average distance of flocks from the cameras in the study, the error in absolute distance is $0.14\,\mathrm{m}$, hence the maximum error in the empirical $r_{\max}$ is $\sim 0.28\,\mathrm{m}$ under average conditions.

The empirical $r_{\max}$ has dimensions in metres, whereas the simulation results are necessarily non-dimensional. Both appear to scale linearly with $\sqrt{N}$ as predicted. However $1\,\mathrm{m}$ is not necessarily the characteristic length scale for the non-dimensionalisation of the empirical data. To compare the simulated data and the empirical data it is reasonable to treat the characteristic length scale as a fittable parameter and to use a least squares minimization to find the best fit with the simulated data.

From the mean field argument and simulation, $r_{\max}$ in model flock densities scales

(a)   (b)
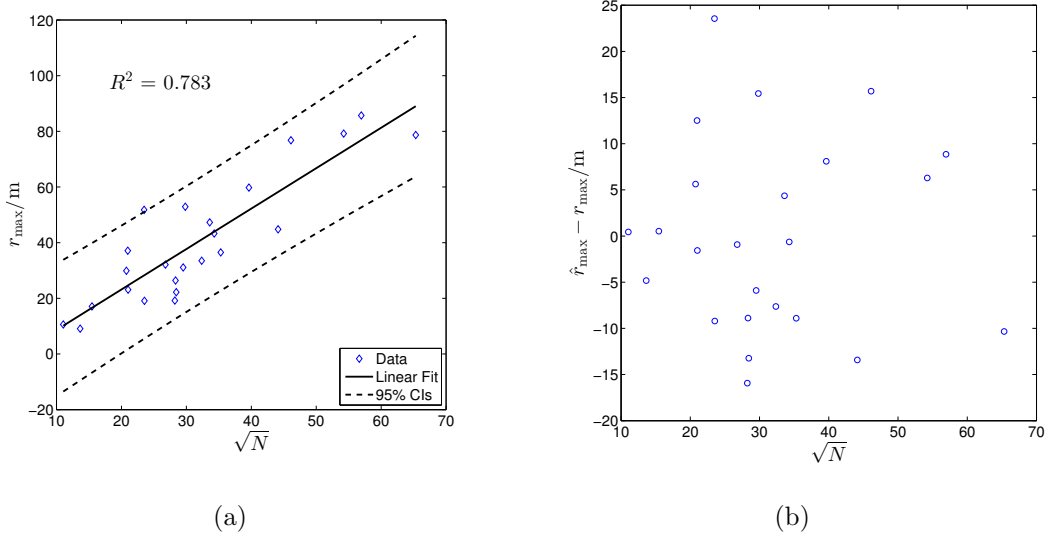
Figure 2.20: Testing $r_{\max} \sim N^{1/2}$ for the empirical data of Ballerini et al. [2008a] a) 78% of the variation of $r_{\max}$ with $\sqrt{N}$ can be explained by a linear model. Only one point lies outside the 95% confidence interval which is as expected for 24 data points. b) The residual plot appears random, which implies a good fit for the linear model.

linearly with $\sqrt{N}$. Hence we can carry out a least squares fit to the simulated data. As stated above the empirical flock $r_{\max}$ also scales linearly with $\sqrt{N}$. Hence our linear models for the simulated $\bar{r}_{\max}$ and empirical $r_{\max}$ are

$$\bar{r}_{\max} = m_s \sqrt{N} + b_s + \epsilon_s \tag{2.28}$$

$$\frac{r_{\max}}{[\text{m}]} = m_e \sqrt{N} + b_e + \epsilon_e \tag{2.29}$$

where the ϵs are noise terms (assumed to be Gaussian). The simulated $\bar{r}_{\max}$ is non-dimensionalised and this is represented by the over bar. Hence for direct comparison the empirical $r_{\max}$ must also be non-dimensionalised by dividing through by the unit (m).

Estimates for the gradient coefficients $\hat{m}_s$, $\hat{m}_e$ and intercepts $\hat{b}_s$, $\hat{b}_e$ can be obtained by simple linear regression, resulting in our best estimates for the fits, where the over hat denotes an estimated quantity.

$$\bar{r}_{\max} = \hat{m}_s \sqrt{N} + \hat{b}_s \tag{2.30}$$

$$\frac{r_{\max}}{\text{m}} = \hat{m}_e \sqrt{N} + \hat{b}_e \tag{2.31}$$

To place the linear fits directly on top of each other for comparison and to estimate the

scaling parameter, we subtract these two equations and rearrange

$$\bar{r}_{\max} = \frac{r_{\max}}{[\,\mathrm{m}\,]} + \hat{m}_e \left(\frac{\hat{m}_s}{\hat{m}_e} - 1 \right) \sqrt{N} + \hat{b}_s - \hat{b}_e \qquad (2.32)$$

we will set $c_{\mathrm{shift}} = \hat{b}_s - \hat{b}_e$ and the scaling factor between the simulation and experiment is given by the ratio of the gradients $m_e/m_s = L$. This is the characteristic length scale of the empirical flock, which is not present in the simulated flock due to the 'phantom' nature of the individuals, i.e. there are no contact / space exclusion effects in the model (other than those that enter indirectly though the projection term). Hence the transformation is

$$\bar{r}_{\max} = \frac{r_{\max}}{[\,\mathrm{m}\,]} + \sqrt{N}\frac{1-L}{L} + c_{\mathrm{shift}} \qquad (2.33)$$

where $\bar{r}_{\max}$ is the non-dimensionalised quantity, L the characteristic length scale and c_{shift} the change in the $\bar{r}_{\max}$ intercept. Note that c_{shift} is also a fitted parameter.

The scaling hypothesis for simulation and experiment was tested in Fig. 2.17, where $r_{\max}$ is plotted against $\sqrt{N}$. The linear fit for the simulated flock $r_{\max}$ has an $R^2 = 0.998$ and essentially all the variance in $r_{\max}$ is described by the predicted scaling with $\sqrt{N}$. In the same figure, linearly rescaled empirical $r_{\max}$ data is also plotted, which also scales linearly with $\sqrt{N}$ and has an $R^2 = 0.763$, which is a very good fit considering all the confounding factors in real flocks (such as the anisotropy of directions, such as up and down, lighting, etc).

Using a standard method of error calculation for a function f with two variables, a, b:

$$\sigma_f^2 = \left(\frac{\partial f}{\partial a} \right)^2 \sigma_a^2 + \left(\frac{\partial f}{\partial b} \right)^2 \sigma_b^2 \qquad (2.34)$$

an error estimate for L can be made from the standard errors on the regression coefficients.

$$\sigma_L^2 = \frac{1}{\hat{m}_{\mathrm{s}}^2}\sigma_{\hat{m}_{\mathrm{e}}}^2 + \frac{\hat{m}_{\mathrm{e}}^2}{\hat{m}_{\mathrm{e}}^4}\sigma_{\hat{m}_{\mathrm{s}}}^2 \qquad (2.35)$$

The least square fit estimate is $L = 1.015 \pm 0.115\,\mathrm{m}$. Thus $0.90\,\mathrm{m} \le L \le 1.13\,\mathrm{m}$. The average body length of a starling is $0.2\,\mathrm{m}$ and the wingspan $0.4\,\mathrm{m}$. So a characteristic length scale of the order of $1\,\mathrm{m}$ is not unreasonable. The characteristic length scale could reasonably be expected to be related either to the distance travelled in a timestep, i.e. $\propto 1/\langle v \rangle$, where $\langle v \rangle$ is the average velocity in the natural flock, or related to the average size of a starling. As these factors control the relative size of the natural flock to the simulated flock. The simulated flock members travel their radius in a timestep and the
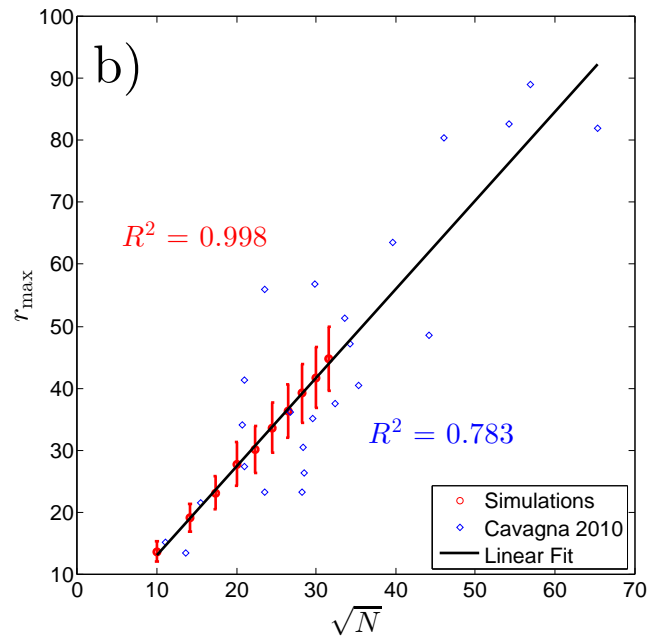
Figure 2.21: $r_{\max}$ from simulation and from the empirical study of Cavagna *et al* scales linearly with $\sqrt{N}$, as predicted to obtain marginal opacity in 3D [Cavagna et al., 2010]. The empirical $r_{\max}$ has been non-dimensionalised using a characteristic length scale fitted to the simulated $r_{\max}$ of $1.015 \pm 0.115\,\mathrm{m}$ (plus a y-axis shift to align the linear fits). The simulations are consistent and provide a very good linear fit ($R^2 = 0.998$).
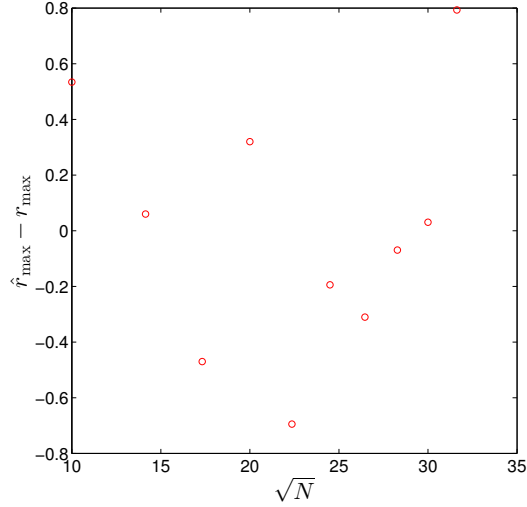
Figure 2.22: The residuals for the fit of the linear model for the simulated r_{max} to $\sqrt{N}$ Eqn. 2.30 appear random, implying a good linear fit to the simulated $\bar{r}_{max}$ values.

natural flock members exclude their own volume (plus, in practice, a safety margin). Hence finding a characteristic scaling of the same order as a starling's dimensions is unsurprising.

For all the linear fits the residuals are found to be from the normal distribution using the Anderson-Darling test at the 5% significance level, with a null hypothesis H_0 that the underlying distributionof the residuals is normal (see Table 2.4). Hence the assumption of normally distributed errors for linear regression holds for the fits made here. It was previously verified that the opacity of both simulated and natural starling flocks scale as predicted by the model. It has been verified here that $\bar{r}_{max}$ also scales as predicted by the model in both simulated and natural flocks. This was not obviously the case, as we will see later in §2.6.3 that natural flocks are very flat (hence $\bar{r}_{max}$ is along an extended direction) and that certain parameter regions of the simulations are similarly anisotropic.

2.6.2 Density

Ballerini et al. [2008b] estimated natural flock densities from the α-shape by dividing the volume by the number of internal points, varied widely across the flock but was uncorrelated with the number of birds. However they did find that the density was related to the nearest neighbour distance, or 'sparseness' as $\rho = r_1^{-3}$.

Table 2.4: p-values for the Anderson-Darling test on the distribution of the residuals from the linear fits. H_0 is that the underlying distribution is normally distributed. The p-value is the probability of the data given the hypothesis H_0, hence rejection at the 5% significance level would occur if $p \leq 0.05$. Therefore the null hypothesis that the distributions of the residuals are normally distributed is accepted in all cases (this is an assumption of linear regression which is satisfied here).

	Variables		
Type	Independent	Dependent	p-value
Simulated	$\sqrt{N}$	$r_{\max}$	0.987
Empirical	$\sqrt{N}$	$r_{\max}/\,\mathrm{m}$	0.599
Simulated	$\log N$	$\log(r_{\max})$	0.694
Empirical	$\log N$	$\log(r_{\max}/\,\mathrm{m})$	0.954

The empirically observed flocks had convexities defined as V_α/V_H that were greater than 0.63 with mean 0.82 ± 0.04 [Ballerini et al., 2008b]. The observed values for $\vec{\phi} = (0.8, 0.03, 0.17)$ which is considered to be a bird-like flock phenotype and the closely valued $\vec{\phi} = (0.9, 0.0, 0.1)$ are just outside the empirical range. Only $\vec{\phi} = (0.0, 0.1, 0.9)$ is within the empirical range and this is a phenotype that appears more midge-like than starling-like. The other 2 parameter regimes, which have greater ϕ_p, have a convexity that is somewhat smaller than the observed flocks. It is of course unknown how much of an effect external stimuli has on the convexity of the flock, but observations of flocks responding to predation demonstrate this can be considerable.

The flock density ρ is defined as N_I/V_α, where N_I is the number of interior points and V_α the volume of the α-complex. Empirically $0.04 < \rho < 0.80$ with mean 0.27 ± 0.08. The simulated densities fell within this range, except for $\vec{\phi} = (0.9, 0.0, 0.1)$ which with $\phi_p = 0$ was able to dissipate (i.e. there is no flock cohesion and the flock breaks apart) and hence obtain a very small density. $\vec{\phi} = (0.495, 0.495, 0.01)$ has the closest density to the mean, but these flocks are very thin and flat and come from a pathological region of the parameter space with very low noise and are interesting from the point of view of model behaviour, but do not correspond to natural starling flocks.

Table 2.5: Mean $\pm$ SE for properties related to the density of the flock, calculated for $N = 1000$ and adjusting for border bias. r_1 is the nearest neighbour distance or sparseness; V_α and V_H, the volumes of the α-shape complex and convex hull; N_E is the number of points on the edge of the flock; ρ is defined as the number of interior points divided by the volume of the α-shape complex; V_α/V_H is a measure of the concavity of the flock.

	r_1	α	V_α	N_E	V_H	ρ	V_α/V_H
$(0, 0.1, 0.9)$	2.123 ± 0.004	112.0 ± 0.5	93000 ± 100	175.6 ± 0.2	134300 ± 200	0.0089 ± 0.0000	0.6947 ± 0.0003
$(0.333, 0.333, 0.333)$	0.52 ± 0.01	15.5 ± 0.1	4900 ± 40	720 ± 1	16000 ± 50	0.0558 ± 0.0001	0.309 ± 0.001
$(0.9, 0.0, 0.1)$	19 ± 2	2500 ± 100	$4 \times 10^7 \pm 4.0 \times 10^6$	470 ± 20	$6 \times 10^7 \pm 5 \times 10^6$	0.0000 ± 0.0000	0.62 ± 0.02
$(0.495, 0.495, 0.01)$	0.79 ± 0.01	500 ± 100	2800.4597 ± 400	460 ± 30	17000 ± 1000	0.22 ± 0.02	0.18 ± 0.04
$(0.8, 0.03, 0.17)$	$1.7 \pm 0.5^{\,5}$	60 ± 20	14700 ± 900	290 ± 40	24600 ± 700	0.0484 ± 0.001	0.600 ± 0.006

2.6.3 Morphology: Anisotropy in Flock Dimensions

Studies of birds and fish show them to have flocks and schools that are not generally spherical (the bait ball formed by mackerel species being an obvious exception). Hence the flocks have different extensions in different directions. There are two obvious possibilities for the cause of this anisotropy in birds: gravity and the prevailing average flock direction. Gravity defines a direction in a 3D basis that is different to the other two perpendicular directions for natural bird flocks. The effect of gravity is neglected in the model used here. However the effect of the prevailing flock direction (or average velocity) can be investigated and the anisotropy is quantified by analysing the magnitude of the dot product with the flock's principal directions.

Ballerini et al. [2008b] define the principal dimensions I_1, I_2 and I_3 as follows. I_1 is the diameter of the largest sphere contained within the flock boundary. The principal direction associated with this, $\vec{I_1}$, was defined as perpendicular to a plane least-squares fitted through the flock. They then defined I_2 as the largest circle inside a projection of the flock onto the previously defined plane. The projection of the flock onto the plane was then least-square fitted to a line on that plane to define $\vec{I_3}$. $\vec{I_2}$ is perpendicular to $\vec{I_1}$ and $\vec{I_3}$ and is in the fitted-plane. I_3 gives the greatest extension of the flock and $I_1 \leq I_2 \leq I_3$. Note these directions define an orthonormal basis.

This definition of the principal directions of the flock doesn't relate simply to the principal dimensions and a different definition is used here. That is the principal directions are defined as the principal components (eigenvectors) . The principal components are defined as the normalized eigenvectors of the covariance matrix, Σ, and hence also define an orthonormal basis for the flock positions. For the 3D point cloud from the instantaneous flock member positions

$$\Sigma = \begin{pmatrix} \text{cov}(r_x, r_x) & \text{cov}(r_x, r_y) & \text{cov}(r_x, r_z) \\ \text{cov}(r_y, r_x) & \text{cov}(r_y, r_y) & \text{cov}(r_y, r_z) \\ \text{cov}(r_z, r_x) & \text{cov}(r_z, r_y) & \text{cov}(r_z, r_z) \end{pmatrix} \tag{2.36}$$

for the random variables formed from the components of the position vectors $\vec{r_i}$. The eigenvalues are the variance along these principal components and their square roots are defined as the associated dimensions.

$$\Sigma \vec{I_k} = I_k^2 \vec{I_k} \tag{2.37}$$

where $\vec{I_k}$ are the principal directions and I_k the associated dimensions. The first principal
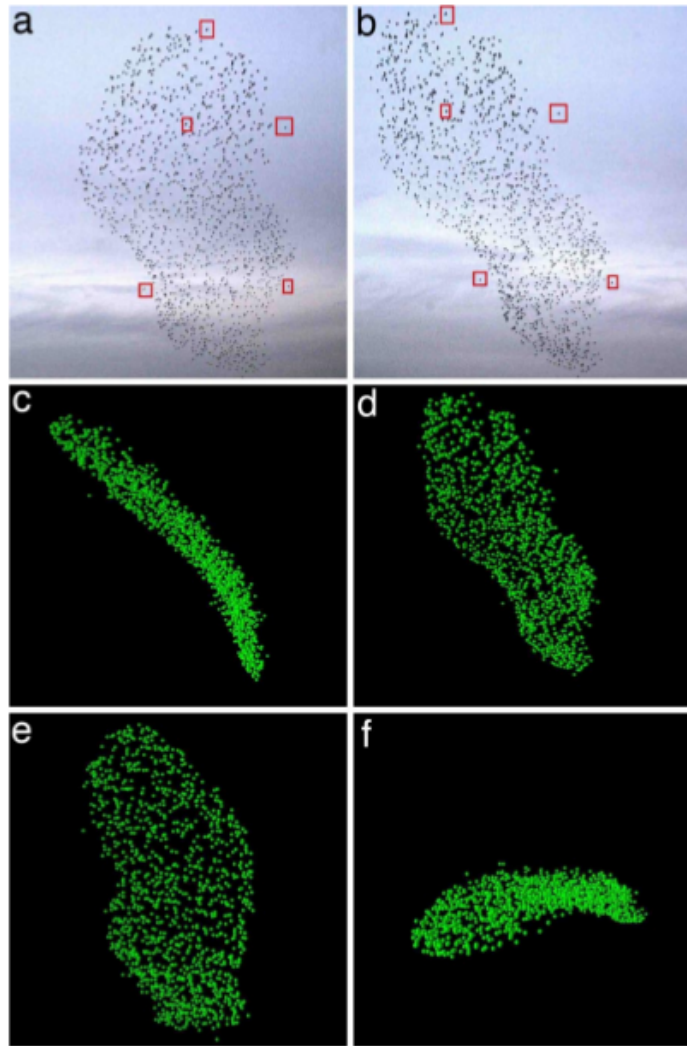
Figure 2.23: A 'typical' flock as determined by Ballerini et al. [2008a]. a, b are the stereo pair photographs and c–e views of the 3D reconstruction. Note how flat the flock appears in the reconstruction.

component points along the direction that minimizes the distance from its axis to all points in the point cloud and is analogous to $\vec{I_3}$. The second principal component is analogous to $\vec{I_2}$ and the third to $\vec{I_1}$. By defining the dimensions as the square root of the associated eigenvalues, these are measures of mean deviation as opposed to maximal in these directions and are decidedly different to the previous measurements. For instance if there is a very large flat flock with a round bulge, I_2 as previously defined could be very large (depending on the size of the bulge), whereas I_2 as defined here would be close to the mean deviation. It is perhaps not obvious what the correct measure should be, but this method is very fast (as it is an eigenvalue problem and can be solved efficiently). Also what we are looking for is the qualitative behaviour, i.e. that flocks tend to be slightly flat and thin (at least according to Ballerini et al. [2008b]), with the plane parallel to the ground. It is contrary to observed experience, but it is probable that this is a perceptive trick caused by observing flocks from a tilted visual projection. The inability to distinguish near and far birds easily means like in the model we are seeing a projection onto our view and lose information about the aspect ratio of the flock (the brain then reconstructs a 'plausible' flock shape). Thus the thin aspect of the flock is lost. Flying parallel to the ground on average makes sense, as every time a bird dips they lose gravitational potential energy and hence must expend energy to reach their previous height [Ballerini et al., 2008b].

Table 2.6: Mean ± standard error for principal dimensions of $N = 200$ flock, calculated from an eigenvalue analysis of the covariance matrix Σ for the position vector components. 5 repeats with a 20,000 timestep equilibration period and 120,000 step measuring period were used.

ϕ_a	ϕ_p	ϕ_e	I_3	I_2	I_1	L_3/L_1	L_2/L_1	$|\vec{e}_1 \cdot \vec{v}_\mathrm{av}|$	$|\vec{e}_2 \cdot \vec{v}_\mathrm{av}|$	$|\vec{e}_3 \cdot \vec{v}_\mathrm{av}|$
0	0.1	0.9	8.7296 ± 0.0121	7.9014 ± 0.0079	7.1390 ± 0.0028	1.2256 ± 0.0015	1.1087 ± 0.0008	0.5004 ± 0.0003	0.4997 ± 0.0003	0.5000 ± 0.0004
0	0.9	0.1	4.6598 ± 0.0029	3.8052 ± 0.0026	1.0727 ± 0.0009	4.4010 ± 0.0044	3.5953 ± 0.0037	0.4421 ± 0.0005	0.4525 ± 0.0002	0.5955 ± 0.0004
0.3333	0.3333	0.3333	7.7433 ± 0.0238	4.3723 ± 0.0072	1.4735 ± 0.0024	5.7734 ± 0.0159	3.2957 ± 0.0096	0.3052 ± 0.0022	0.2693 ± 0.0006	0.8502 ± 0.0009
0.495	0.495	0.01	6.1166 ± 0.1121	3.0407 ± 0.0443	1.0629 ± 0.0684	7.9067 ± 0.5291	3.7418 ± 0.2108	0.6543 ± 0.0145	0.3085 ± 0.0278	0.5205 ± 0.0325
0.8	0.03	0.17	6.0419 ± 0.0812	3.7127 ± 0.0097	2.6081 ± 0.0160	2.3812 ± 0.0503	1.4478 ± 0.0082	0.3912 ± 0.0231	0.4968 ± 0.0127	0.5922 ± 0.0184

Table 2.7: Means ± standard error for dimensions of $N = 1000$ flock, calculated from a principal component analysis. 5 repeats with a 20,000 timestep equilibration period and 80,000 step measuring period were used.

ϕ_a	ϕ_p	ϕ_e	I_3	I_2	I_1	L_3/L_1	L_2/L_1	$|\vec{e}_1 \cdot \vec{v}_\mathrm{av}|$	$|\vec{e}_2 \cdot \vec{v}_\mathrm{av}|$	$|\vec{e}_3 \cdot \vec{v}_\mathrm{av}|$
0.0	0.1	0.9	11.9638 ± 0.0103	11.3189 ± 0.0075	10.7209 ± 0.0096	1.1166 ± 0.0018	1.0563 ± 0.0007	0.5000 ± 0.0003	0.5005 ± 0.0005	0.4993 ± 0.0006
0.333	0.333	0.333	183.6644 ± 4.4073	124.1662 ± 4.7019	49.7793 ± 4.4746	3.9027 ± 0.4384	2.6149 ± 0.2610	0.4941 ± 0.1130	0.4910 ± 0.0871	0.5463 ± 0.0955
0.495	0.495	0.01	36.8018 ± 1.1940	5.0755 ± 0.3390	3.4454 ± 0.1348	10.89987 ± 0.3917	1.4888 ± 0.0440	0.9911 ± 0.0011	0.0938 ± 0.0071	0.0436 ± 0.0028
0.8	0.03	0.017	14.3247 ± 0.4239	7.5691 ± 0.1874	4.7104 ± 0.0934	3.1647 ± 0.1278	1.6524 ± 0.0585	0.4036 ± 0.0369	0.6246 ± 0.0338	0.4455 ± 0.0309 [6]
0.9	0.0	0.1	17.7148 ± 0.0887	11.2153 ± 0.0255	1.9008 ± 0.0210	10.0730 ± 0.1308	6.4875 ± 0.0538	0.2033 ± 0.0036	0.1832 ± 0.0029	0.9365 ± 0.0025

The empirical measurements of Ballerini et al. [2008b] for the mean of the dimensional ratios over all observed events are $L_2/L_1 = 2.8 \pm 0.4$ and $L_3/L_1 = 5.6 \pm 1.0$ (95% CIs) with overall aspect ratio of approximately 1:3:6. The simulated flocks containing substantial amounts of both the projection and alignment terms are also highly anisotropic in the 3 flock dimensions. The $\vec{\phi} = (0.495, 0.495, 0.01)$ flocks are very flat and for $N = 1000$ has an aspect ratio of approx. 1:1.5:11. This directional symmetry breaking in the flock dimensions is an interesting feature of the model that mirrors the empirical observations.

Due to the absence of gravity in the model, we cannot examine $|\vec{G} \cdot \vec{e}_x|$ for the 3 principal component axes, where $\vec{G}$ is the gravitational direction. It is only possible to look at the projections onto the average velocity $|\vec{v}_{av} \cdot \vec{e}_x|$. For the measured starling flocks the projection of $\vec{e}_1$, i.e. the flock thickness, was found to be 0.06–0.41 with a mean value of 0.19 ± 0.08 indicating that it does not generally point in the direction of average flock motion, but is in the range $\pi/2$ and $\pi/3$, i.e. an oblique angle to the velocity [Ballerini et al., 2008b]. The simulated values lie within this range except for $\vec{\phi} = (0.495, 0.495, 0.01)$ where the smallest dimension is closer to parallel with the flock velocity, as can be seen in Fig. 2.8 for $N = 200$ (as noted before this is in a pathological region of the parameter space). This axis is in good alignment with the average velocity for $N = 1000$ simulations at the same coefficient values, which results in the flat sheet of the flock moving perpendicularly to natural flocks.

2.6.4 Anisotropy in Nearest Neighbours

The following analyses are of the nearest neighbour angular distributions, i.e. where the nearest neighbours are found relative to the individual's velocity. The analyses use the Hanisch method to remove border bias in the nearest neighbour statistics as detailed in §2.3.2. A common measure of the relative position of nearest neighbours in a focal individual's view is the so-called bearing angle θ. This is the angle between the focal individual's velocity and the position of the nearest neighbour. If the directions to the nearest neighbour are randomly distributed in 3D around the focal individual, the distribution of θ is not uniform (see 2.24). This is because for each bearing angle θ, the possible directions at which a neighbour may be located are on a circle with radius $\sin(\theta)$ on the unit sphere. There are maximal possible directions at $\theta = \pi/2$ (a great circle) and minimal at $0, \pi$ where there is only one point. Hence there is a jacobian factor of $\sin(\theta)$ that needs to be accounted for. For determining if the distribution of θ differs from uniformly random, it is easier to work with the PDF of $\cos(\theta)$, $f(\cos(\theta))$, which is uniform
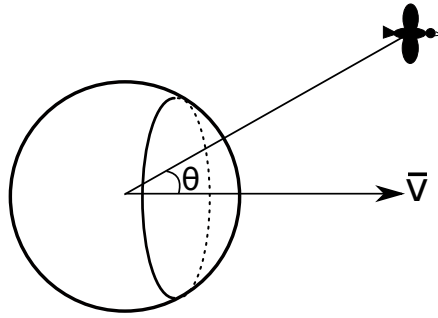
Figure 2.24: The circle defined by a given bearing angle has a greater circumference the closer θ is to $\pm\pi/2$, hence there are more positions a potential can be – a geometrical effect. This Jacobian factor must be taken into account when constructing the PDF, in this case it is simpler to use the PDF of $\cos\theta$ as it is a uniform distribution, for an isotropic neighbour distribution.

for randomly positioned nearest neighbours with $f(\cos(\theta)) = 0.5$ [Ballerini et al., 2008b]. $\vec{d_i} = \vec{v_i}/\|\vec{v_i}\|$ is the normalized velocity (i.e. direction) of the focal individual i and $\vec{u_j}$ is a unit vector in the direction of the nearest neighbour j, i.e. $\vec{u_j} = \vec{r_j} - \vec{r_i}/|\vec{r_j} - \vec{r_i}|$.

$$\cos(\theta) = \vec{d_i} \cdot \vec{u_j} \tag{2.38}$$

The observed $\cos\theta$ distributions from Ballerini et al. [2008a] show fewer nearest neighbours in front and to the rear than would be expected by chance alone, with a concomitant increase in neighbours at the side of an individual (see Fig. 2.26). One possible explanation is that collisions are best avoided by having neighbours that are not directly in front or behind, as in aligned flocks the directions of motion are likely to be very similar. However, if it is assumed that vision informs the movement rules of birds, then the anisotropic nature of the visual apparatus, such as the foveal specialisation and the blind angle behind the head, could be the cause of the anisotropy. For instance it could be argued that keeping your nearest neighbours centred in your view on the region of your visual field with greatest resolution, will allow you to best assess their position and heading to prevent collision. In laterally located eyes, the regions directly in front and behind of the head are typically at the periphery of the visual field or include blind areas and this is a dangerous place to have your nearest neighbours when avoiding collisions. It has also been suggested (although disputed) that there is an energy benefit to some anisotropic structures in animal aggregations. Famously (and particularly disputed) is the case of geese, which fly in a characteristic V-formation that may confer an aerodynamic benefit as flock members 'break the air' by creating
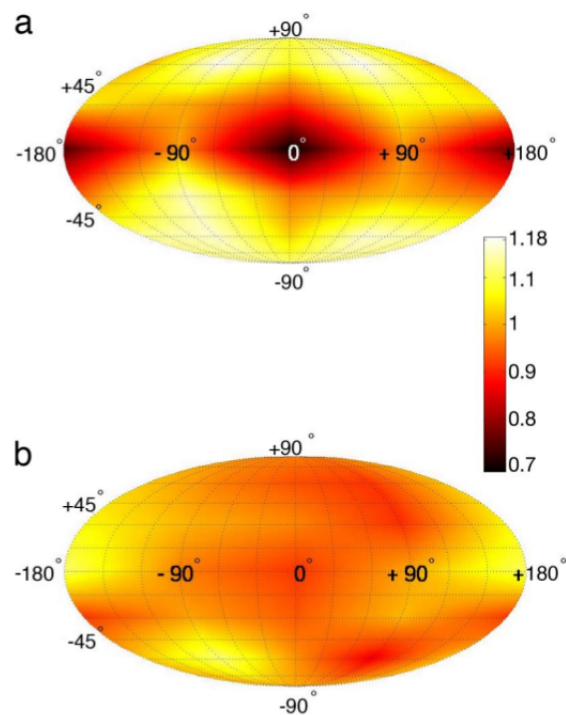
Figure 2.25: The empirical nearest-neighbour angular distribution. The plots show the density of unit vectors to the first nearest neighbour a), and tenth nearest neighbours b), for a flock of 1168 starlings [Ballerini et al., 2008a]. The angles are relative to the average flock velocity. Note the lack of neighbours in front and behind, in contrast to the early work of Major and Dill [1978] who found the nearest neighbours to be behind and below a reference bird. The discrepancy is likely to be due to the limitations of the techniques available to Major and Dill [1978]. They could only examine small flocks with a two camera set up and matching individuals between the stereo photographs was done manually. Although the discrepancy may be a real difference between small and intermediately sized natural flocks (small $\mathbb{O}(10)$, intermediate $\mathbb{O}(100)$). There are less opportunities for collision in smaller flocks, where remaining aligned may be more important for flock cohesion. Hence it could possibly be more advantageous to follow other flock members in small flocks.
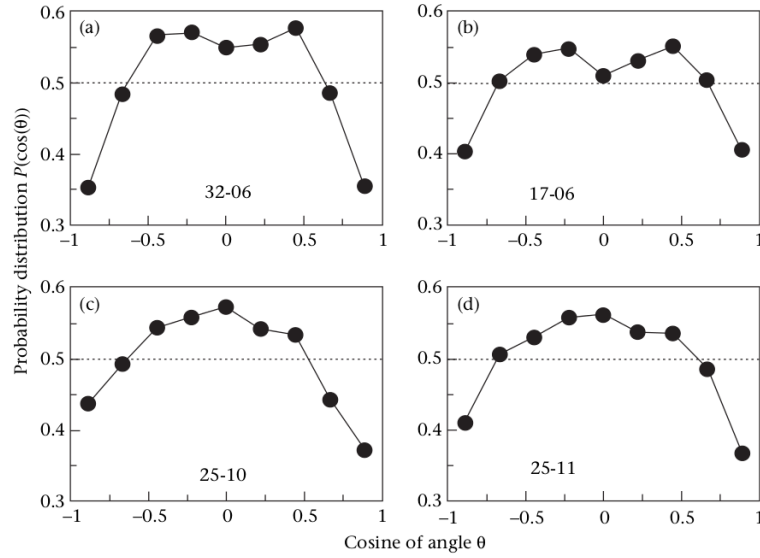
Figure 2.26: The empirical nearest neighbour $\cos\theta$ distribution for four flocking events 32-06 $N = 781$, 17-06 $N = 534$, 25-10 $N = 834$ and 25-11 $N = 1168$ [Ballerini et al., 2008b]. θ is the bearing angle, measured relative to an individual's direction of motion. Note that the distributions peak at $\cos\theta = 0$, i.e. $\theta = \pm\pi/2$ and that neighbours tend to be found at the sides, not in front or behind.

turbulence for the individuals behind them [Badgerow and Hainsworth, 1981]. More directly applicable is [Higdon and Corrsin, 1978]'s investigation of the aerodynamic effect in aggregations such as starlings. They found it to be disadvantageous for one bird to fly directly behind another, which is another possible reason for the empirical anisotropy.[7] It is still very much an open question as to whether the geometric relationship of birds is primarily determined by visual or aerodynamical considerations, but the anisotropy is clearly established.

Fig. 2.27 shows the $\cos\theta$ distributions for the first nearest neighbours for certain $\vec{\phi}$ parameter values. For each point there are tens of thousands of measurements and all the distributions differ significantly from the uniform random distribution, using a chi-squared goodness-of-fit test at the 1% level. Interestingly, for the parameters considered to appear bird-like, $\vec{\phi} = (0.8, 0.03, 0.17)$, the distribution is close to uniformly random. Less surprisingly, this is also true for high alignment and low noise, $\vec{\phi} = (0.9, 0.0, 0.1)$, as neither of the contributions should result in a preferred nearest neighbour direction. For the midge-like parameter values $\vec{\phi} = (0.0, 0.1, 0.9)$ the distribution is also close to uni-

---

[7]Interestingly, the most efficient structure was found to be tall and narrow, such as those found in mixed icterid flocks, not the flat structures parallel to the ground found for starlings.
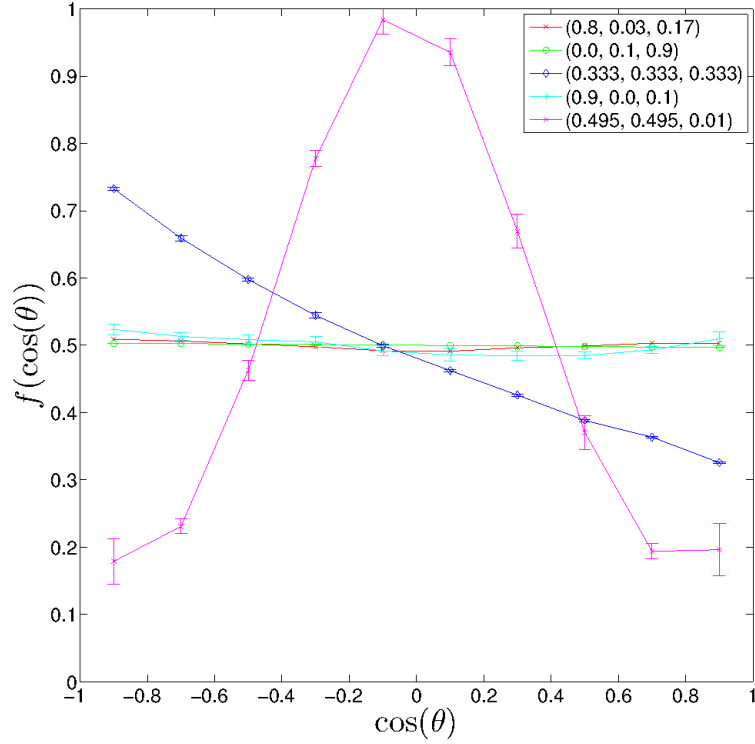
Figure 2.27: The empirical pdfs for $\cos(\theta)$ for 5 different sets of parameters $\vec{\phi}$ as shown on the inset for $N = 1000$. The nearest neighbour bearing measurements were made over $80,000$ timesteps with $20,000$ timestep equilibration. Error bars are for the standard errors. For $\vec{\phi} = (0.495, 0.495, 0.01)$, a uniformly random displacement was added to the positions due to the tendency to produce flat flocks, which breaks the 3D alpha shape algorithm. The displacement was $x, y, z \sim \text{Uniform}(-5\text{e}^{-6}, 5\text{e}^{-6})$, which are orders of magnitude smaller than the nearest neighbour distances, which are of order unity.

formly random and this is also unsurprising, as this behaviour type is noise dominated. See Fig. 2.27.

The nearest-neighbour distribution for the low noise, $\vec{\phi} = (0.495, 0.495, 0.01)$, which falls on the diagonal of the parameter space diagrams, is highly anisotropic, with a large peak at $\cos(\theta) = 0.0$ or $\theta = \pi/2$. This means it is very likely to find the nearest neighbour at the sides of a focal individual. Looking at the flocks formed, these tend to be very flat with the motion perpendicular to the plane containing the flock. Hence nearest neighbours are found at $\pi/2$ relative to the direction of motion of the individuals. It is surprising how consistently flat the flocks are for these parameters.

For $\vec{\phi} = (0.333, 0.333, 0.333)$, the nearest neighbours tend to be behind the individuals with the probability decreasing towards the front. This distribution differs to those previously described and demonstrates the richness of behaviours across the parameter space. It has been found that the empirical nearest neighbour angular distribution varies within $\pm \sim 20\%$ of uniform, with increased density at the sides (see Fig. 2.26).

It is interesting that differing structures arise in the angular distributions as this is not explicitly built into the model. The symmetry of the flock is broken in highly aligned flocks, such as $\vec{\phi} = (0.9, 0.0, 0.1)$ but this is not enough to produce the large deviations from randomness seen for $\vec{\phi} = (0.495, 0.495, 0.01)$ and $\vec{\phi} = (0.333, 0.333, 0.333)$. The projection term is clearly driving this anisotropy without any anisotropy in the individual viewing angles. The anisotropic nature of the natural visual apparatus has been suggested as the cause in natural flocks, but is clearly not a necessary condition for anisotropy.

2.7 Algorithms

2.7.1 Spherical Geometry

$\vec{\delta}_{p,i}$ is calculated as the centre of mass of the boundaries of the projection through the flock onto an individuals view. This boundary is composed of circular arcs from the projection of the other spherical individuals. The projection of a sphere onto the surface of another sphere is not generally a hemisphere with a great circle boundary, but a spherical cap with a shorter circular boundary. This boundary of the union of the projection of multiple spheres will be composed of arcs of these circles. These circles on a sphere define a spherical cap (the region of smallest volume bounded by the circle) for which it is the base. Hence a representation of a (general) circle in 3D is required, the
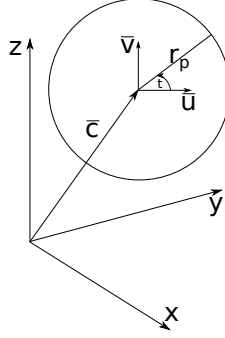
Figure 2.28: The circular bases of the spherical arcs are 3D circles with a point on that circle defined by the equation $\vec{x}(t) = \vec{c} + r_p\{\cos(t)\vec{u} + r_p\sin(t)\vec{v}\}$, where $\vec{c}$ is the circle's centre, r_p its radius; $\vec{u}$ and $\vec{v}$ are perpendicular basis vectors for the circle and $0 \leq t \leq 2\pi$ the angle parameter that defines a position on that circle.

representation used in this study is:

$$\vec{x}(t) = \vec{c} + r_p\{\cos(t)\vec{u} + r_p\sin(t)\vec{v}\} \qquad (2.39)$$

where $\vec{x}$ is a point is on the circle, $\vec{c}$ is the circle centre, $\vec{u}$ and $\vec{v}$ are unit vectors in the plane of the circle, r_p is the radius of the circle and t is the parameter $0 \leq t \leq 2\pi$. See Fig. 2.28. Intersections between circles are found using this representation by the formula in Szalay et al. [2005]. Each circle is supported on a plane with the following equations

$$\vec{n}_1 \cdot \vec{x} = c_1 \qquad (2.40)$$
$$\vec{n}_2 \cdot \vec{x} = c_2 \qquad (2.41)$$

where $\vec{n}$ are unit vectors perpendicular to the supporting plane and $\vec{x}$ are points on those planes. For the 2 circles to intersect their supporting planes must intersect along a line (or a point). We will define this line in terms of the axes composed from these normal vectors:

$$\vec{x} = u\vec{n}_1 + v\vec{n}_2 + w(\vec{n}_1 \times \vec{n}_2) \qquad (2.42)$$

($\vec{n}_1 \times \vec{n}_2$ is a vector parallel to the line of intersection of the supporting planes (see Fig. 2.29). Multiplying Eqn 2.42 separately by $\vec{n}_1$ and $\vec{n}_2$ leads to 2 scalar equations. Using the fact that $\vec{n}_1$ and $\vec{n}_2$ are normal vectors and orthogonal, then defining $\vec{n}_1 \cdot \vec{n}_2 =$
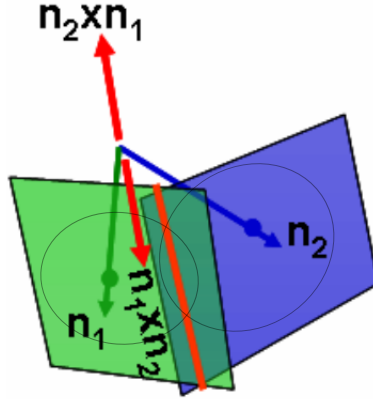
Figure 2.29: Finding the line of intersection for 2 circles in 3D space. For the 2 circles to intersect the planes (defined by normal vectors $\vec{n}_1$, $\vec{n}_1$) containing them must also intersect. They do so along a line which is in the direction of the cross product vector of the 2 normal vectors defining the supporting planes [Szalay et al., 2005].

$\cos(\theta) = \gamma$ gives us

$$u + v\gamma = c_1 \tag{2.43}$$

$$u\gamma + v = c_2 \tag{2.44}$$

The 2 planes cannot be parallel if there is to be an intersection hence $\gamma \neq \pm 1$ (which must be explicitly tested for). Solving for u and v we get

$$u = \frac{c_1 - c_2\gamma}{1 - \gamma^2} \tag{2.45}$$

$$v = \frac{c_2 - c_1\gamma}{1 - \gamma^2} \tag{2.46}$$

As out intersections also occur on the unit sphere, we have $\vec{x} \cdot \vec{x} = 1$. Using this; that $\vec{n}_1$ and $\vec{n}_2$ are unit vectors and that $|\vec{n}_1 \times \vec{n}_2| = 1 - \cos^2(\theta) = 1 - \gamma^2$ we get an equation for the squared position

$$\vec{x} \cdot \vec{x} = u^2 + v^2 + 2uv\gamma + w^2(1 - \gamma^2) = 1 \tag{2.47}$$

which we solve for w

$$w^2 = \frac{1 - (u^2 + v^2 + 2uv\gamma)}{1 - \gamma^2} = \left(1 - \frac{c_1^2 + c_2^2 - 2c_1c_2\gamma}{1 - \gamma^2}\right)\frac{1}{1 - \gamma^2} \tag{2.48}$$

For the equation to have valid roots the following 2 conditions must be met

$$1 - \gamma^2 \;>\; 0 \tag{2.49}$$

$$1 - \gamma^2 \;\geq\; c_1^2 + c_2^2 - 2c_1 c_2 \gamma \tag{2.50}$$

Arcs are defined on such a circle, called the supporting circle, by the parameter t, s.t. $t_{\text{start}} \leq t \leq t_{\text{end}}$ and $t_{\text{end}} \geq t_{\text{start}}$, with the exception of arcs that cross the $0, 2\pi$ boundary. With the exception of arcs that cross the $0, 2\pi$ ends follow starts around the circle with increasing t. The centre of mass of an arc is calculated in the $\vec{u}\vec{v}$-frame, as this is the centre of mass of a circle arc in 2D. The equation of the circle is then $u(t) = r_p \cos(t)$ and $v(t) = r_p \sin(t)$ and the differential arc length is $\sqrt{u'(t)^2 + v'(t)^2} = r_p$

$$\bar{u}L = \int_{t_{\text{start}}}^{t_{\text{end}}} r_p{}^2 \cos(t).dt = r_p{}^2 [\sin(t)]_{t_{\text{start}}}^{t_{\text{end}}} \tag{2.51}$$

$$\bar{v}L = \int_{t_{\text{start}}}^{t_{\text{end}}} r_p{}^2 \sin(t).dt = r_p{}^2 [-\cos(t)]_{t_{\text{start}}}^{t_{\text{end}}} \tag{2.52}$$

where L is the arc length $r_p(t_{\text{target}} - t_{\text{source}})$. Hence the contribution to the centre of mass in the model frame of a single arc is:

$$L\left[\vec{c} + \frac{\bar{u}\vec{u} + \bar{v}\vec{v}}{L}\right] \tag{2.53}$$

The overall centre of mass position for all the arcs on a sphere is the sum over the individual arcs divided by the sum of the arc lengths L. This will necessarily be inside the sphere and for a unit sphere will therefore be a vector having magnitude less than 1.

2.7.2 Projection Algorithm

The computational problem is to find the boundaries of arrangements of circles on the surface of a sphere. It has been said that when solving a computational problem that you can either use better algorithms or better numbers (e.g. exact or high precision arithmetic implementations). A Bentley-Ottman algorithm for high precision arithmetic that is of $O(N \log N)$ complexity to find the arrangement of circles on the surface of a sphere exists, but an implementation is not publicly available. When double precision arithmetic was used (to increase speed) in an implementation of this algorithm by the author, the algorithm seemed to be unstable to missed intersections. So, a more robust, but less efficient double precision algorithm was developed for this work.
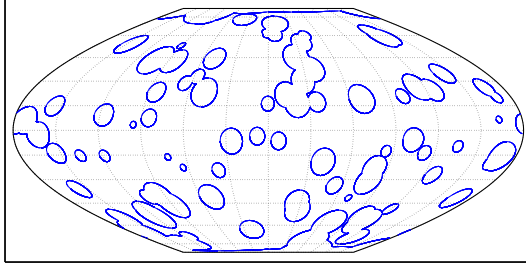
Figure 2.30: A McBryde-Thomas Flat-Polar Parabolic projection of the edge finding projection algorithm's output for 100 randomly placed circles. The maximum surface coverage is 1/2 the surface area, with 10 circle sizes that have uniformly distributed radii. All the intersections have been identified correctly. The actual surface coverage is 1/4.

The designed algorithm took the circles denoting the base of the spherical caps of the projection of the individual particles and then found the intersection of these circles. First, each pair of projected circles was checked to see if they were close enough to overlap and then their intersections were found. The spherical distance from the centre of a projected spherical cap to its circumference is

$$d = |\arccos \|\vec{c}\| |$$ (2.54)

Hence two caps may overlap if the distance to their radii is less than there circumference, i.e. $d_1 + d_2 \leq d_{12}$.

$$d_{12} = \left| \arccos \frac{\vec{c}_1 \cdot \vec{c}_2}{\|\vec{c}_1\| \|\vec{c}_2\|} \right|$$ (2.55)

From those intersection points the connecting arcs were defined according to Eqn. 2.39 and then each arc was checked to see if it was contained in any supporting circle sufficiently close to the supporting circle of the arc to overlap with it (again from d_{12}). Any arc found to be contained within another supporting circle was then eliminated from the arc list. To test for the possibility of an arc being contained within cap i the midpoint on the arc under test was projected onto the $\vec{u}_i \vec{v}_i$ basis of supporting circle i. If in this coordinate system the point was less than r_i from the centre of the supporting circle then the arc must be contained in that cap. The projections of a point $\vec{p}$ onto $\vec{u}_i$ and $\vec{v}_i$

71

are

$$\text{proj}(\vec{p}, \vec{u}_i) = (\vec{p} - \vec{c}_i) \cdot \vec{u}_i \tag{2.56}$$

$$\text{proj}(\vec{p}, \vec{v}_i) = (\vec{p} - \vec{c}_i) \cdot \vec{v}_i \tag{2.57}$$

The conditions for the inclusion of the arc in the spherical cap are

$$\text{proj}(\vec{p}, \vec{u}_i)^2 + \text{proj}(\vec{p}, \vec{u}_i) < r_i^2 \tag{2.58}$$

and

$$(\vec{p} - \vec{c}_i) \cdot \vec{c}_i > 0 \tag{2.59}$$

ensures that the arc is on a hemisphere shared with the spherical cap.

Visual inspections of the output of the algorithm indicate that it is working correctly and is more stable to missed intersections than the previously implemented method. Although inaccuracies could be tolerated for the intersection of small circles on the grounds that the visual system itself will have a cut-off below which it fails to function (i.e. resolution) and that as the input of the projection term to the model is an integral over arc length, the smaller arcs will influence the model output the least.

2.7.3   Calculating Opacity: Spherical Surface Integration

The projection algorithm is concerned with finding the boundaries of overlapping spherical caps which are spherical arcs. To avoid an expensive area-discretised calculation of the occluded surface area, an approximate green's theorem method was used to find the area from the already obtained boundary arcs. The accuracy of this estimate of the occluded surface area is clearly limited by the accuracy of the representation of the boundary and on how the discretisation over the boundary is performed.

For spherical caps not overlapping any others the surface area is easily found as $2\pi r h$ where $r = 1$ is the radius of the view sphere and h is the radius minus the distance to the centre of the cap's bounding circle, i.e. the cap height. Areas of overlapping regions are calculated by integrating over z-monotone arcs that the region's boundary has been divided into.

If necessary, arcs are split so that they are z-monotone. This results in a definition of 'left' and 'right' arcs. Drawing a meridian through each circle centre (and the view sphere's poles) results in two halves. The half with smaller ϕ is the left half. The area

integration is carried out by integrating the function

$$f(z) = \left\{ \begin{array}{ll} -\phi(z) & \text{if arc is left} \\ \phi(z) & \text{if arc is right} \end{array} \right\}$$
(2.60)

for each arc numerically. On each arc the numerical integration used is an adaptive 15-point Gauss-Konrod rule scheme [Galassi et al., 2009]. Thus the total area is calculated by subtracting the enclosed area for left arcs and adding the area to the total area sum for right arcs, with respect to a prime meridian at $\phi = 0$. This is explained visually in Fig. 2.31.

Care needs to be taken when the boundaries include the poles, as the ϕ integration will miss the spherical cap with z-values higher (lower) than the highest (lowest) value on the boundary when enclosing the North (South) pole. An ordered list of the intervals of overlap with the prime meridian are recorded as pairs of z-coordinates (upper and lower bounds). Hence if the South pole is included in a region the lowest lower bound is -1 and if the North pole is included the highest upper bound is $+1$. This list is also necessary as $2\pi(z_u - z_l)$ needs to be subtracted for each crossing of the prime meridian. This is due to the 'right 'part of the boundary being at smaller ϕ than the 'left' part. Hence the requirement of maintaining an interval list data structure implemented using the interval set class of the boost::icl interval arithmetic library [Dawes, 2003].

A similar method was implemented in a technical report by NASA [Chamberlain and Duquette, 2007]. Their method is for spherical polygons (composed of great circle segments) and integrates with respect to the South Pole, rather than a meridian. However the algorithm does not work if either pole is contained inside the polygon and therefore it is necessary to test for that eventuality and rotate the coordinate system appropriately (assuming such a rotation is possible). When working with a spherical approximation of the Earth for strategic simulations (the NASA case), this is not onerous as the poles are not usually in regions of interest. Their method could be adapted for general spherical arcs by using a numerical integration scheme for the area between the arc and the South Pole and has the advantage that it is unnecessary to maintain a z-interval data structure, but it is not as general, as it can't deal with regions that cannot be rotated to avoid covering both poles. Unless this eventuality is tested for and the region divided into two such that no piece contains both poles.

To evaluate the quality of the numerical spherical integration scheme implemented, a comparison with a simple pointwise integration scheme is made. Spherical caps were placed with minimum distances to their bases $r \leq 1$ and $\phi \sim \text{unif}(0, 2\pi)$ and
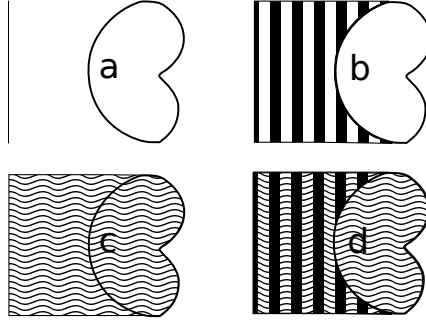
Figure 2.31: Finding the area of a shape **a** constructed of left and right arcs of general circles on the sphere. The area between the left arcs and the meridian, **b**, are subtracted; whereas the area between the meridian and the right arcs, **c**, are added to the overall area sum. This gives the total area of the shape, i.e. the wavy portion in **d**.

$\theta \sim \mathrm{unif}(0, \pi)$. This results in more spherical caps at the poles. Two situations were tested: the first where the caps are of uniform size and a second where the caps are uniformly distributed up to a maximum size n, where the expected area of the caps (if they did not overlap) is Ω_{max} a control parameter which sets the number of caps, N. The total area of the regions occluded by the randomly placed spherical caps was then evaluated using the pointwise integration method and the 3D approximate greens theorem approach outlined previously.

The first test involved the random placement of uniform spherical caps and the comparison with the point-wise scheme was made over a range of cap numbers N. A short cut in the opacity calculation used in the flock simulations is that non-overlapping caps are calculated using the simple formula for their area ($S = 2\pi h$), thus removing the numerical integration of isolated circles and improving the overall accuracy of the opacity calculation. However for the following tests, isolated circles were also integrated numerically, because this is a test of the accuracy of the Green's theorem based approach. The difference between the integrations is less than 1% over all numbers of caps N. This is a good performance over a large range of surface coverages, as shown in Fig. 2.32. indirectly, this is also a measure of the quality of the projection algorithm used, as errors in the arcs will translate into errors in the surface integration.

However using uniform caps means the arcs integrated over have uniform curvature and a more realistic test uses caps that have a distribution of radii. The second test used a uniformly distributed set of radii for the spherical caps and the algorithm also shows a higher level of accuracy (see Fig. 2.33).
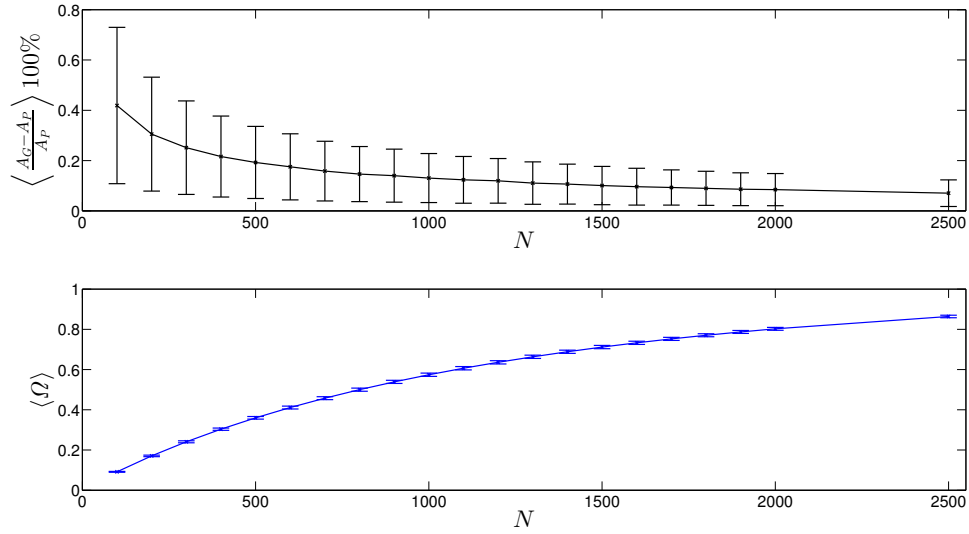
Figure 2.32:   As the number of uniform caps N increases, the percentage difference between the approximate green's theorem and the point-wise integration scheme falls. The variance reduces due to the increased number of caps sampling surface positions more effectively.

2.8 n-Nearest vs Delaunay Neighbours: A 2D Case Study

In Fig. 2.34 a) the advantages of the Delaunay neighbour construction in a 2D flock can be seen. It is that connectivity in alignment information is maintained even with some members significantly outside the main body of the flock. In Fig. 2.34 b) the Delaunay neighbours are illustrated for a flock using a nearest neighbour rule for alignment. The various sub-flocks would be connected in the passing of alignment information, if neighbours were defined by the Delaunay triangulation used instead of being less than the 7-th nearest neighbour as in b).

The choice of neighbour definition, does make a difference to the amount of alignment generated. The higher n in an n-nearest neighbours model, the more connected the flock will be in terms of alignment, i.e. the less likely it is that there will be groups moving away from the main flock that will eventually become too distant to share any neighbours with the main flock, hence becoming separate flocks. This is because the alignment interaction is an average over neighbours with proportion in the velocity update controlled by ϕ_a. It was previously shown that only small amounts of the
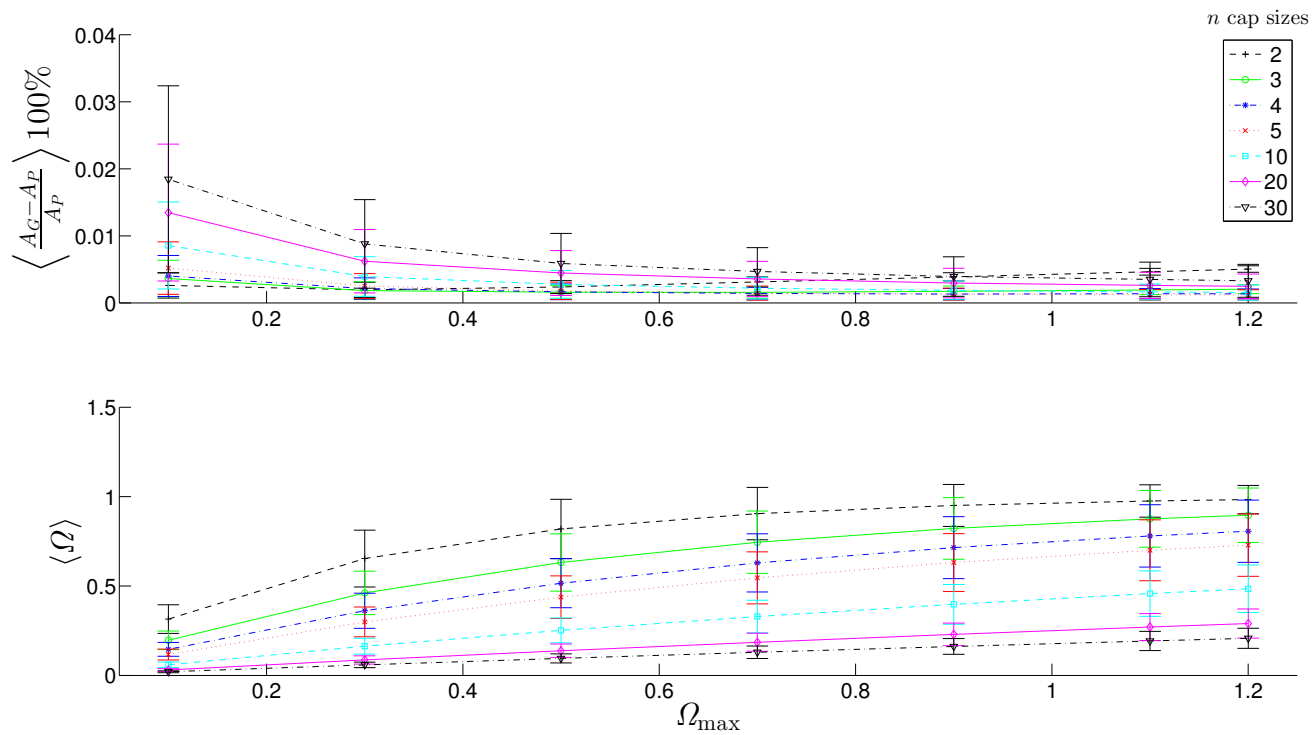
Figure 2.33: For the tested numbers of cap sizes, n, the difference in the numerical schemes decreases as the view coverage represented by Ω the opacity as a function of the total area of the caps assuming they did not overlap ($\Omega_{\max}$) increases and tends towards a value less than 0.01%.
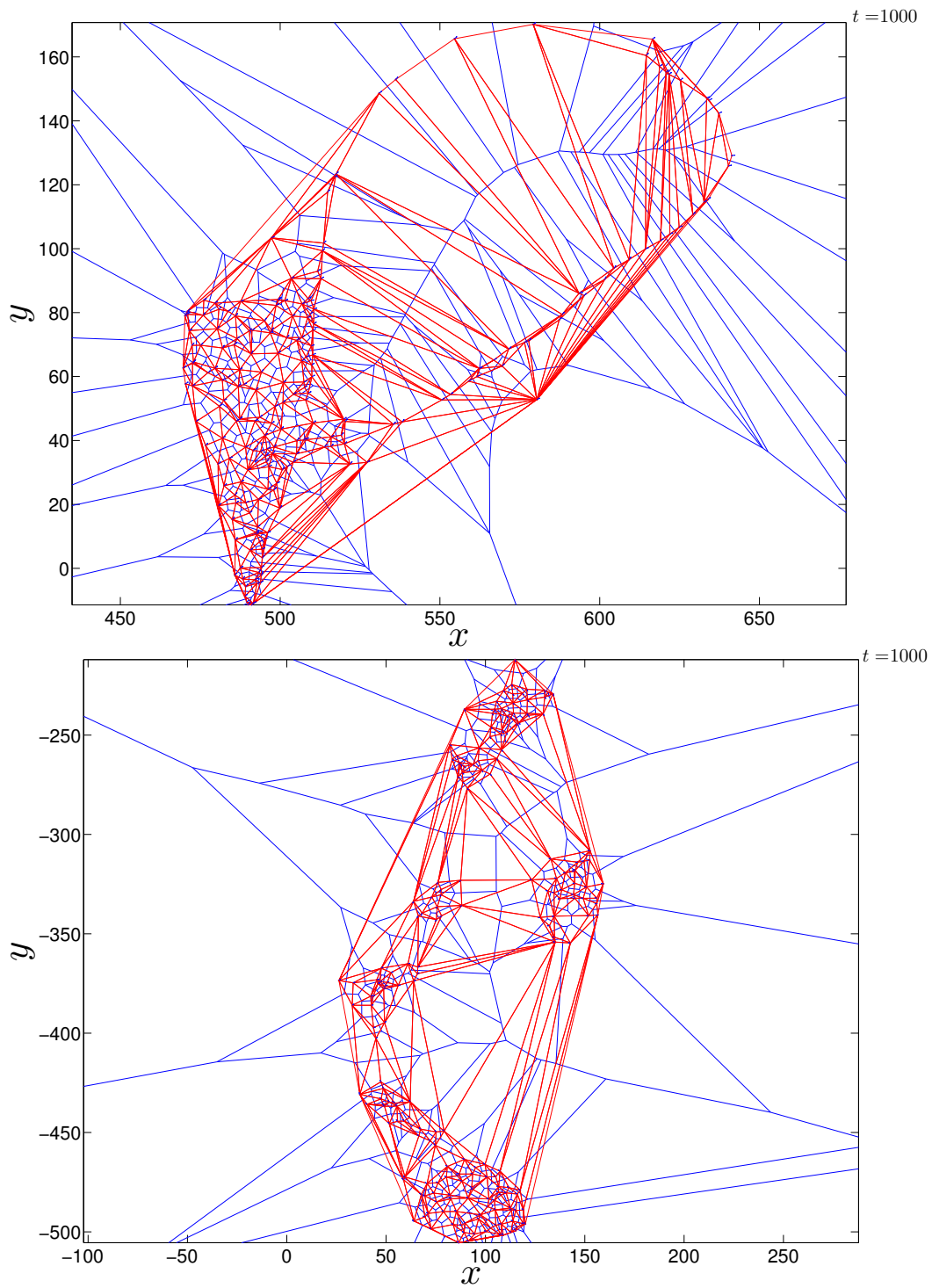
Figure 2.34: The Delaunay triangulation is shown in red and the Voronoi construction in blue for 2D $N = 200$ flocks with $\vec{\phi} = (0.8, 0.03, 0.17)$ with alignment from an average over a) Delaunay triangulation neighbours and b) the 7 nearest neghibours.

77

projection term $\vec{\delta}_{p,i}$ were required to prevent flock dissipation for the case of Delaunay neighbours. Even though this remains true, no matter what the neighbour definition is for the alignment term, the alignment order parameter Ψ depends strongly on the transfer of alignment information in the flock.

$$\Psi = \frac{1}{Nv_0} \left| \sum_{i=1}^{N} \vec{v}_i \right| \tag{2.61}$$

Where v_0 is the average absolute velocity of individuals in the system (in this model a constant, $v_0 = 1.0$). This is not really surprising, as for n-nearest neighbour models, it is possible to have locally aligned regions that communicate weakly with other neighbouring regions in the flock, based on the density of internal connections. Hence increasing the number of members in the flock for an n-nearest neighbour model, where $n \leq N$ results in a lower order parameter as the growth in the size of the flock outstrips that of the order parameter correlation length (see fig. 2.35).

2.9 Discussion

The projection rule described here is similar to a rule inspired by the selfish herd theory and has been simulated in 1D and 2D [Viscido et al., 2002]. This rule is the 'Local Crowded Horizon' (LCH) and it also uses the density of the whole flock to determine movement. At each timestep the focal individual, i, moves towards the part of the horizon that is most densely populated, after adjusting for perceptive ability. The influence of j on i was considered to be proportional to the size of j's projection on the horizon and therefore decays with distance. The functional form of this perception was $f(r_{ij}) = \frac{1}{1+kx_{ij}}$, where r_{ij} is the distance between i and j. This form produced the desired compact flocks while reducing the average size of the domain of danger. Using a different perception function they were also able to prevent flock dispersion without having a higher central density (another aim of the model), similar to the results here. Herds of non-flying animals often display a high central density as they can get very close together without the inherent danger for flying animals (that they may collide and cease to be able to fly). The LCH simulations also contained no alignment or random noise terms, hence the reasonable comparison is with the $\vec{\phi} = (0.0, 1.0, 0.0)$ behaviour of the model here.

The parameter value planes investigated in §2.4.3 show regions of high alignment and opacity controlled by the projection term, it was later shown in §2.6 that for a set
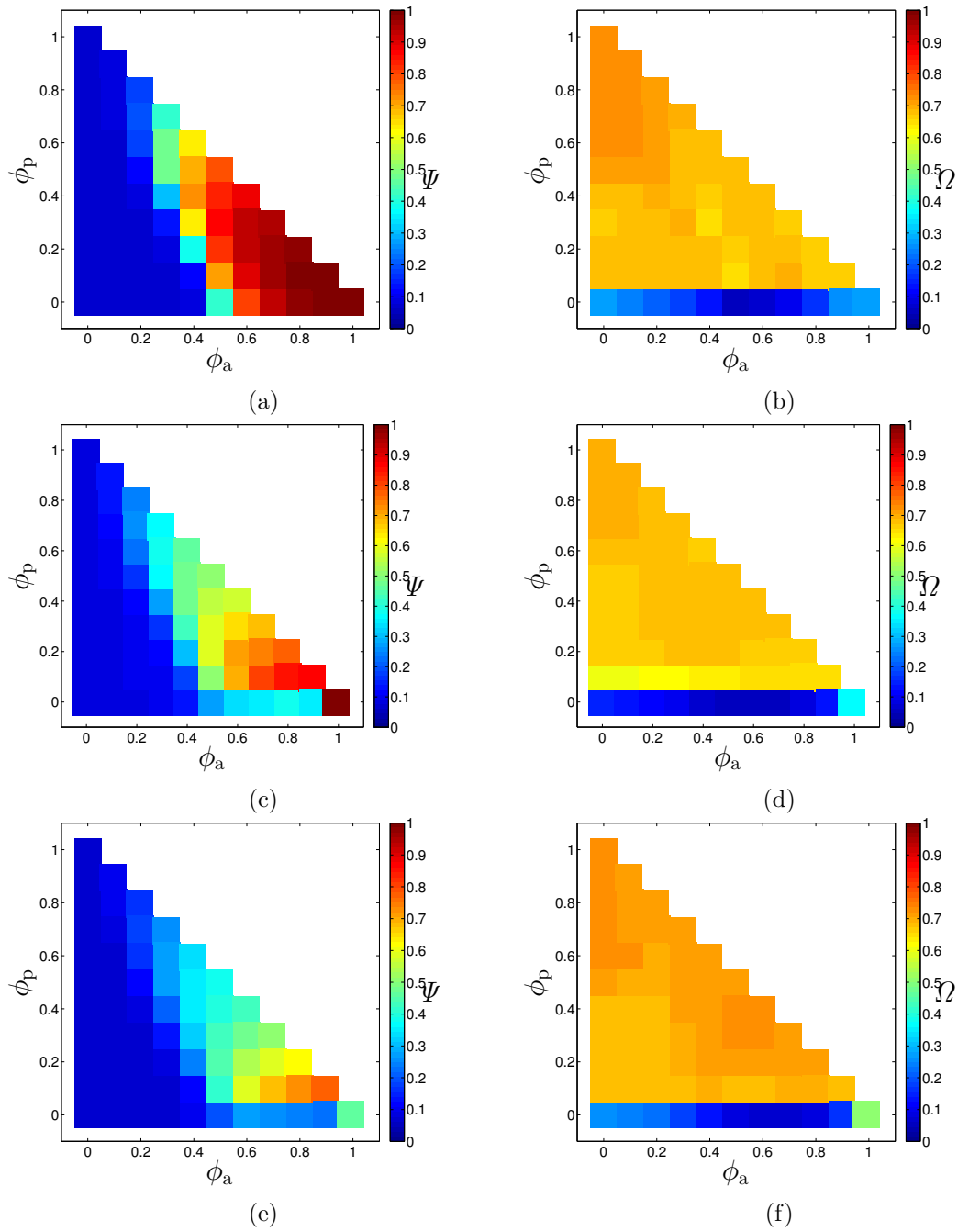
Figure 2.35: The variation of Ω and Ψ with control parameter values for an $N = 200$ flock using Delaunay neighbours a) and b). The variation with control parameters for $N = 100$ c) and d) and $N = 200$ flocks e) and f) with 7 nearest neighbours used for alignment ($n = 7$). Ω is similar for the 3 flock types but Ψ is less for $N = 200$ than $N = 100$, for the nearest neighbour alignment due to the lower transfer of alignment information across the flock. Both nearest neighbour flock types achieve less alignment than the Delaunay neighbours due to the increased connectivity in Delaunay flocks.

of chosen values in this region $\vec{\phi} = (0.8, 0.03, 0.17)$ that $r_{\max}$ scales with flock size in a way consistent with the empirically observed $r_{\max}$. The simulated $r_{\max}$ also scales as predicted by the simple mean field argument advanced in Pearce et al. [2014]. It is suggestive that the simple projection rule can reproduce the observed scaling behaviour in $r_{\max}$ and a plausible scaling in the opacity, Ω, that tends to a value that is less than 1 and hence is 'marginally opaque'.

An emergent anisotropy in the flock dimensions and nearest neighbour angular distributions, reflective of the empirical studies were investigated in §2.6.3 and §2.6.4. The anisotropy in the flock dimensions could only be examined in the 3D model and is a feature of the 3D model that is unexpected as there are no preferred directions for $\vec{\delta}_p$ *a priori*.

2.10   Future Work

- Perhaps the most obvious extension is to create a computationally less demanding model, perhaps by discretising the view rather than the arcs of the projections onto the view (the current method was chosen to keep the simulation as true to the theoretical model as possible). This would allow for much larger flocks and for calculating properties for more parameter values, in addition to investigating non-spherical particles and inertia.

- A rear blind angle caused by the location of the eyes in the skull has been found to affect the properties of some models, but in the 2D version of this model it was not found to lead to qualitative differences. It is still to be verified that a blind angle has little effect in 3D.

- As mentioned in §2.6.3 a possible, and indeed likely, driver of the anisotropy in flock dimensions is gravity and it has been empirically observed that flocks are thin and move parallel to the ground. A version of the model that modelled gravity, perhaps implemented as a contribution to the velocity $\phi_g \vec{v}_g$ that pushes individuals back to a preferred plane may produce the observed flock morphologies. This is of course an empirical rather than *a priori* addition to the model and perhaps may not differ much from the 2D model previously implemented in Pearce et al. [2014].

- A more detailed model involving basic flight characteristics, such as minimum turning angles and inertia would allow for further direct comparisons with the STARFLAG data and investigation of the turning characteristics of the flock. For

example, rock doves are believed to turn in equal radius paths and this has been shown to be true for starlings [Ballerini et al., 2008b].

- It has been shown that having individuals not obeying the same rules within a flock can control the flock behaviour, e.g. turning the flock. This could be tested by adding agents with different movement rules, e.g. a directional bias. Another question is the stability of the density scaling to differences in the individual rules, e.g. if the coefficients are drawn from a normal distribution around particular values. This is a different way of introducing error to that used in the model here.

- It would be interesting to look at the local density across the flock, as natural flocks have greater density at the edges than in the centre (which runs contrary to what is expected from selfish herd theory). This could be done by sequentially adding flock members from the centroid of the flock outwards and at each step calculating the volume of the associated α-shape. If the volume increases then the edges have greater density than the interior.

- Density measurements of starling flocks were made previously in this group from 2D photographs. These represent a external measurements of the opacity from a projection of the flock taken by an observer usually at many flock lengths from the flock. A code was developed to make a similar measurement, using an external observer (again with a spherical view), where the convex hull of the flock was projected onto the observers view.

Chapter 3

2D 2-Step Models Inspired by Optical Flow

It has been suggested by Gibson that visual perception should not be considered to be a series of still photographs to be processed by the brain before moving on to the next one, but instead it is the movement between frames (or flow) that is important [Gibson, 1986]. This idea is based on how considerably more information can be extracted from the visual field by considering the time evolution of the retinal response – such as whether an object is approaching/receding relative to the observer, by enlargement/reduction in their view. Further discussion of these ideas is given in section 1.3.4. This chapter investigates possibilities for a novel cohesion term, using the difference in views at two time steps.

3.1 Model Description

This model replaces the projection term of the model given in chapter 2, with a new term, designed to approximate optical flow $\vec{v}_{\text{flow}}$. This term, like the former projection term, is very simple and aims to be a minimal 'difference between two frames model' that has cohesion. The view of an individual is taken to be a unit circle, onto which are

projected the other flock members as dark regions as before. Four different models can be conceived along the lines of the projection model, but using the differences between two frames.

- Model D: Only regions that have become dark in the latest frame contribute. Take vectors to the edges of these regions from the individual and average them to give the new input.

- Model L: Only regions that have become light in the latest frame contribute. Take vectors to the edges of these regions from the individual and average to give the new input.

- Model DL: If a region was dark and has become light, take vectors from the edges of these regions to the individual and vice versa for light regions that have become dark. Hence move away from dark and towards light regions.

- Model LD: If a region was light and has become dark, take vectors from the edges of these regions to the individual and vice versa for dark regions that have become light. Hence move away from light and towards dark regions.

Model D encourages individuals to fly towards regions that have become dark, whereas model L says to fly towards regions that have become light. Model DL says to move away from newly dark regions towards newly light regions, whereas model LD says the opposite. These models clearly have a dependence on the individual velocities v, as these control the rate at which the views change. Models D and L were expected to act as cohesive terms as those outside the flock will only see changes to their view in the direction of the flock, whereas those inside the flock who are moving in roughly the same direction as the flock will have an approximately isotropically changing view and the contribution of $\vec{v}_{\text{flow}}$ to the overall velocity will be small.

3.1.1 The 2 Member 'Flock'

It is interesting to consider some particular movement cases for a pair of individuals. What do the model $\vec{v}_{\text{flow}}$ rules above say to do when the other individual approaches/recedes or goes past? These archetypal situations considered are illustrated in Fig. 3.1.

If the individuals move along the line joining them, model L says to go towards receding individuals, but not to avoid incoming ones. Model D says to go towards approaching individuals but not to follow receding individuals. Model L tries to avoid
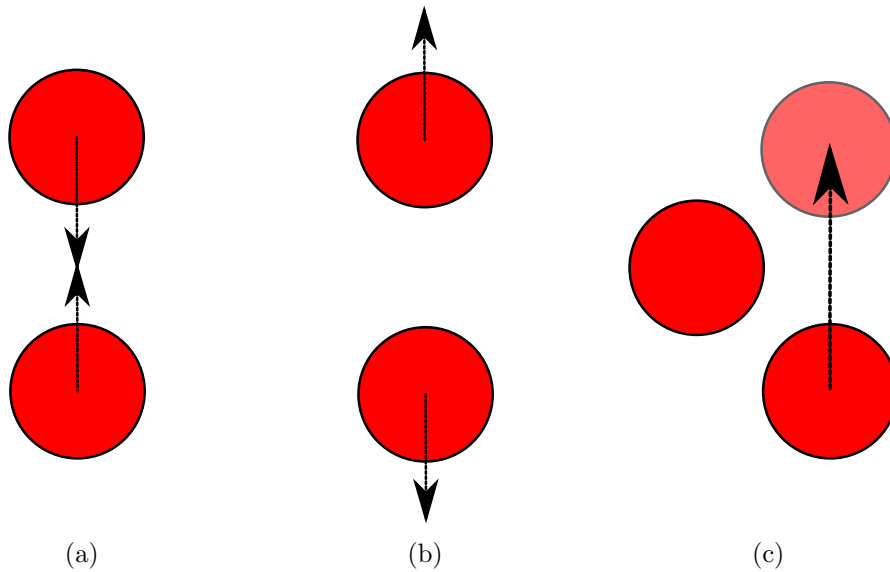
Figure 3.1: The three archetypal movements considered here are a) individuals moving towards each other, b) individuals moving away from each other and c) a particle moving past another.

separation, whereas model D encourages collisions! Neither is a satisfactory single rule in the 2 individual case when they are approaching or receding. Model LD is worse than either L or D as it says to move towards approaching individuals and away from receding ones. The only rule which might not result in collapse or dissipation in this setting is DL, as it encourages movement away from an approaching, but towards a receding, individual and will hence have the effect of maintaining the starting distance (see Fig. 3.2). That flock members would be approaching or receding from each other along a connecting line is unlikely. It is more likely that movement will be at an oblique angle with a similar result.

Another simple situation to consider, is when the two individuals move past each other, without change in the angular size of their respective images, i.e if we are in the reference frame of one individual, then the other follows a circular path of fixed radius as it passes the first. This means that the start and end-points (and every other point on the path) are equidistant from the focal individual (the one currently under consideration). For a rule designed to enhance cohesion, this is a not a relevant situation (as the distance between individuals never changes), but for an alignment contribution the direction indicated should be near that of the other individual's direction of travel. Rule L says to head in an oblique direction away from the trajectory of the other individual, whereas
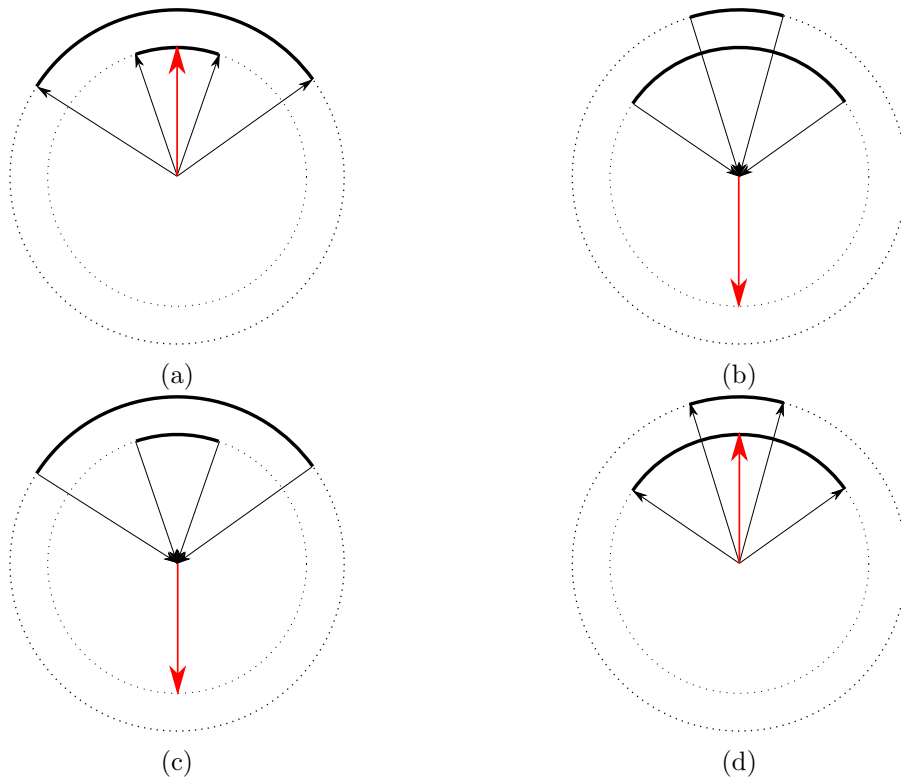
(a)

(b)

(c)

(d)

Figure 3.2: The inner circles represent an individual's view at the previous timestep and the outer circles the view at the current timestep. The red arrow gives an indication of the direction specified by the optical flow term, but not the magnitude. Model LD has exactly the opposite behaviour to what would be desired for a cohesive contribution to the velocity update equation when a single individual approaches a), or recedes b). Model DL on the other hand has the expected behaviour for a cohesive contribution, c) and d).
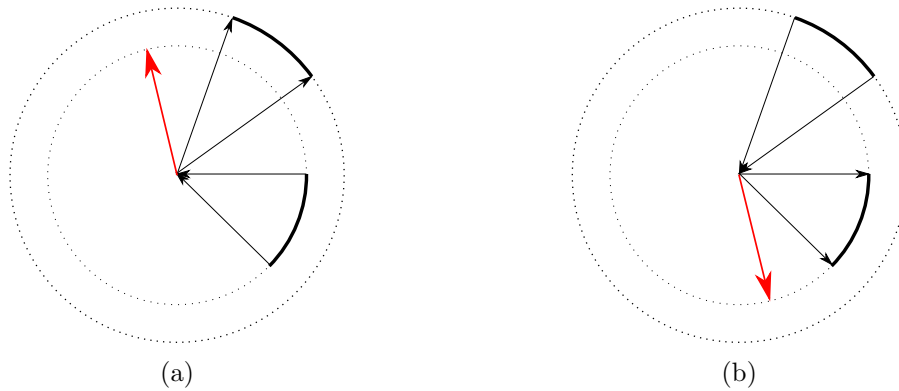
Figure 3.3: The inner circles represent an individual's view at the previous timestep and the outer circles the view at the current timestep. The red arrow gives an indication of the direction specified by the optical flow term, but not the magnitude. a) Model LD results in motion in the approximate direction that the projected individual is moving. b) Model DL results in motion in the opposite direction.

rule D says to move in the opposite direction to rule L (i.e. in an oblique direction towards the other trajectory). Rule DL results in movement in the opposite direction to the trajectory, whereas rule LD results in movement in the same direction. However outside of the equidistant path constraint, the interactions will clearly be more complicated.

Rules L and D cannot function as both alignment and cohesion contributions in both the approaching and receding cases, but rule D introduces approximate alignment, with a passing individual (whereas rule L will not). Rule DL is an acceptable cohesion rule, but not alignment rule and vice versa for rule LD. It does not appear that a single rule is sufficient to provide both *alignment* and *distance* controls in the $N = 2$ setting. However, few would consider two birds to be a flock, so that success or failure of a rule in these cases does not mean that we can immediately make assertions about its use as a cohesive rule in large flocks.

When a bird is outside a flock, rule D, rather intuitively, tells the bird to fly towards the flock as did the projection term from chapter 2 and this should be largely independent of the speed of the flock relative to the bird. Rule L will behave similarly if the movement of the flock is small relative to the focal individual, such that the newly light regions of view are still inside the new position of the flock. If the flock velocity is very high, the flock could move more than a flock length in a timestep and the newly light regions would be behind the flock (relative to the c.o.m. trajectory). This is not a distance that can be reasonably travelled that quickly in a natural flock, when compared to the cognitive update rates (assumed to be those of the visual system, which are in the

microsecond range). For rules LD and DL the size of the changing light and dark regions and the number of them should determine whether there is a net movement towards the flock or not. The easiest way to determine whether these mixed rules (DL and LD) will produce alignment and or cohesion (without collapse to unrealistic densities) is through simulation.

3.1.2 Model

As stated previously, the model is a Vicsek-like model similar to that in chapter 2. The new velocity update equation for individual i at time $t + 1$ is

$$\vec{v}_{i,t+1} = \phi_a \frac{\langle \vec{v}_t \rangle_{n_i}}{\|\langle \vec{v}_t \rangle_{n_i}\|} + \phi_{\text{flow}} \frac{\vec{v}_{\text{flow}}}{\|\vec{v}_{\text{flow}}\|} + \phi_e \vec{\eta}_i \quad (3.1)$$

Where the new term $\vec{v}_{\text{flow}}$ is the input from one of the new rules. The position update is therefore

$$\vec{x}_{t+1} = \vec{x}_t + v_0 \Delta t \frac{\vec{v}_{t+1}}{|\vec{v}_{t+1}|} \quad (3.2)$$

with Δt the length of the discrete time step, taken to be 1.

The 2D models were implemented in C++ using the Boost Interval Arithmetic Library to calculate the flow terms [Dawes, 2003]. The views at the current and previous timestep are represented as the interval sets of the filled portions of view in the range $[0, 2\pi)$ denoted S_{c} and S_{p}. From this, the unfilled portion of the views can be found from the absolute complements to these sets $U \setminus S_{\text{c}}$ or $U \setminus S_{\text{p}}$, where $U = [0, 2\pi)$ is the universe.[1]

The interval set that has become light in the current view and was dark in the previous view is

$$S_{\text{DL}} = S_{\text{p}} \setminus S_{\text{c}} \quad (3.3)$$

and the interval set that has become dark in the current view that was light in the previous view

$$S_{\text{LD}} = S_{\text{c}} \setminus S_{\text{p}} \quad (3.4)$$

Care needs to be taken at the boundaries, as the Boost Interval Arithmetic Library does not natively support periodic boundary conditions. If a region of light or dark overlapped the angle 0 an additional two boundaries, representing the boundaries of the internal linear interval representation, have been added to the sum). These boundaries were located at 0 and 2π These need to be accounted for, by subtracting the vector to

---

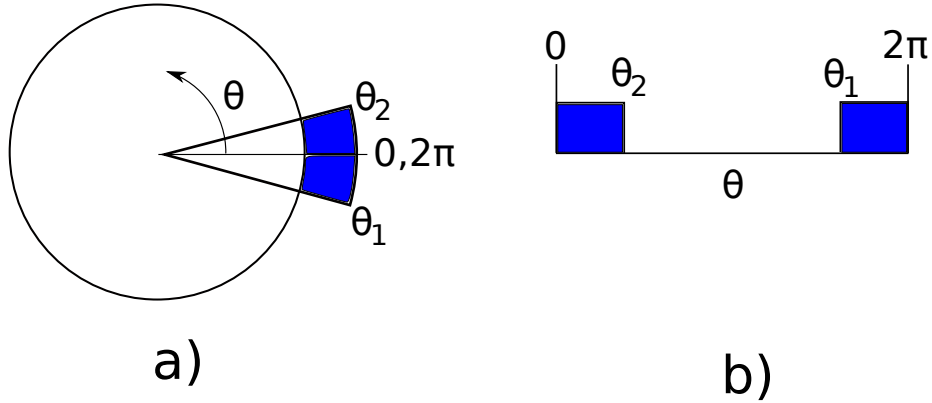[1]The complement, $A \setminus B = x \in A | x \notin B$

Figure 3.4: a) The projections of flock members onto an individual's circular view is recorded as the boundary angles of the projections. b) The representation used in the Boost interval arithmetic library is a linear interval. This introduces 2 false boundaries at the bounds of the interval which must be subtratcted from the $\vec{v}_{\text{flow}}$ calculations.

$(1, 0)$ twice from the calculated direction (see Fig. 3.4).

Let $\{\theta_{S,j}\}$ be the set of n_S end points of the intervals in set S. Then the flow terms are calculated as in table 3.1.

3.1.3 Initial Conditions

Unless otherwise specified, the individuals were initialised on a circular disc with radius $R = 80$ (dimensionless) units, uniformly distributed angular position and a radial probability distribution weighted to produce an approximately constant radial density.

$$r\mathrm{d}r\mathrm{d}\theta \;=\; \frac{1}{2}\mathrm{d}(r^2)\mathrm{d}\theta \tag{3.5}$$

$$\implies r^2 \;\sim\; \mathrm{unif}[0, R] \tag{3.6}$$

$$\implies r \;=\; \sqrt{u} \tag{3.7}$$

$u \sim \mathrm{unif}[0, R]$ and the angular distribution $\theta \sim \mathrm{unif}[0, 2\pi]$

3.2 Results

Again we are interested in the effect of changing the ratios of $\phi_a{:}\phi_{\text{flow}}{:}\phi_e$. Because of the normalization of the velocity term their absolute values are not important. Hence we can constrain the ϕs such that $\phi_a + \phi_{\text{flow}} + \phi_e = 1$ To identify the individual models the parameter ϕ_{flow} is replaced with one of ϕ_{D}, ϕ_{L}, ϕ_{DL} or ϕ_{LD} to indicate which model

Table 3.1: Construction of the different 2-step velocity $\vec{v}_{\text{flow}}$ contributions. The contributions to $\vec{\text{flow}}$ for the different models. For model D the vectors to the boundaries of regions that have become dark in the current view are summed to produce an input direction, similarly for light region boundaries in model L. Models DL and LD involving adding (vectorially) directions to one type of new boundary (L/D) and subtracting the other type (D/L). Hence movement is towards one type of boundary and away from the others. $\vec{v}_{\text{flow}}$ is then normalized $\vec{v}_{\text{flow}} = \vec{v}_{\text{flow}}/\|\vec{v}_{\text{flow}}\|$

Model	$\vec{v}_{\text{flow}}$
D	$\sum_j \begin{pmatrix} \cos(\theta_{S_{\text{LD}},j}) \\ \sin(\theta_{S_{\text{LD}},j}) \end{pmatrix}$
L	$\sum_j \begin{pmatrix} \cos(\theta_{S_{\text{DL}},j}) \\ \sin(\theta_{S_{\text{DL}},j}) \end{pmatrix}$
DL	$\sum_j \begin{pmatrix} \cos(\theta_{S_{\text{DL}},j}) \\ \sin(\theta_{S_{\text{DL}},j}) \end{pmatrix} - \begin{pmatrix} \cos(\theta_{S_{\text{LD}},j}) \\ \sin(\theta_{S_{\text{LD}},j}) \end{pmatrix}$
LD	$\sum_j \begin{pmatrix} \cos(\theta_{S_{\text{LD}},j}) \\ \sin(\theta_{S_{\text{LD}},j}) \end{pmatrix} - \begin{pmatrix} \cos(\theta_{S_{\text{DL}},j}) \\ \sin(\theta_{S_{\text{DL}},j}) \end{pmatrix}$

for the flow term was used.

3.2.1 Parameter Space Diagrams

The parameter space diagrams for models D and L are both very similar to those for the projection model and the opacity of the flock is relatively constant across the parameter plane with values of 0.6–0.7, i.e. the marginally opaque regime, with $r_{\max}$ also controlled. There is still a region of highly aligned and compact marginally opaque flocks as can be seen in fig. 3.5.

Disappointingly, models DL and LD do not have marginal opacity across most of the parameter plane. Model DL only has it when there is 99% alignment and 1% noise, this simply being a translating flock of density which is very slowly increasing. In addition to marginal opacity for 99% alignment and 1% noise model LD also has alignment for $(0.0, 0.99, 0.01)$, which is more interesting. The structure of the alignment parameter planes are very similar to those of the other 2 models, due to the identical implementation of the alignment rule.
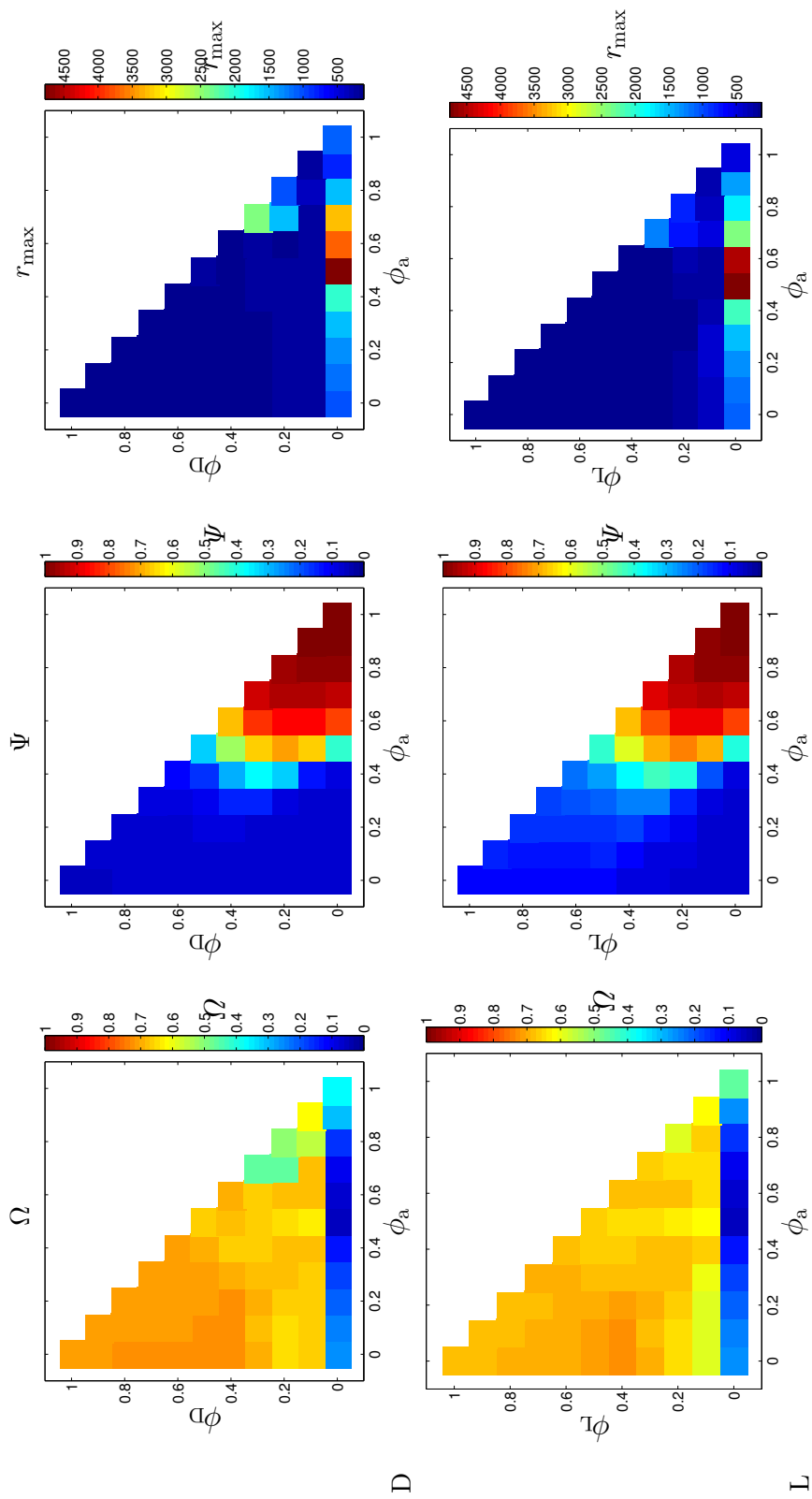
Figure 3.5: Parameter planes for measured quantities in models D and L. The quantities are the average opacity Ω, alignment Ψ and linear flock size $r_{\max}$, of the flock.
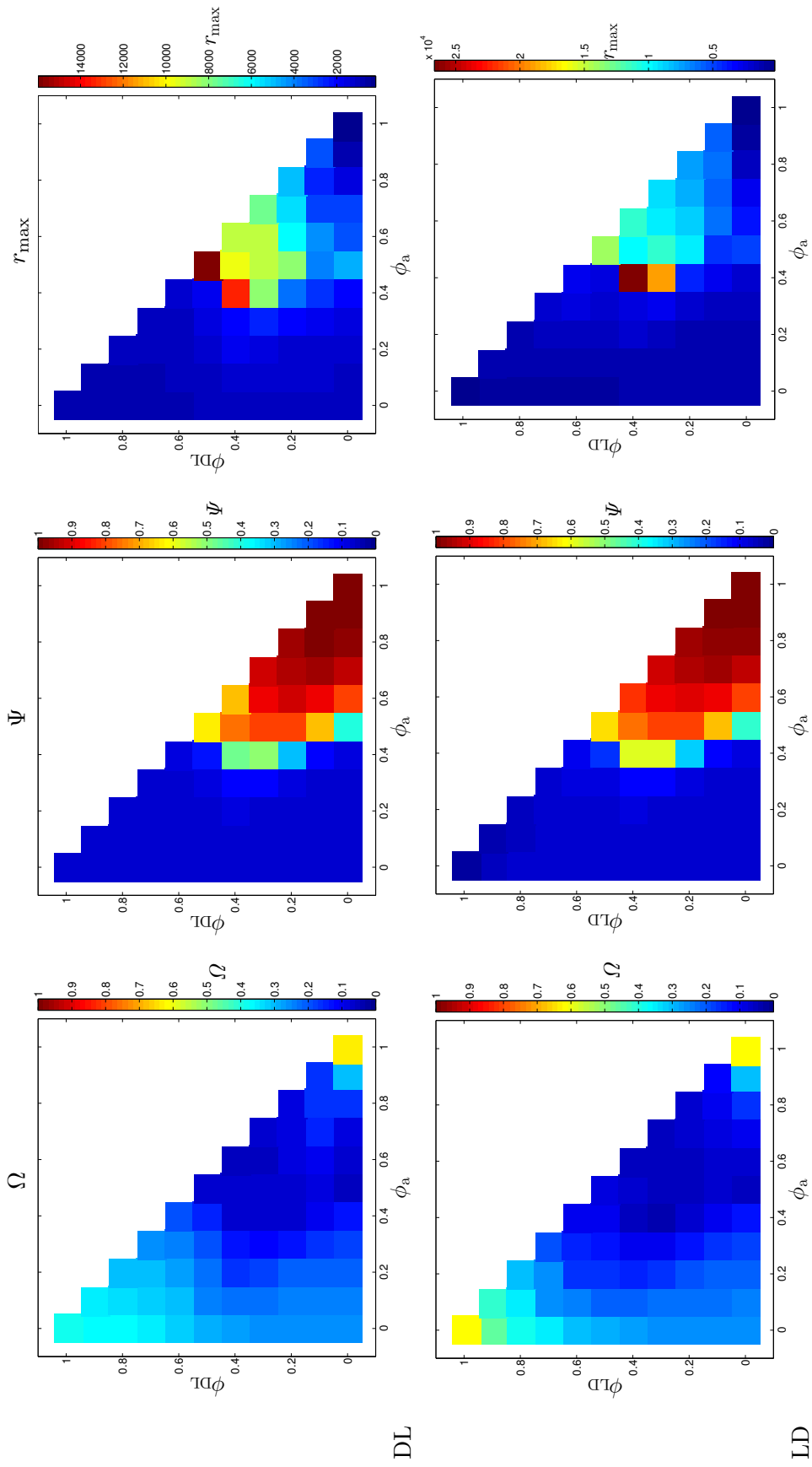
Figure 3.6: Parameter planes for measured quantities in models DL and LD. The quantities are the average opacity Ω, alignment Ψ and linear flock size r_{max}, of the flock. The initial condition for models DL and LD had individual directions with respect to the global coordinate system $[-\pi/4, pi/4]$ and were therefore highly aligned. This was due to the tendency of the models to generate rotating flocks, with different properties to the linearly translating ones.

3.2.2 Model Outputs

We will again define a model parameter vector $\phi = (\phi_a, \phi_{\text{flow}}, \phi_e)$.

Trajectories

Models D and L display similar behaviour for the examined trajectories. For $\vec{\phi} = (0.0, 0.99, 0.01)$ with no alignment contribution from ϕ_a, both models seem to favour a 3-armed flock shape that does not translate far from the initial centre of mass. This 3-armed stable configuration seems to be interrupted by increasing the proportion of alignment, resulting in increasingly more flock translation.

The models DL and LD form more convex non-translating aggregations, with model LD forming small clusters within the wider flock. Both models change quickly with increasing alignment term to wider and more linear flocks.

Models D and L only show significant translation of the centre of mass for high proportions of the alignment term as can be seen in Fig. 3.9. The displacement of the centre of mass is smaller for models DL and LD than for models D and L when $\vec{\phi} = (0.0, 0.99, 0.01)$. For $\vec{\phi} = (0.4, 0.4, 0.2)$ and (0.8, 0.1, 0.1) models DL and LD have much more linear centre of mass trajectories than the other two models. Reinforcing that these rules encourage alignment and might make a suitable visual alignment rule, although they fail as cohesion rules.
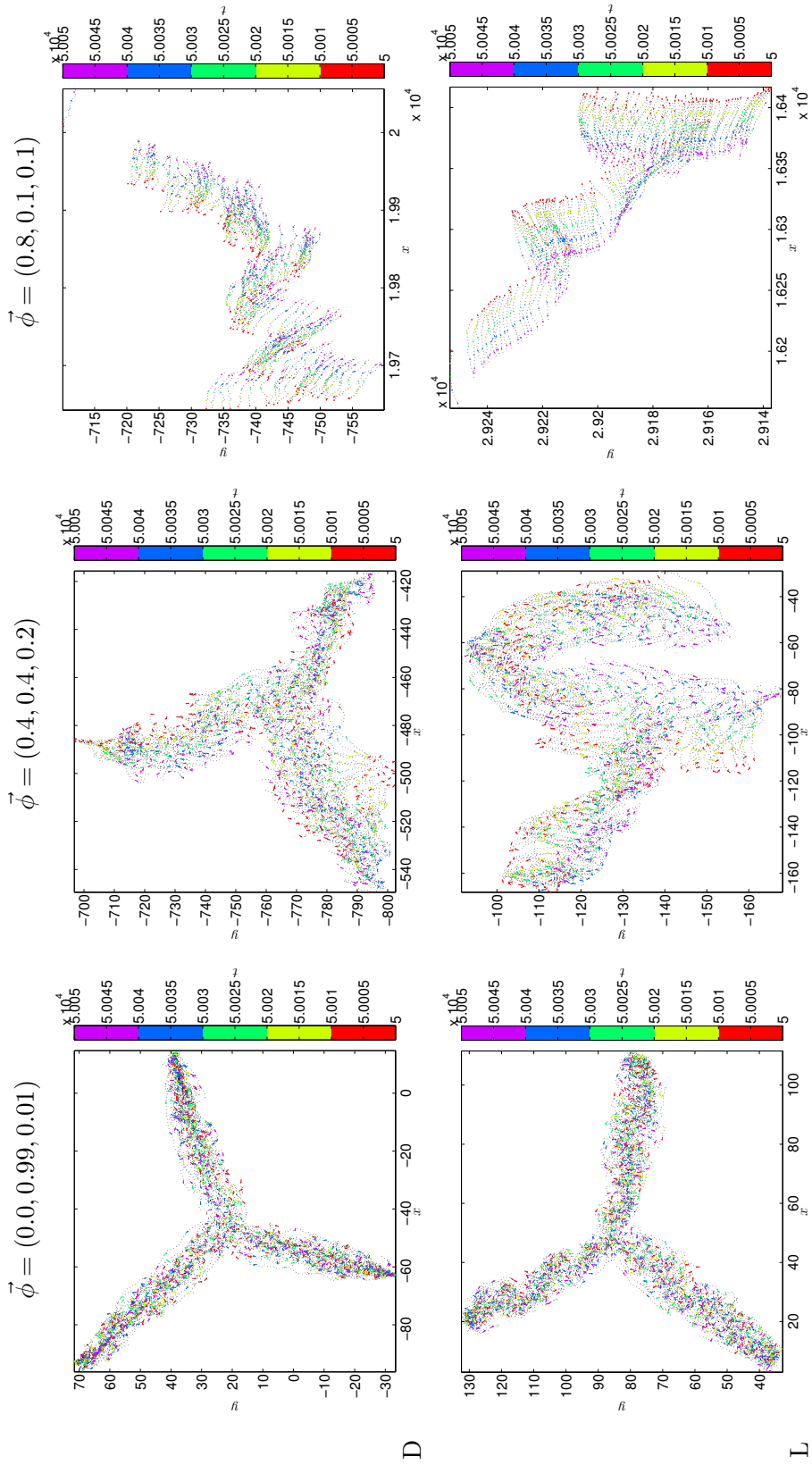
Figure 3.7: Snapshots with the number of timesteps between them $\tau = 10$, for $N = 200$, starting at $t = 50000$ and hence the range represents 50 timesteps.
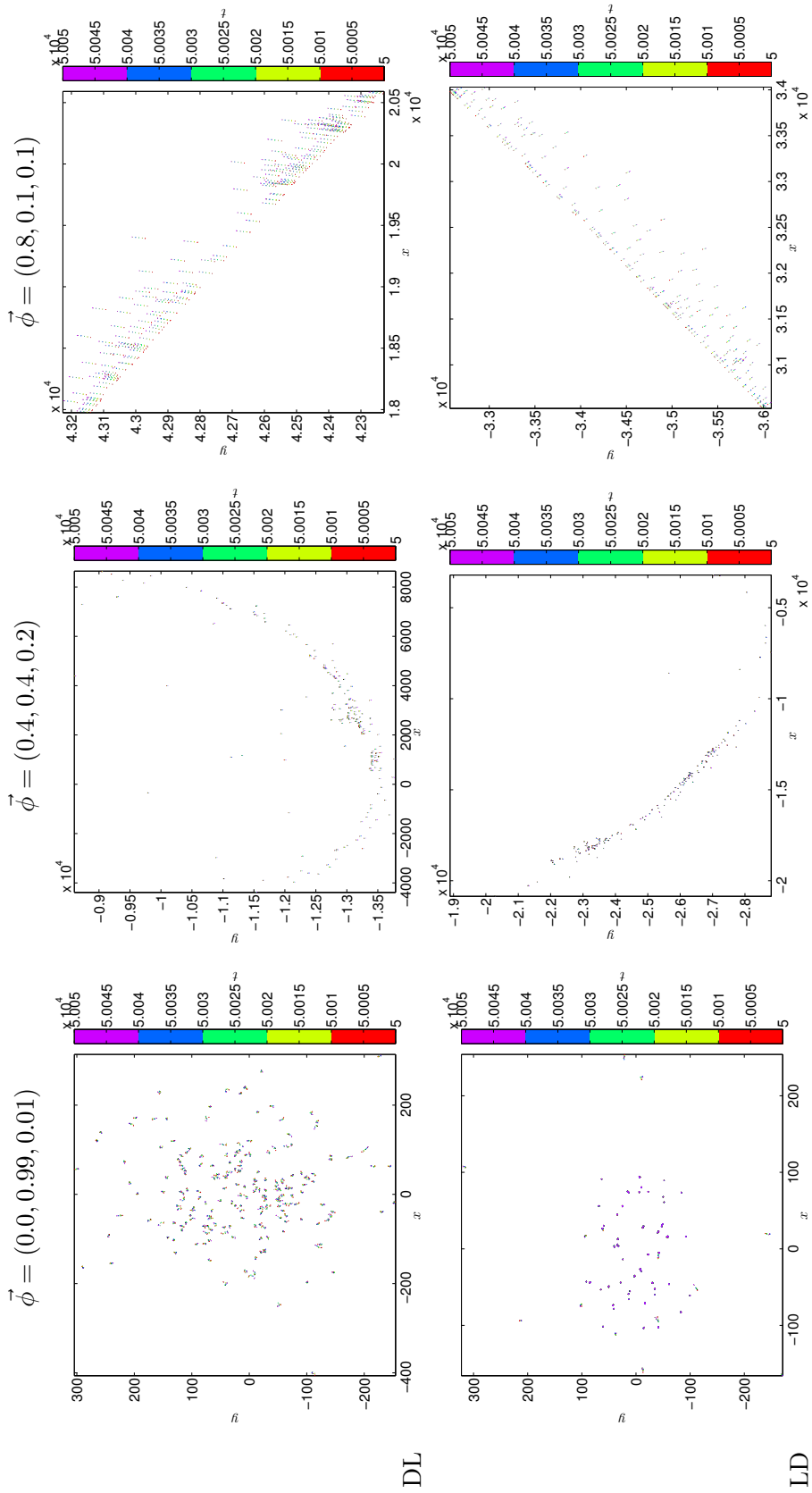
Figure 3.8: Snapshots with the number of timesteps between them $\tau = 10$, for $N = 200$, starting at $t = 50000$ and hence the range represents 50 timesteps.

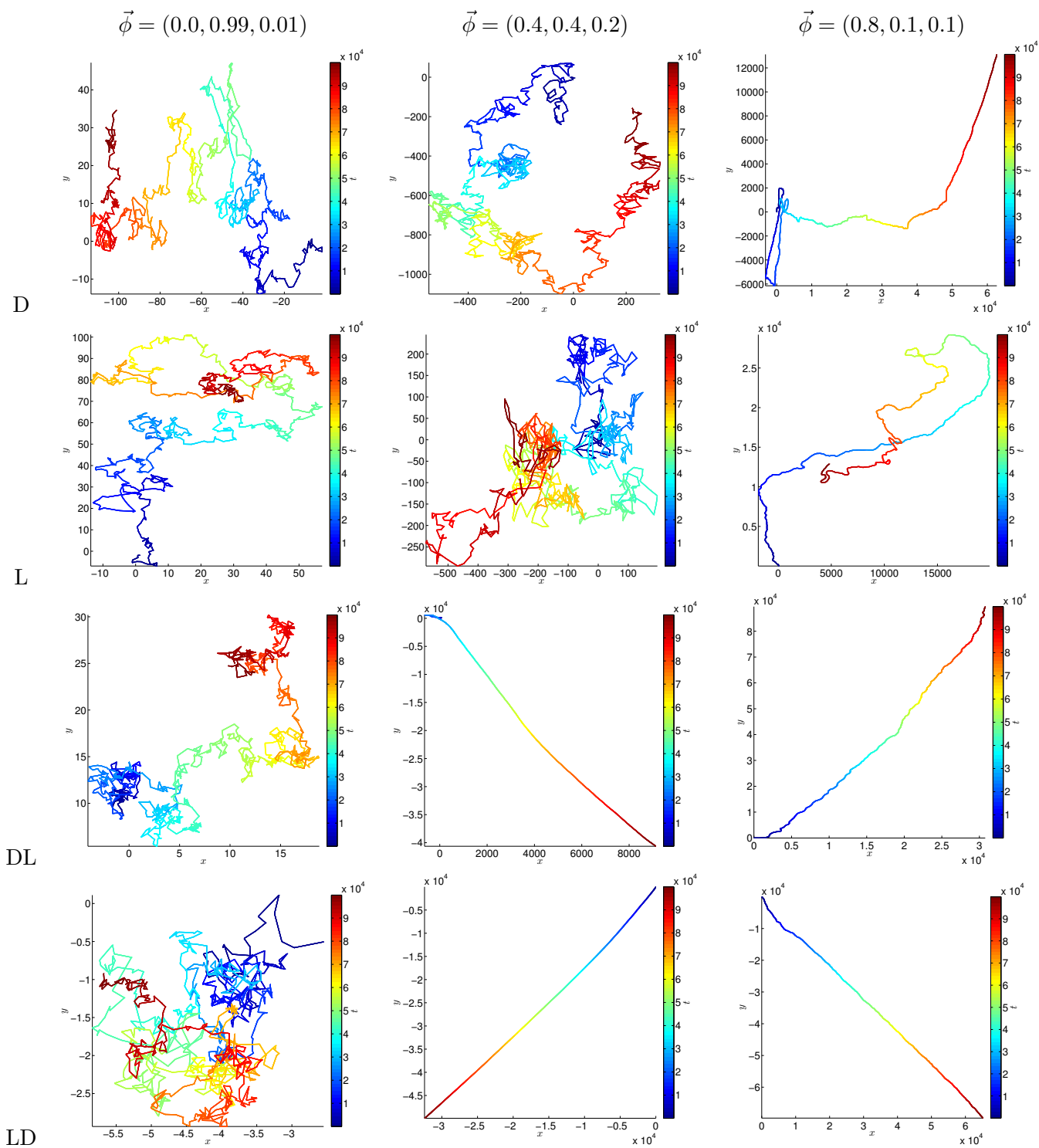Figure 3.9: Trajectories of the centre of mass of the flocks for $N = 200$ over 100,000 timesteps (including equilibration time).

95

Observed Behaviour

Lobes   A visually striking feature of these algorithms is the propensity of the flocks to form lobes when the ϕ_{flow} is close to 1. Lobes are very obvious in natural starling flocks and to obtain a qualitatively similar behaviour from these models was not expected. This is in clear contradistinction to the previously described projection model in 2D that when a large proportion of ϕ_{p} (and no alignment term ϕ_{a}) is used, produces only convex balls of individuals. Snapshots of the process of lobe formation from the initial circular flock are shown in fig. 3.10.

Inducing Alignment   One of the aims of these models was to identify a single rule that would produce both cohesion and alignment. It was hypothesised that models DL and LD, particularly LD, were most likely to produce this behaviour. To this end, simulations were run without any contribution from the alignment term, i.e. $(0, \phi_{\text{flow}}, \phi_{\text{e}})$ for the various models. As is clear from the alignment parameter planes, significant alignment does not occur without the alignment term in the basic models (see fig. 3.5 and 3.6).

There are some ways that we can adjust the basic models that might produce high alignment (Ψ). High and low velocities (10x and 0.1x the size of the individual) in addition to the introduction of inertia. The speed, v, of the individuals can be adjusted in the model as the initial length and time scales are ad hoc and a smaller velocity means more flight control decisions within the same distance travelled, due to the constant velocities being an effective (spatial) step size. An effective inertia was introduced by a modification to the velocity rule:

$$v_{t+1} = \phi_i \vec{v}_t + \phi_{\text{flow}} \vec{v}_{\text{flow}} + \vec{v}_{\text{e}} \tag{3.8}$$

Where ϕ_i is a control parameter that introduces an effective inertia. ϕ_i could be considered to arise from physical considerations (birds cannot turn as rapidly as the model animats[2]) or from memory of flight direction in the animat or a preference to continue flying in the same direction.

As can be seen from fig. 3.11a most of the tested models had a very small mean normalised flock velocity Ψ. At low proportions of the flow term ϕ_x ($x = $ D, L, DL, LD) increasing ϕ_x has little effect, but once the flow term reaches between 0.4-0.5 there is more noticeable variation between the models (on the scale shown). Model DL with $\phi_i = 10.0$ is an outlier with more rapidly decreasing Ψ with ϕ_x for small values.
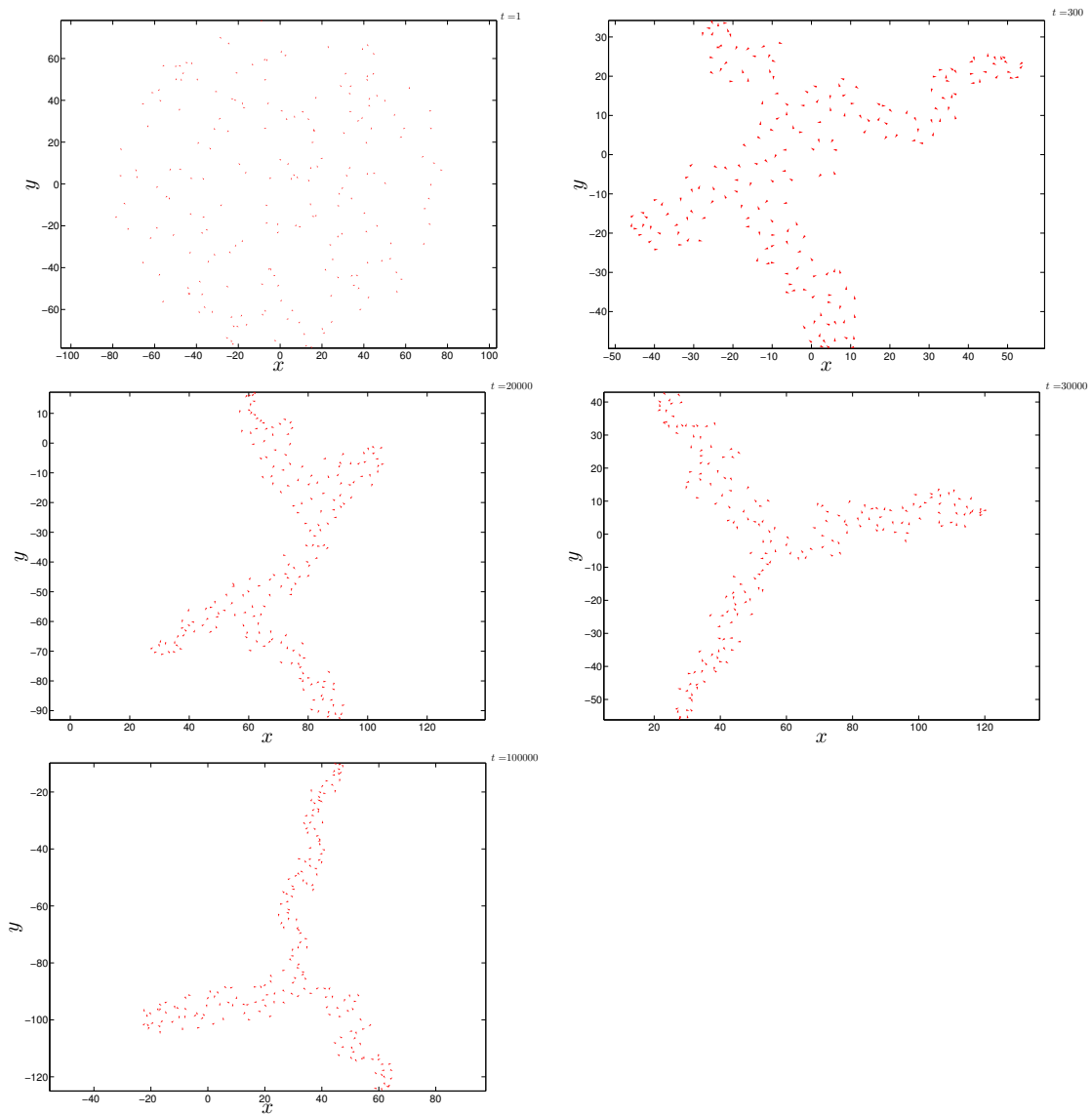
---

[2]a simulated animal

Figure 3.10: Model L $\boldsymbol{\Phi} = (0.0, 0.99, 0.01)$. The flock members are intially distributed randomly inside a circle. As the simulation proceeds, lobes form in contradistinction to the projection model, which rapidly converges to a convex 'ball' of individuals. The number of lobes gradually reduce until there are three lobes, this seems to be a stable arrangement and persists until the end of the simulation.

97

(a)

(b)
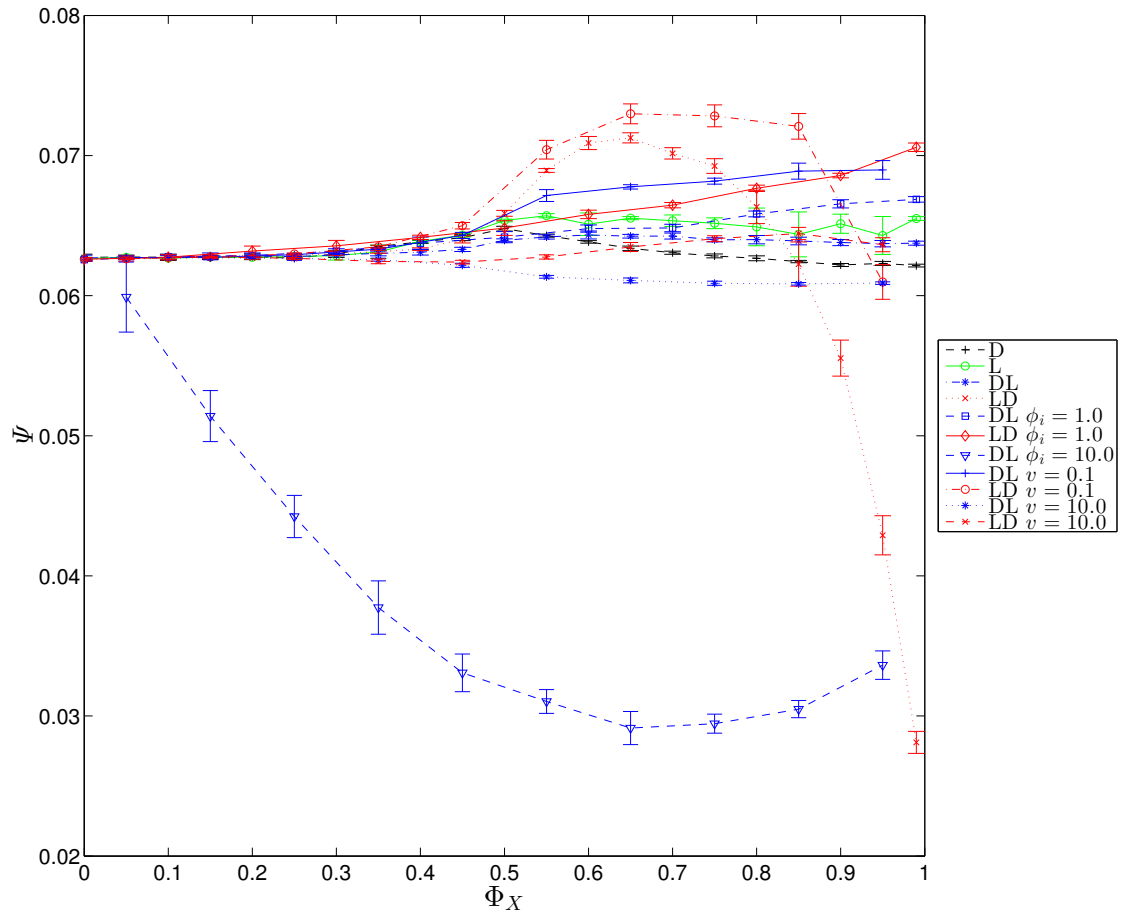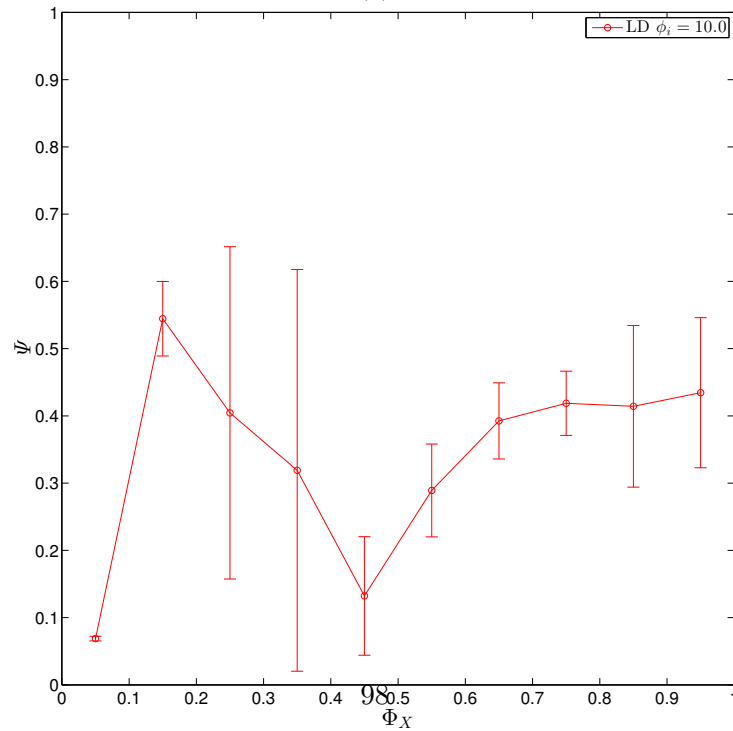
Figure 3.11: Ψ for simulated $N = 200$ flocks over 5 repeats with different speeds v and inertias ϕ_i (see Eqn. 3.8). The individual velocities were initialised with $[-\pi/4, \pi/4]$ of the x-axis to encourage linear motion. a) Most of the models tried produced had a very low mean normalised flock velocity Ψ. b) Model LD with $\phi_i = 10$ produced flocks with considerably more alignment than the others. However this is only at very low densities.

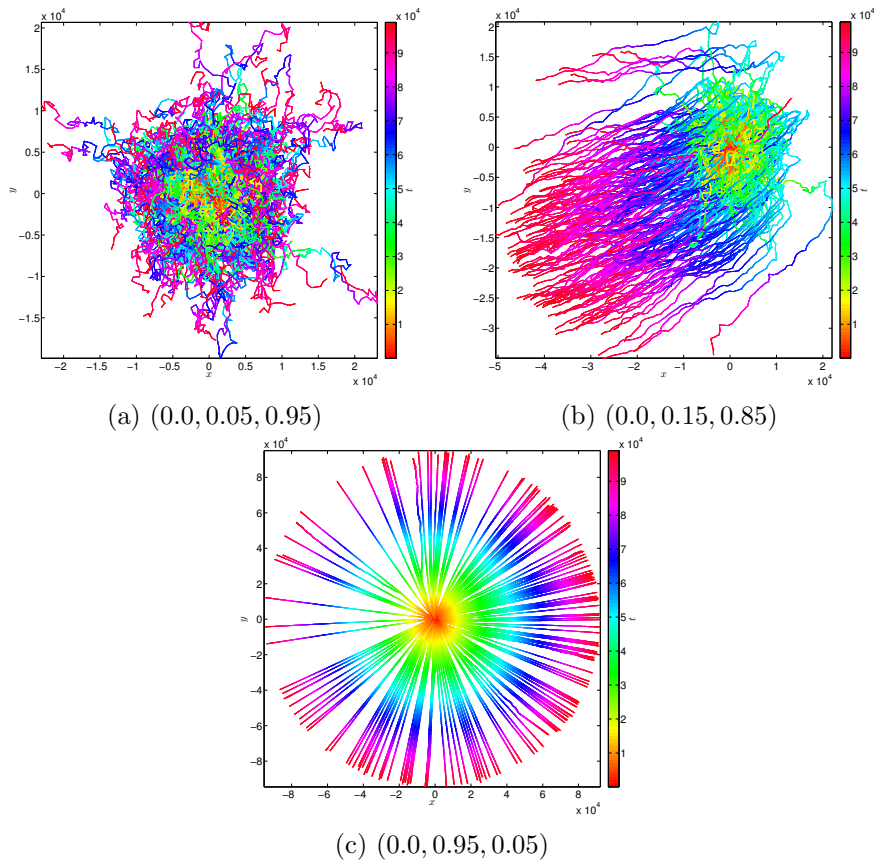(a) $(0.0, 0.05, 0.95)$ (b) $(0.0, 0.15, 0.85)$

(c) $(0.0, 0.95, 0.05)$

Figure 3.12: Trajectories for $N = 200$ particles demonstrating the range of behaviours found for model LD without noise. The behaviours are highly variable between runs and aligned flocks or expanding flocks are both found at the same parameter values.

Model LD with $\phi_i = 10.0$ is also an outlier as can be seen from fig. 3.11b. There is a considerable amount of alignment, but also much higher variability between the trial runs than for the other models. Further investigation found that the alignment occurs once a very low density has been reached. It was initially thought that model LD might enhance alignment interactions in the flock and this appears to be the case. Unfortunately any density control or cohesion, if it does occur, occurs at a density that is orders of magnitudes lower than for natural flocks.

Rotational Motion and Milling   Approximately 50% of fish species school at some point in their life-cycle and small pelagic fish, such as mackerel, are well known for 'milling' and forming a 'bait ball' when under pressure from predators [Parrish et al., 2002]. These are rotational motions of the school, characterised by high alignment among

neighbours and high density. The reason for milling in fish is unknown, but it results in highly aligned local velocities, without translation of the entire school. This may be useful as a state of readiness to respond to predation. The shapes formed by the milling fish in 3D can be cylindrical or toroidal. The bait ball, on the other hand, is though to be a panic response to the presence of nearby predators, with each fish attempting to move in to the centre of the ball.

To quantify the rotational motion in a school a further order parameter, vorticity, is useful, which will be denoted as O_{rot} [Couzin et al., 2002].

$$O_{\mathrm{rot}} = \frac{1}{N} \left| \sum_i^N \vec{u}_i \times \vec{r}_i \right| \tag{3.9}$$

where $\vec{u}_i$ is an individual i's direction and $\vec{r}_i$ their position relative to the centre of mass of the flock. O_{rot} is the mean normalised angular momentum and ranges from 0, no rotation, to 1, where all individuals are moving with velocity perpendicular to the vector from them to the centre of mass of the flock and in the same clockwise or counterclockwise direction. The modulus ensures that the direction of rotation is not taken into account, as it is assumed that this is a symmetry breaking and it is the magnitude rather than direction that is important.

When initializing the flock randomly within a circular domain, with random initial directions, unusually low alignment was observed for some simulations of model DL containing high values of the alignment term ϕ_a. Visual inspection showed rotational motion during at least part of the simulation run, probably caused by local alignments conducive to rotational motion in the initial conditions. To find the region of the parameter space for which milling is stable, the initial condition was changed, such that the maximum angular momentum was attained at initialisation. The resulting phase plane (fig. 3.13 a)) shows that rotational motion is stable, for a small region where $0.1 \leq \phi_{\mathrm{DL}} \leq 0.4$ and $0.5 \leq \phi_a \leq 0.9$. As implemented, alignment alone is not sufficient to produce rotational motion as can be seen from the $\phi_a = 0$ line in fig. 3.13 a), which has almost zero rotational order. As does $\phi_{\mathrm{DL}} = 0$ and again the model term is insufficient to produce milling, even when the flock was prepared in a favourable state with maximal angular momentum. Perhaps surprisingly model LD does not tend to display stable rotational motion (see fig 3.13 c)).

Model DL shows the greatest propensity to milling but the flocks tend to disperse, with r_{max} appearing to grow without bound (see figs. 3.14 and 3.15). This region also appears to disperse faster than the majority of the phase plane. The induced rotational
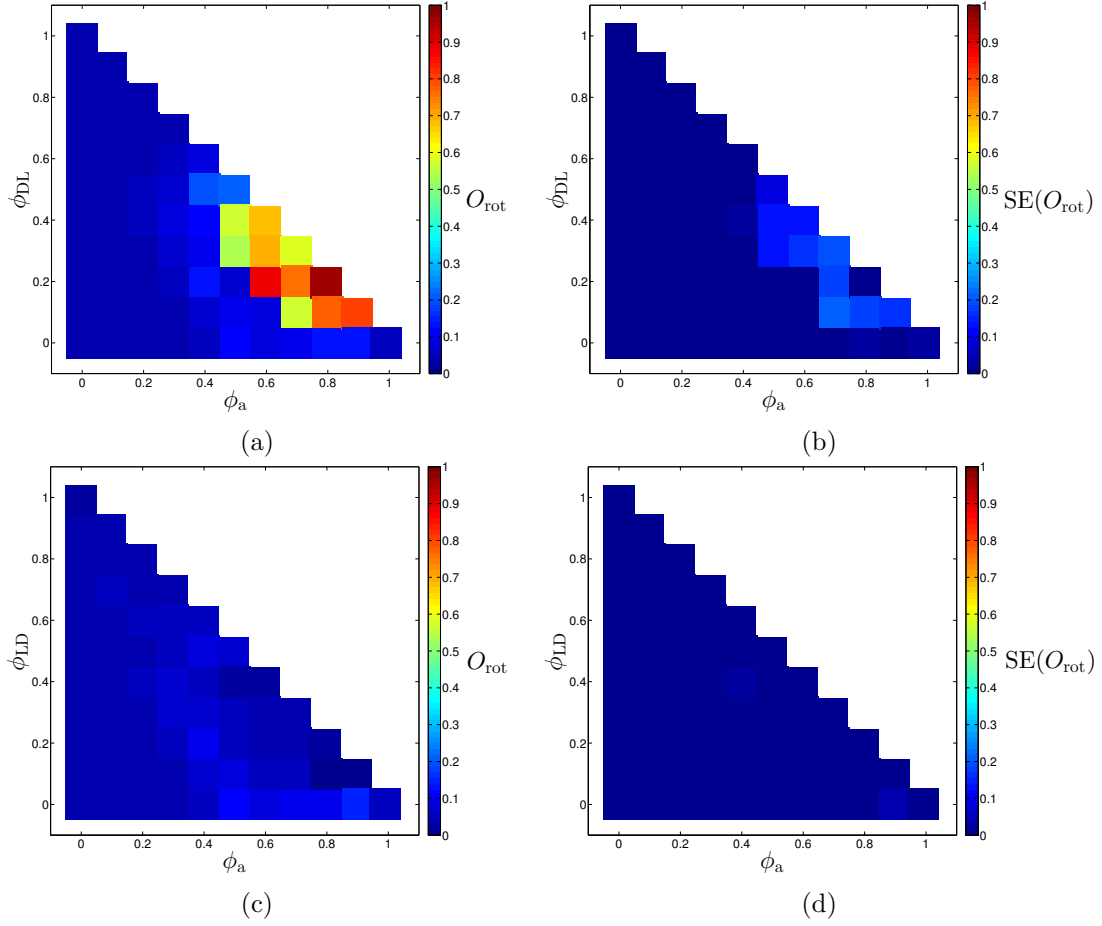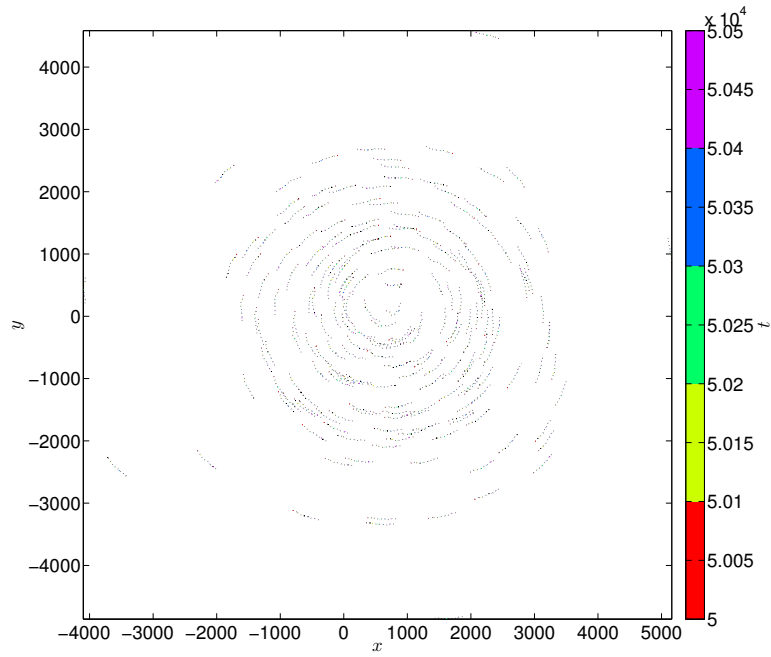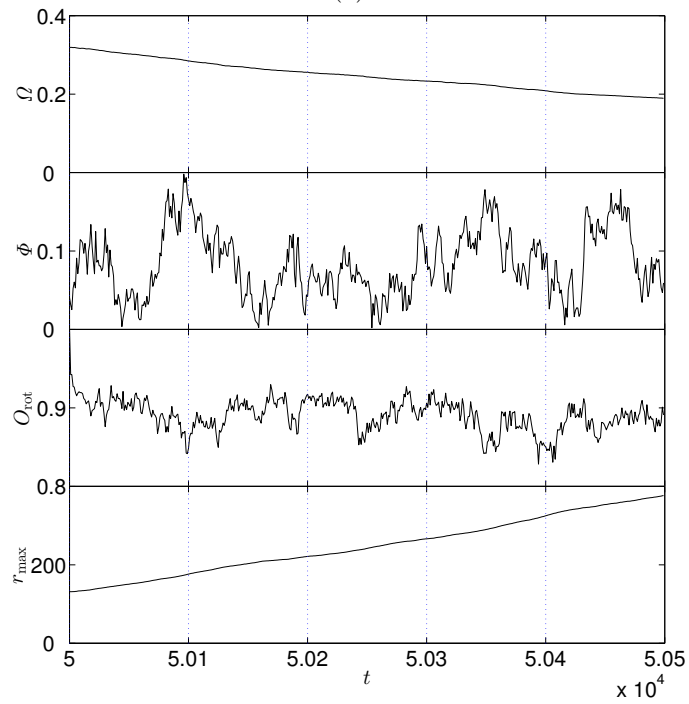
Figure 3.13: Variation of the vorticity order parameter O_{rot} with the control parameters $\vec{\phi}$: $\phi_{\mathrm{flow}} = \phi_{\mathrm{DL}}$ for model DL, etc. a) and c) phase planes for the mean rotational order parameter; b) and d) the standard error in the rotational order parameter. See §3.2.2 for discussion.

(a)

(b)

Figure 3.14: Snapshots of model DL with the number of timesteps between them $\tau = 100$, for $\vec{\Phi} = (0.6, 0.2, 0.2)$ and $N = 200$, starting at $t = 50000$ and hence the range represents 500 timesteps. The dotted lines are the individual trajectories. In the traces below, $r_{\max}$ is the maximum distance through the flock, Φ is the linear velocity order parameter, $O_{\rm rot}$ and Ω is the opacity. The blue lines are at the time points visualised in the upper plot.
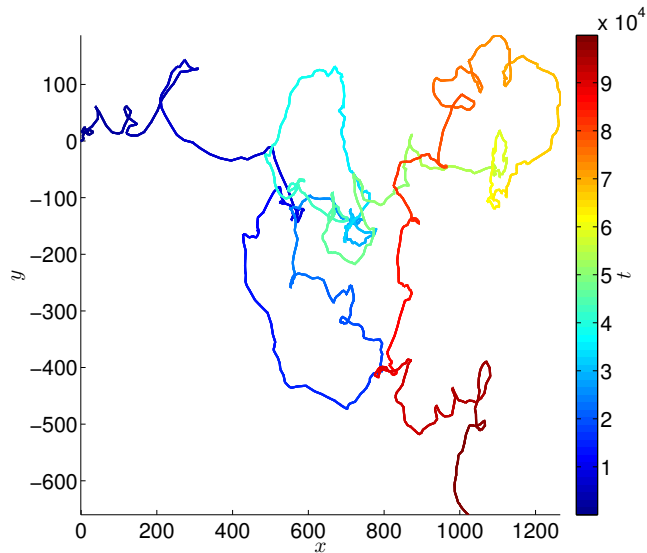
(a)
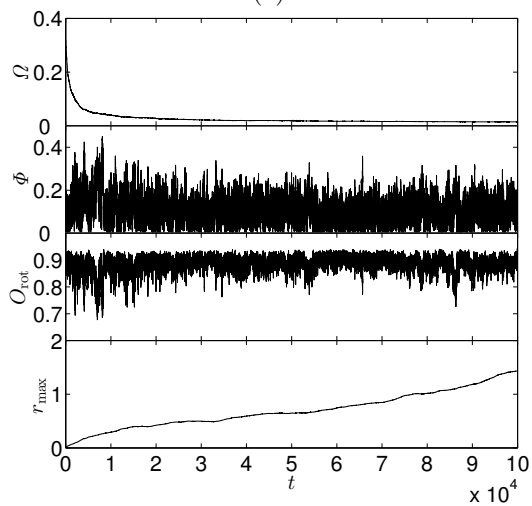
(b)

Figure 3.15: The time evolution of the center of mass of the flock a), and the values of the measured order parameters and $r_{\max}$ b) for $(0.6, 0.2, 0.2)$ and $N = 200$. The rotational order parameter O_{rot} remains high for the entire simulation run and represents persistent rotational motion. However $r_{\max}$ also continues to increase throughout the simulation, so a steady state density has not been obtained, even after a 100,000 timesteps.
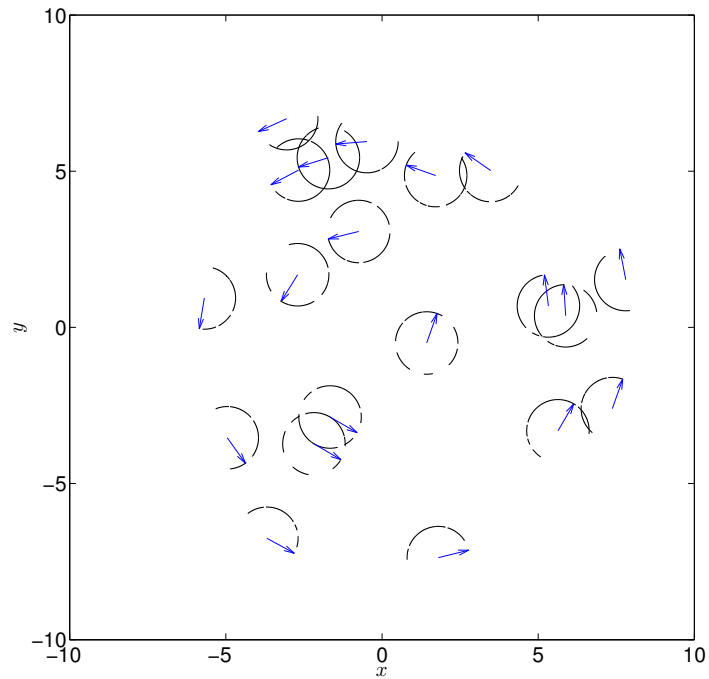
(a) $t = 0$
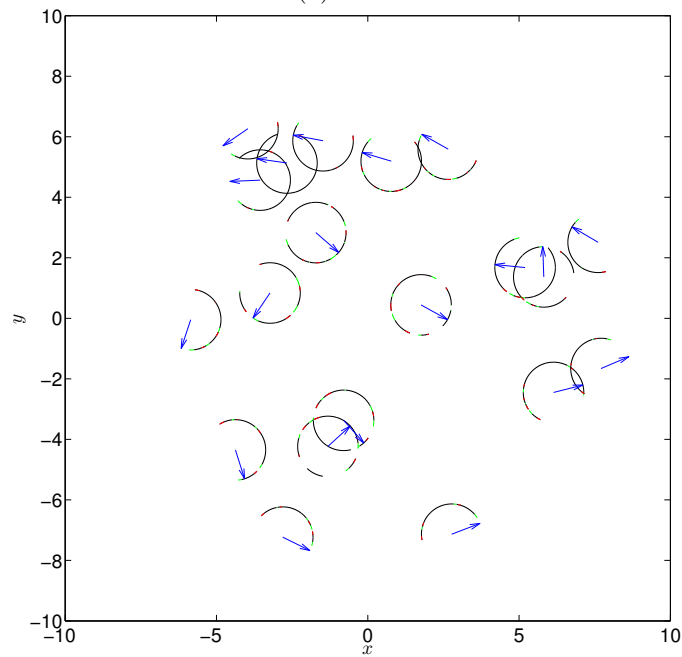
(b) $t = 1$

Figure 3.16: The set of arcs constructed by the algorithm for an $N = 20$ flock, initialised with random positions within a circular domain and with maximized O_{rot} in the initial state a) and the first timestep b). $\vec{\phi} = (0.0, 1.0, 0.0)$ and the blue arrows are the individual velocities. The black arcs represent the filled portions of the individual views and the green (resp. red) arcs, the intervals that have become empty (resp. filled).

motion is seen to continue, before eventually breaking down for many of the trajectories in and around the area of high rotational motion in the O_rot parameter plane. Linear motion changing to rotational motion was not observed in the simulations, contrary to experimental observations [Tunstrøm et al., 2013].

3.3   Discussion

The 4 models inspired by optical flow, investigated in this chapter did not produce both alignment and cohesion in the model flocks.

Further testing of models DL and LD with $\phi_a = 0$ attempted to use inertia (through Eqn. 3.8) and magnitudes for the individual velocities v_i an order of magnitude smaller and larger than the individual projections to try to find a parameter regime where the models acted as an alignment term.

Using the alignment term controlled through ϕ_a models D and L both show behaviour similar to the 3D model in chapter 2, i.e. a marginal opacity with control of the flock density, when $\vec{v}_\text{flow} > 0$ and parameter regimes with both high alignment and marginal opacity (see Figs. 3.5 and 3.5).

It was found that there is a region of parameter space for model DL that supports sustained rotation. It is a region with moderate to high alignment and low to moderate (but non-zero) ϕ_DL. Due to the symmetry of the models it is surprising that model LD does not also support these long-lived rotational states.

3.4   Future Work

It has become clear that it is difficult to invent a single simple rule that produces alignment and cohesion. Another approach would be to use a genetic algorithm to evolve a neural network controller where the inputs could be a discretised view.

Chapter 4

A 2D Simulation Model of Thermophoresis

> For those who want some proof that
> physicists are human, the proof is in
> the idiocy of all the different units
> which they use for measuring energy.
>
> Richard P. Feynman –
> *The Character of Physical Law*

This chapter focuses on a computer simulation model of the collective motion of photo-thermophoretic particles. The particles absorb light, convert the absorbed light into heat and then move in response to the induced temperature gradients. The incoming light field is circularly focused at the origin of a bounded region containing the photo-thermophoretic particles. The geometrical problem of finding regions of this focus or origin that are illuminated by an exterior light source is the complementary problem to finding the projections of other individuals on to a flock member's view in the case of birds in chapter 2. This allows for a lighting model which is can be calculated in a similar manner to the projected view used in the bird flocking simulations in chapter 2. Effectively, particles shade the optical focus, in a similar way to the birds project onto each others views.

In a first attempt, a 3D model was developed to look for a transition between a compact and diffuse particle state. Finding the transition with the 3D model proved difficult and so instead a 2D model was developed. The initial 3D model was unbounded and used the Non Uniform Fast Fourier Transform (NUFFT) centred at the optical focus.

Unfortunately the FORTRAN code for the NUFFT is not mature and this proved to be a computationally costly method to compute the temperature field. Informed by theory developed by Tamsett et al. [2016], an attempt was made to find the transition in 2D. The continuum system was bounded, so this was introduced into the simulation model also, thus obviating the need for the NUFFT. The development of the 2D simulation model is outlined in this chapter. The development of the 3D model is very similar.

4.1 Introduction

Thermophoresis, the tendency of larger particles in a liquid of smaller solvent particles to move up or down temperature gradients is well known and this response to a temperature gradient is characterised by the Soret coefficient. The case of particles moving away from heated regions is the more commonly observed case. However the mechanism for thermophoresis is still under debate. For both DNA and polystyrene beads, the sign of the thermophoretic motion (Soret coefficient) reverses at low temperature. Hence the same particles can move up or down temperature gradients depending on the bulk temperature and Duhr and Braun [2006] related this to the increasingly positive entropy of hydration at low temperatures. This response to temperature gradients can be exploited to increase local density of the larger particles, such as with DNA in Fig. 4.1.

Thermophoretic particles move in response to temperature gradients in the medium. The thermophoretic velocity is given by:

$$v_T = -D_T \nabla T \tag{4.1}$$

where D_T is called, confusingly, the 'thermal diffusion coefficient'. This is defined in contradistinction to the usual Brownian diffusion coefficient, which also depends on temperature, but scales a number density gradient. Hence in a bulk system the flux $\mathbf{J}$ and diffusion equation for a thermophoretic system with colloid concentration u are given by:

$$\mathbf{J} = -D\nabla u - uD_T\nabla T \tag{4.2}$$

$$\frac{\partial u}{\partial t} = -D\nabla^2 u - D_T u(1-u)\nabla^2 T \tag{4.3}$$

Where D is the usual Brownian diffusion coefficient and the Soret coefficient for the system is defined as $\frac{D_T}{D}$. Although in the work of Tamsett et al. [2016] omit the nonlinear term $u(1-u)$ to allow tractable analytical solutions to the PDE, this is the standard
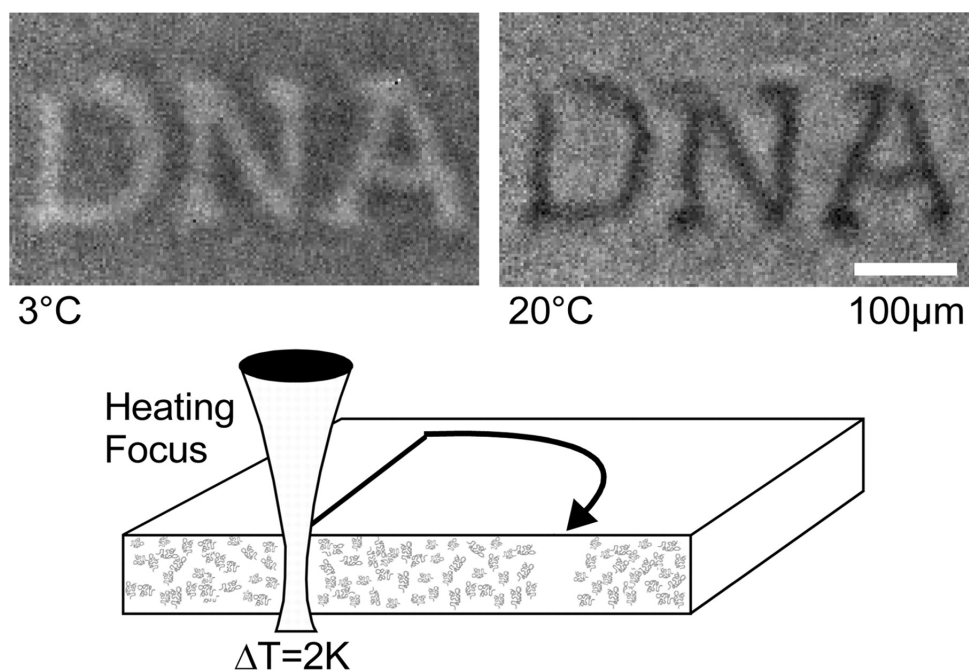
Figure 4.1: At low bulk temperature DNA particles move to the regions heated by an infrared laser. However at room temperature the reverse is true [Duhr and Braun, 2006].
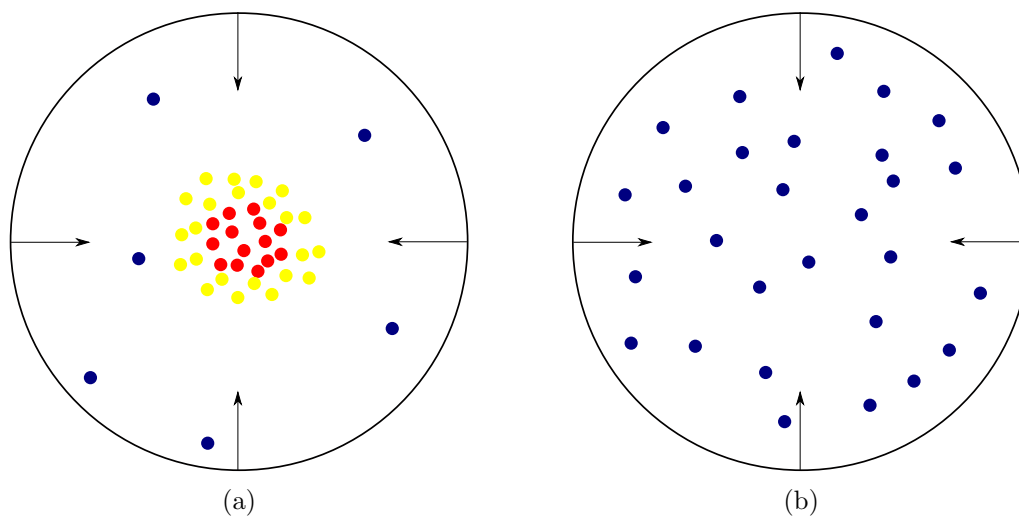
Figure 4.2: The particles exist within a circular boundary with isotropic illumination directed at a central focus. Particles absorb radiation that falls on their surface, i.e. only light rays that have not been screened (shaded) out by a particle further from the focal point. Arrows represent incoming light focused at the centre of the domain, colour indicates heating. a) Initial conditions with high particle density at the optical focus may cause sufficient heating to produce a compact state. b) diffuse states cannot produce sufficient heating to form a compact state.

representation of the bulk problem. The steady state concentration is characterised by:

$$\nabla u = -u S_T \nabla T \tag{4.4}$$

Hence, for a thermophoresing particle, the Soret coefficient indicates the relative strength of the thermophoretic drift to translational diffusion and is an important descriptor of the system [Piazza and Parola, 2008].

The Reynolds number is a dimensionless quantity representing the relative strength of inertial and viscous forces

$$\text{Re} = \frac{\rho v L}{\mu} \tag{4.5}$$

where ρ is fluid density, v is the mean velocity of the particle and L is a characteristic length scale. Low Reynolds number is a regime where viscous forces dominate and inertial forces are not important. Due to the size of the thermophoretic particles considered here (500 nm) the system is in this low Reynolds number regime.

A mean field (density) model has been developed by Tamsett et al. [2016] for an isotropically illuminated system (circularly symmetric) in 2D with isotropic density $\rho(r, \theta) = \rho(\theta)$. Steady state solutions were found for the 1D and 2D model, as a first step towards a continuum model of the collective behaviour of thermophoretic particles. This analysis posited that there would be stable compact states of the system, where the particles absorb enough light to maintain a temperature gradient large enough to keep the particles from escaping the aggregation bound together by the thermophoretic effect. The mean field model did indeed display a bifurcation, between compact and diffuse states (see Fig. 4.4). The diffuse states cannot absorb enough light to maintain the necessary temperature gradient to achieve compactness.

The model in this chapter attempts to identify the same behaviour with discrete particles and a shadowing-based model of lighting, which is not limited to steady state mean field or rotational symmetry. This simulation model can then be used to verify the mean field results and investigate dynamic properties such as stability/instability of clusters and transient behaviour. The non-dimensionalised variables $\bar{\gamma}$, $\bar{\psi}$ and $\bar{R}$ are described in §4.6.2. $\bar{R}$ is a dimensionless system size $\bar{\psi}$ corresponds to the integrated density (i.e. number) of particles along and $\bar{\gamma}$, their thermophoretic responsiveness (proportional to the irradiance and their thermophoretic movement propensity D_T).

4.2 Summary of the Mean Field Continuum Theory

Tamsett et al. [2016] developed a mean field continuum model of a collection of ther-

mophoretic particles in which hydrodynamic effects are neglected. In the model colloidal particles undergo Brownian motion with an additional drift along their orientation. This additional drift is the self-thermophoretic component and models the interaction of a thermophoretic particle with a well-defined orientation, such as a half coated polystyrene bead (i.e. a Janus particle). Janus particles are impelled along their axis of rotational symmetry by the thermophoretic effect. However in any reasonably small volume there will be a distribution of orientations and the self thermophoretic component averages to zero locally, resulting in isotropic heating of the surrounding fluid. The temperature imhomogeneities and hence the gradients that the colloidal particles respond to are caused by non-uniform particle distributions (i.e. the particle density) and shading of particles which prevents local heating. Hence the self-thermophoretic effect, which averages out to zero is not important and can be safely neglected from the model.

The mean field continuum model predicts the formation of compact states, which are heated on the boundary by absorption of incident light. The compact states are predicted to be hotter in the interior, which is simply a consequence of the geometry of the heat sources. An extreme case is to consider a 2D (x, y) slice through a cylindrical heat bath, the walls of which are kept at a constant temperature and with no heat or particle conduction in the z-direction. Even in an extreme case where the particles in the heat bath were to be arranged in a ring around the bath's centre, with no additional heat sources inside the ring, then the centre must be the hottest part of the bath, as heat is conducted outwards and inwards radially through the fluid until the centre is as hot as the ring of sources and then heat flows out of the bath at steady state. However in the compact state there will also be some interior heat sources, unless the state were to be fully opaque (which it is not predicted to be). It follows that in any stationary state that is predicted by the mean field model, the interior of the compact state must have a uniform temperature profile, or there will be a change in the density profile through the thermophoretic response.

4.2.1 The Continuum Model

The equations of motions for the model are now described.

The colloid number conservation:

$$\frac{\partial \rho}{\partial t} = -\nabla \cdot \vec{j} \tag{4.6}$$

where ρ is the density of colloids and $\vec{j}$ is the colloid current.

$$\vec{j} = -D\nabla\rho - D_T\rho\nabla T \tag{4.7}$$

the first term of which is the usual Brownian diffusion and the second term the thermophoretic response of the colloids to the local temperature gradient. The Soret coefficient $\frac{D}{D_T}$ can be temperature dependent, but this was not considered.

The heat equation defines the temperature field:

$$\frac{\partial T}{\partial T} = \kappa\nabla^2 T + \Gamma[\rho(x)] \tag{4.8}$$

$\kappa\nabla^2 T$ describes heat conduction through the fluid medium and $\Gamma[\rho(x)]$ the heating due to heat sources. In this model the heat sources are the thermophoretic colloidal particles themselves. In 1D the heat equation with sources does not have a steady state solution on an infinite domain, as the temperature becomes infinite everywhere. If however, the problem is considered on a finite domain $x \in [-\bar{x}, \bar{x}]$ with boundary conditions $T(\pm\bar{x}) = 0$ a solution may be found and then by taking $\bar{x} \to \infty$. That despite having an infinite temperature the solution converges to have a finite temperature gradient. The finite temperature gradient is the important part as the thermophoretic particles respond to the temperature gradient *not* the temperature itself. Hence steady state solutions can be found for the 1D particle distribution, by requiring zero current everywhere.

The 1D Heat Source Term

The heat sources are the colloidal particles, which convert intercepted light into heat. Over a small interval $x \in [x, \Delta x]$ for which the density of particles ρ is approximately uniform, the light absorbed and hence the heating is proportional to ρ, i.e. the relationship between illuminance I and ρ is:

$$\frac{I(x + \Delta x) - I(x)}{I(x + \Delta x)} = \alpha\rho(x + \Delta x)\Delta x \tag{4.9}$$

or as we take $\Delta x \to 0$

$$\frac{dI}{dx} = \alpha\rho(x)I(x) \tag{4.10}$$

This is a first order differential equation with solution:

$$I(x) = I_\infty e^{-\alpha\int_x^\infty \rho dx'} \tag{4.11}$$

where α is the absorbance of a particle, the fraction of incident light on a particle absorbed by it.

If light is incident from both the left $(+)$ and right $(-)$, the heating term is

$$\Gamma(x) = \frac{1}{c\rho_f} \left(\frac{dI_+}{dx} - \frac{dI_-}{dx} \right) \tag{4.12}$$

where $c\rho_f$ is the specific heat capacity of the surrounding fluid $\times$ its density. this factor accounts for the heating of the medium per Joule of energy put into the system by absorbed light. Omitting some trigonometric substitutions and algebra

$$\Gamma(x) = \frac{2\alpha}{c\rho_f} \sqrt{I_\infty I_{-\infty}} e^{-\alpha N/2} \rho(x) \cosh \left[\alpha \int_x^\infty \rho dx' - \frac{\alpha N}{2} - \frac{1}{2} \ln \left(\frac{I_\infty}{I_{-\infty}} \right) \right] \tag{4.13}$$

1D Equations of Motion

Substituting for the source term in the heat equation, results in the following 1D equations of motion for the system:

$$\frac{\partial}{\partial t}T = \kappa \frac{\partial^2}{\partial x^2}T$$
$$+ \frac{2\alpha}{c\rho_f} \sqrt{I_\infty I_{-\infty}} e^{-\alpha N/2} \rho(x) \cosh \left[\alpha \int_x^\infty \rho dx' - \frac{\alpha N}{2} - \frac{1}{2} \ln \left(\frac{I_\infty}{I_{-\infty}} \right) \right] \tag{4.14}$$
$$\frac{\partial}{\partial t}\rho = D \frac{\partial^2}{\partial x^2}\rho + D_T \frac{\partial}{\partial x} \left(\rho \frac{\partial}{\partial x}T \right) \tag{4.15}$$

with boundary conditions on the temperature $T(\pm\bar{x}) = 0$ and a condition on the conservation of particles $N = \int_{-\bar{x}}^{\bar{x}} \rho(x,t)dx'$. As the equations only contain derivatives of T, $T(\pm\bar{x})$ is an arbitrary constant and can be fixed to 0 for convenience. Comparisons with an actual heat bath would require shifting the temperature of the system by a constant T_0.

To enable solving these equations of motion were de-dimensionalised and a new variable ψ introduced to incorporate the integral on the RHS of Eqn 4.14.

$$\rho(x,t) = \lambda\tilde{\rho}(\xi,t) \tag{4.16}$$
$$x = \frac{\xi}{\lambda} \tag{4.17}$$
$$T = -\frac{D}{D_T}\bar{T} \tag{4.18}$$
$$t = \frac{\tau}{\kappa\lambda^2} \tag{4.19}$$

Normalising the density $\tilde{\rho} = N\bar{\rho} \implies \int_{-\hat{\xi}}^{\hat{\xi}} \hat{\rho} d\xi$, choosing $\lambda = -\frac{2D_T \sqrt{I_{-\infty} I_\infty}}{c\rho_f \kappa D}$ and defining $a = \alpha N$ leads to the de-dimensionalised equations of motion. The new variable $\psi = -a\left(\int_{\hat{\xi}}^{\hat{\xi}} \bar{\rho} d\xi - \frac{1}{2}\right)$ can be introduced at this point. ψ is 0 at the centre of the particle distribution with symmetric boundary conditions. This is the case when the particle advection velocity is 0, which gives some insight into the physical meaning of ψ. There is the possibility of travelling solutions for the particle density, which would be caused by anisotropic illumination on the sides of the distribution, i.e. if $I_\infty \neq I_{-\infty}$. Note that this possibility will not be expanded on as we are interested in stable compact and *static* states. A further substitution for convenience is $\phi(\xi, \tau) = \frac{\partial \bar{T}}{\partial \xi}$. This is useful as static solutions exist for the temperature gradient, but not the temperature in 1D on an infinite domain. The new equations of motion are

$$\frac{\partial \phi}{\partial \tau} = \frac{\partial^2 \phi}{\partial \xi^2} + e^{-a/2} \frac{\partial^2 \phi}{\partial \xi^2} \sinh\left(\psi + \frac{1}{2}\ln\left[\frac{I_\infty}{I_{-\infty}}\right]\right) \quad (4.20)$$

$$\frac{\kappa}{D}\frac{\partial \psi}{\partial \tau} = \frac{\partial^2 \psi}{\partial \xi^2} - \phi\frac{\partial \psi}{\partial \xi} \quad (4.21)$$

The thermal conductivity of the fluid is considerably faster than the particle diffusion, which allows for a quasi-static approximation. Due to the heating through the light absorbed by the particles, the temperature gradient field in the quasi-static case is a function of the density field or equivalently ψ, i.e. $\phi(\xi, \tau) = U[\psi(\xi, \tau)]$. On an infinite domain,

$$\phi(\xi, \tau) = \bar{\phi} - e^{-a/2} \sinh\left[\psi(\xi, \tau) + \frac{1}{2}\ln\left[\frac{I_\infty}{I_{-\infty}}\right]\right] \quad (4.22)$$

and where $\bar{\phi} = \frac{1+e^{-a}}{4}\frac{I_\infty - I_{-\infty}}{\sqrt{I_\infty I_{-\infty}}}$ This leads to a generalized Burger's equation

$$\frac{\kappa}{D}\frac{\partial \psi}{\partial \tau} + U[\psi]\frac{\partial \psi}{\partial \xi} = \frac{\partial^2 \psi}{\partial \xi^2} \quad (4.23)$$

As might be expected for a Burger's-type equation there may be the afore-mentioned travelling solutions in addition to the static solutions that we are interested in.

In the simplest case of symmetric illumination $I_{-\infty} = I_\infty$ the static case is defined by $\frac{\partial \phi}{\partial \tau} = \frac{\partial \psi}{\partial \tau} = 0$. From Eqn 4.22

$$\phi(\xi) = -e^{-a/2} \sinh[\psi(\xi)] \quad (4.24)$$

This can be substituted into the equation for ψ and the resulting integral equation solved

for ξ.

$$\xi = \frac{2}{\sqrt{c^2 - e^{-1}}} \text{arctanh} \left[\sqrt{\frac{c + e^{-a/2}}{c - e^{-a/2}}} \tanh \left[\frac{\psi}{2} \right] \right] \tag{4.25}$$

This can be inverted to solve for ψ and invoking the boundary condition $\psi(\pm\infty) = a/2$

$$\psi\xi = 2\text{arctanh} \left[\tanh \left[\frac{a}{4} \right] \tanh \left[\frac{1 - e^{-a}}{4} \xi \right] \right] \tag{4.26}$$

From the equation for the density $\bar{\rho} = \frac{1}{a} \frac{d\psi}{d\xi}$

$$\bar{\rho}(\xi) = \frac{\frac{1}{2a}(1 - e^{-a/2})^2}{1 + \frac{\sinh^2\left[\frac{1-e^{-a}}{4}\xi\right]}{\cosh^2\left[\frac{a}{4}\right]}} \tag{4.27}$$

Asymptotic analysis discriminates 2 phases for $a \ll 1$ a non-shading limit

$$\bar{\rho} \sim \frac{a}{8}\text{sech}^2 \left[\frac{a}{4}\xi \right] \tag{4.28}$$

and for $a \gg 1$ an opaque limit

$$\bar{\rho} \sim \frac{1/2a}{1 + \exp\left[-\frac{1}{2}(a - |\xi|)\right]} \tag{4.29}$$

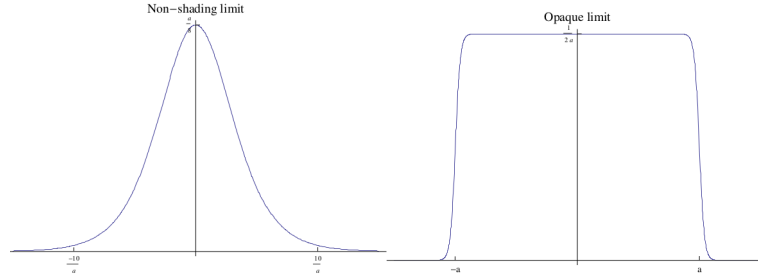In the diffuse, non-shading limit almost none of the incident light is absorbed by particles

Figure 4.3: Exact solutions for $a \ll 1$ the non-shading limit (left) and $a \gg 1$ the opaque limit (right). (Courtesy of Arran Tamsett)

and the heating of the fluid is proportional to local particle density. In the opaque limit all the heating occurs at the edge, where density goes to zero exponentially. Hence in the opaque state particles can fuse diffuse freely in the centre, but are constrained by high temperature gradients at the edges.

114

4.2.2 The 2D Continuum Model

In 2D the incoming light is focused at the centre of a circular domain. Consider an annulus $r' \in [r, r + \Delta r]$. Energy enters at the far edge of the annulus at the rate $\dot{E}_{\text{in}} = I(r + \Delta r)2\pi(r + \Delta r)$ and the energy leaving the annulus at the edge nearest to the central focus is $\dot{E}_{\text{out}} = I(r)2\pi r$, where $I(r')$, the irradiance is a function of the radius. Therefore the energy absorption rate is

$$\dot{E}_{\text{abs}} = 2\pi(I(r + \Delta r)(r + \Delta r) - I(r)r) \tag{4.30}$$

The light absorbed is again an integral over regions of infinitesimal thickness (Δr) and proportional to the proportion of the annulus screened by particles in the annulus. Hence the proportion of energy absorbed is

$$\frac{2\pi(I(r + \Delta r)(r + \Delta r) - I(r)r)}{2\pi I(r + \Delta r)(r + \Delta r)} = \rho 2\pi r \Delta r \frac{2r_0}{2\pi r} \tag{4.31}$$

where r_0 is the particle radius. Taking $\Delta r \to 0$ gives

$$\frac{d}{dr}[rI] = 2r_0 \rho r I \tag{4.32}$$

$$\implies rI(r) = RI(R)\exp\left[-2r_0 \int_r^R \rho dr'\right] \tag{4.33}$$

where R is the radius of the system. Let $Q = 2\pi R I(R)$ be the rate of injection of energy into the system then

$$rI_{\text{in}}(r) = \frac{Q}{2\pi}e^{-2r_0 \int_r^R \rho dr'} \tag{4.34}$$

Not all the incoming radiation will be absorbed and some will pass through the focus and become outgoing radiation, this provides a second opportunity for that light to be absorbed. Following similar reasoning as for incoming light

$$rI_{\text{out}}(r) = \frac{Q}{2\pi}e^{-2r_0 \int_0^R \rho dr'} \tag{4.35}$$

The rate of energy absorption into the shell $r' \in [r, r + \Delta r]$ is

$$\dot{E} = 2\pi\left(I_{\text{in}}(r + \Delta r)(r + \Delta r) - I_{\text{in}}(r)r\right) + 2\pi\left(I_{\text{out}}(r + \Delta r)(r + \Delta r)\right) \tag{4.36}$$

If the energy ΔE is absorbed into the shell, then the temperature increase $\Delta T = \frac{\Delta E}{c\rho_f 2\pi r \Delta r}$ and the rate of temperature change $\Delta \dot{T} = \frac{\Delta \dot{E}}{c\rho_f 2\pi r \Delta r}$. Thus the heat source term for the

2D heat equation is

$$\Gamma(r) = \frac{1}{c\rho_f r}\left(\frac{d}{dr}(rI_{in}) - \frac{d}{dr}(rI_{out})\right) \tag{4.37}$$

$$= \frac{1}{c\rho_f r}\left(2r_0\rho r I_{in} + 2r_0\rho r I_{out}\right) \tag{4.38}$$

$$= \frac{2r_0 Q}{\pi c\rho_f}e^{-2r_0\int_0^R \rho dr}\frac{\rho}{r}\cosh\left[2r_0\int_0^r \rho dr'\right] \tag{4.39}$$

2D Equations of Motion

For the 2D case of symmetric particle distribution and illumination

$$\frac{\partial T}{\partial t} = \frac{\kappa}{r}\frac{\partial}{\partial r}\left(r\frac{\partial T}{\partial r}\right) + \frac{2r_0 Q}{\pi c\rho_f}e^{-2r_0\int_0^R \rho dr'}\frac{\rho}{r}\cosh\left[2r_0\int_0^r \rho dr'\right] \tag{4.40}$$

$$\frac{\partial \rho}{\partial t} = \frac{D}{r}\frac{\partial}{\partial r}\left(r\frac{\partial \rho}{\partial r}\right) + \frac{D_T}{r}\frac{\partial}{\partial r}\left(r\rho\frac{\partial T}{\partial r}\right) \tag{4.41}$$

To simplify matters de-dimensionalisation can be used as before

$$r = \frac{\bar{r}}{\lambda} \tag{4.42}$$

$$t = \frac{\tau}{\kappa\lambda^2} \tag{4.43}$$

$$T = \frac{-D}{D_T}\bar{T} \tag{4.44}$$

$$\rho(r,t) = N\lambda^2\bar{\rho}(\bar{r},\tau) \tag{4.45}$$

$N = 2\pi\int_0^R \rho r dr$ is the total of number of particles and $\bar{\rho}$ is the normalised density. Defining

$$\gamma = -\frac{D_T Q}{\pi c\rho_f \kappa D} \tag{4.46}$$

$$a = 2r_0 N \tag{4.47}$$

$$\bar{R} = \lambda R \tag{4.48}$$

γ represents the amount of work done on the system through heating controlled by Q. These substitutions result in a set of equations with 3 parameters, but λ is left to be fixed. Fixing λ the inverse length-scale will result in 2 parameters. One way to fix λ is to let $a = 1$ to remove a from the exponent. Thus the length-scale

$$\lambda^{-1} = 2r_0 N \tag{4.49}$$

Hence the length-scale of the system is the length of all the particles in the system arranged in a line. From this definition of λ

$$\bar{R} = \frac{R}{2r_0 N} \tag{4.50}$$

is the dimensionless system size. If $\bar{R} = 1$ then all the particles may be arranged in a line from the centre to the edge. Hence if the particles are arranged isotropically, along any line of sight the expected number of particles is 1, i.e. the system is *marginally opaque*. Therefore $R \gg 1$ results in a highly diffuse and transparent system and $R \ll 1$ is completely opaque. Applying this scaling results in the following de-dimensionalised equations

$$\frac{\partial \bar{T}}{\partial \tau} = \frac{1}{r} \frac{\partial}{\partial \bar{r}} \left(\bar{r} \frac{\partial \bar{T}}{\partial \bar{R}} \right) + \gamma e^{-\int_0^{\bar{R}} \bar{\rho} d\bar{\rho}} \frac{\bar{\rho}}{\bar{r}} \cosh \left[\int_0^{\bar{r}} \bar{\rho} d\bar{r}' \right] \tag{4.51}$$

$$\frac{\kappa}{D} \frac{\partial \bar{\rho}}{\partial \tau} = \frac{1}{\bar{r}} \frac{\partial}{\partial \bar{r}} \left(\bar{r} \frac{\partial \bar{\rho}}{\partial \bar{r}} \right) - \frac{1}{\bar{r}} \frac{\partial}{\partial \bar{r}} \left(\bar{r} \frac{\partial \bar{T}}{\partial \bar{r}} \right) \tag{4.52}$$

Henceforth in this section we are dealing with dimensionless variables and the overbars indicating them will be omitted. Once again we are interested in static solutions and we continue to require radial symmetry. The static case $\frac{\partial T}{\tau} = 0$, reduces the radially symmetric 2D heat equation with sources to the 2D Poisson equation, $\nabla^2 T = -\Gamma(r)$. Setting the temperature at the boundary to 0, i.e. $T(R) = 0$, the Poisson equation has general solution

$$T(r) = \ln R \int_0^R \Gamma(r') dr' - \ln R \int_0^r \Gamma(r') dr' - \ln R \int_r^R \ln r' \Gamma(r') dr' \tag{4.53}$$

Integrating once we find

$$r \frac{dT}{dr} = -\gamma e^{-\int_0^R \rho dr} \sinh \left[\int_0^r \rho dr' \right] \tag{4.54}$$

The zero current condition gives $\frac{d\rho}{dr} = \rho \frac{dT}{dr}$ and thus

$$\frac{d\rho}{dr} = -\gamma e^{-\int_0^R \rho dr} \frac{\rho}{r} \sinh \left[\int_0^r \rho dr' \right] \tag{4.55}$$

As in the 1D case it is useful to define $\psi(r) = \int_0^r \rho dr'$. This transforms the equation to

$$r \frac{d^2 \psi}{dr^2} + \gamma e^{-\bar{\psi}} \frac{d\psi}{dr} \sinh [\psi] = 0 \tag{4.56}$$

where $\bar{\psi} = \psi(\bar{R})$. Using $r\frac{d^2\psi}{dr^2} = \frac{d}{dr}\left(r\frac{d\psi}{dr}\right) - \frac{d\psi}{dr}$ this can be integrated once to give

$$r\frac{d\psi}{dr} - \psi + \gamma e^{-\bar{\psi}}\cosh[\psi] = c \tag{4.57}$$

From asymptotics at low density and ignoring the constraint on maximum density, the density at the origin may be finite in which case $r\frac{d\psi}{dr}|_{r=0} \implies c = \gamma e^{-\bar{\psi}}$, or infinite in which case the total number of particles is finite $\int_0^\epsilon \rho r dr < \infty \,\forall \epsilon$. If for small r, $\rho \sim r^{-\alpha}$, from $\int_0^\epsilon \rho dr < \infty$, then $\alpha < 1$ and again $r\frac{d\psi}{dr}|_{r=0} \implies c = \gamma e^{-\bar{\psi}}$. Also, from the nomalisation condition $1 = 2\pi \int_0^R \frac{d\psi}{dr} r dr$, integration by parts gives $1 = 2\pi R\bar{\psi} - 2\pi \int_0^R \psi dr$. This leads to a pair of equations for ψ, which defines a kind of nonlinear eigenvalue problem for $\bar{\psi}$, which can be solved numerically.

$$0 = r\frac{d\psi}{dr} - \psi + 2\gamma e^{-\bar{\psi}}\sinh^2\left[\frac{\psi}{2}\right] \tag{4.58}$$

$$\bar{\psi} = \frac{1}{2\pi R} + \frac{1}{R}\int_0^R \psi dr \tag{4.59}$$

where $\bar{\psi} = \psi(R)$ as before.

The Continuum Bifurcation

In the mean field continuum model, there is a bifurcation between compact and diffuse states (see Fig. 4.4). This can be obtained by numerically solving Eqns 4.58 and 4.59 self-consistently for $\bar{\psi}$. There are constraints on ψ originating from its relationship to density. $\bar{\psi}$ cannot have a negative gradient (ψ is a monotonically increasing function of r). Therefore

$$R\frac{d\psi}{dr}|_R \geq 0 \implies -\bar{\psi} + 2\gamma e^{-\bar{\psi}}\sinh^2\left[\frac{\bar{\psi}}{2}\right] \geq 0 \tag{4.60}$$

$$\implies \gamma \leq \frac{2\bar{\psi}}{\left(1 - e^{-\bar{\psi}}\right)^2} \tag{4.61}$$

Also $\bar\psi$ is limited by the maximum density attainable (where the particles are as closely packed as possible)

$$\rho(r) = \begin{cases} 4N, & r \le \frac{1}{\sqrt{\pi 4N}} \\ 0, & r \ge \frac{1}{\sqrt{\pi 4N}} \end{cases} \tag{4.62}$$

$$\implies \psi(r) = \begin{cases} 4Nr, & r \le \frac{1}{\sqrt{\pi 4N}} \\ \sqrt{\frac{4N}{\pi}}, & r \ge \frac{1}{\sqrt{\pi 4N}} \end{cases} \implies \bar\psi \le \sqrt{\frac{4N}{\pi}} \tag{4.63}$$

The bifurcation diagram can be obtained either numerically or from an approximate solution to the mean field equations. Depending on the value of the dimensionless system size $\bar\psi$, there can be a cusp bifurcation from the high density state in the upper branch (high $\bar\psi$ and γ) and a lower density state (low ψ). These states are those that are either sufficiently compact for them to absorb sufficient light energy for thermophoresis to maintain them (the upper branch), or too diffuse to absorb sufficient light energy for thermophoresis to hold them together (the lower branch).

If the dimensionless system size $\bar R$ is too small then the particles can only be in the compact state and there is no cusp bifurcation, e.g. $\bar R = 0.5$ in Fig. 4.4. The main
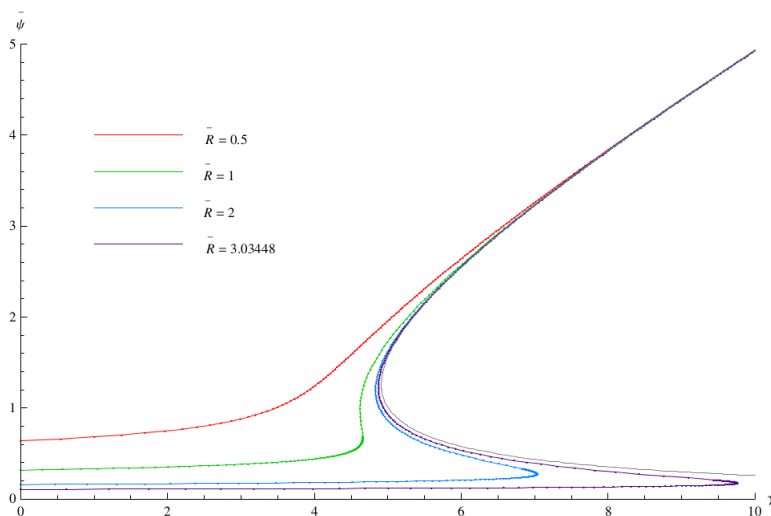

Figure 4.4: The bifurcation diagram for the continuum model. High $\bar\psi$ corresponds to a more compact state and $\bar\gamma$ to an increased importance of thermophoresis. $\bar R$ is the dimensionless system size. $\bar R \gg 1$ corresponds to transparent states in the fully disperse limit ($\bar\gamma \to 0$). Systems prepared in these states could possibly exhibit a transition to a compact state. Whereas $\bar R \le 1$ systems cannot as they are already optically compact. (Courtesy of Arran Tamsett)

aim of this chapter is to find evidence of the cusp bifurcation through direct particle simulation and determine whether the compact states are stable states.

Connection to Previous Chapters

It is known that polystyrene beads will move along temperature gradients in liquids and the particles in this model might therefore be thought of as polystyrene beads [Duhr and Braun, 2006]. Beads partially coated in metal can absorb laser light and re-emit the absorbed energy as heat [Golestanian, 2010]. This can result in thermophoresis in which case they are self-propelled particles somewhat resembling the birds in previous chapters [Jiang et al., 2010].

4.3 Direct Particle Simulation Model Description

The simulation is based on a hypothetical experimental setup, whereby thermophoretic particles are confined in a cylindrical domain, which is isotropically illuminated by a concentric external light source focused on the central axis of the cylindrical domain. If the density of particles is high enough, they should cause a large enough temperature gradient to form an aggregation, otherwise they should disperse and fill the (bounded) domain. The 2D simulation is a 1 particle thick 'slice' through this cylinder. See fig. 4.2.

The thermophoretic colloidal particles are assumed to be spherical and undergo thermophoretic motion, but not *self*-thermophoretic motion. I.e. they do not respond to the local temperature distribution caused by differences in heating on the particle's surface. Essentially the particle is assumed to instantaneously thermally equilibrate (internally and with its surrounding) and it has no effect on itself (due to the symmetry of the particle).

The particles move up temperature gradients to regions of higher temperature (negative Soret coefficient) and hence may cluster. In addition to thermophoretic motion there will be thermal noise due to the surrounding medium, leading to diffusive motion as usual. The particles are assumed to be large compared to the solvent particles of the medium and hence the noise can be modelled as Brownian motion. The particles are also large enough to absorb rather than scatter the incoming light, i.e. the particle radius $r_0 \gg \lambda$, where λ is the wavelength of the incident light.

A numerical Langevin equation approach is used for the particle dynamics, integrated using the Euler-Maruyama approximation, which is a generalisation of the Euler

method to stochastic differential equations. Time $t = \Delta t \times i$ and $\mathbf{x}_i$ is the position of particle i at timestep i.

$$\frac{d\mathbf{x}_i}{dt} = -D_T \nabla T + \sqrt{2D} \eta_i \tag{4.64}$$

The brownian noise is modelled as

$$\langle \eta_i(t) \eta_j(t') \rangle \geq \delta_{ij} \delta_{tt'} \tag{4.65}$$

$$\langle \eta_i(t) \rangle = 0 \tag{4.66}$$

Stoke's law for frictional force gives a value for the thermal diffusion constant of spheres at low Reynolds numbers

$$D = \frac{k_b T_{\text{lab}}}{6\pi\eta a} \tag{4.67}$$

η is the dynamic viscosity, T_{lab} the lab (solvent) temperature and a is the particle radius. The particles are assumed to merely perturb the lab temperature, which is reasonable, as the energy input to the system is small relative to the standard laboratory temperature. Hence the Euler-Maruyama approximation leads to the following numerical update rule.

$$\mathbf{x}_i(t + \Delta t) = \mathbf{x}_i(t) - D_T \nabla T|_{\mathbf{x}=\mathbf{x}_i(t)} \Delta t + \sqrt{2D\Delta t}\, \eta_i \tag{4.68}$$

This is a case of over-damped dynamics, as empirical studies are at low Reynolds numbers.

4.3.1 Inter-particle Repulsion

To prevent problems with a divergent temperature field, caused by the unphysical overlap of particles and the resulting high thermophoretic velocities, the particles were also given a repulsive interaction (implemented as a velocity component), dependent only on inter-particle separation r and the illumination of the particle. As increasing illumination results in increasing particle temperature and therefore thermophoretic velocities in nearby particles.

$$\mathbf{v}_{\text{rep}}(r) = V_{\text{rep}}\hat{\mathbf{r}} = A \frac{e^{-r/\sigma}}{r^3} \hat{\mathbf{r}} \tag{4.69}$$

The inclusion of the force leads to our final version of the position update rule

$$\mathbf{x}_i(t + \Delta t) = \mathbf{x}_i(t) - D_T \nabla T|_{\mathbf{x}=\mathbf{x}_i(t)} \Delta t + \sum_{-i} V_{\text{rep}}(r)\hat{\mathbf{r}}_{ij} \Delta t + \sqrt{2D\Delta t}\eta_i \tag{4.70}$$

where the sum is over all particles other than i. However due to the computational expense of evaluating these forces (computational $O(N^2)$) for the results shown this term was omitted. Although these terms increase the physical realism of the model, by preventing collapse to an overlapping particle aggregation at the illumination focus. If a region of the parameter space is found where collapse of the aggregation to the optical focus occurs for moderate intial densities, then this may happen with the repulsive potential included as well. If this does not happen without repulsive forces it definitely won't when they are included.

4.4 Heating of 2D Particles

The model assumes that the particles are spherical but *constrained* to move in 2D. The heat equation describes how the temperature field develops over time. It has the form

$$\frac{\partial T}{\partial t} = -\kappa \nabla^2 T + \dot{Q} \tag{4.71}$$

where $T = T(\mathbf{x}, t)$ and $\dot{Q}$ is a heat source term. For the thermophoretic particles we are considering, the temperature equilibration of the system is fast relative to their speed. Hence the temperature field at each timestep can be treated as fixed and $\frac{\partial T}{\partial t} = 0$. The heat source term for a particle is

$$\dot{Q} = \frac{\gamma_j P}{\rho c V_j} \tag{4.72}$$

where γ_j is the proportion of the light from the source of power P illuminating particle j at that timestep. Particle j has a material density ρ, heat capacity c and volume $V_j = (4/3)\pi r_0^3$. Here we seek solutions of

$$\kappa \nabla^2 T = -\dot{Q} \tag{4.73}$$

Exploiting the spherical symmetry of the particle and assuming the irradiance of the particle to be conducted uniformly throughout the particle, we can express $\nabla^2 T$ in polar coordinates as a function of r alone. Here T_i is a temperature interior to the particle. See table 4.1 for definitions of constants.

$$\kappa_i \nabla^2 T_i = \kappa_i \left[\frac{1}{r} \frac{\partial}{\partial r} \left(r \frac{\partial T_i}{\partial r} \right) \right] \tag{4.74}$$

$$= \frac{1}{r} \frac{\partial T_i}{\partial r} + \frac{\partial^2 T_i}{\partial r^2} \tag{4.75}$$

Hence the steady state equation for the temperature inside a particle is given by

$$\frac{\kappa_i}{r}\frac{\partial T_i}{\partial r} + \kappa\frac{\partial^2 T_i}{\partial r^2} = -\dot{Q} \tag{4.76}$$

This is a first order linear differential equation in $\frac{\partial T_i}{\partial r}$ with general solution

$$T_i = -\frac{\dot{Q}}{4\kappa_i}r^2 - C_i \ln r + D_i \tag{4.77}$$

$C_i = 0$, as it is required that the temperature is finite at the centre of the particle and also due to circular symmetry of the temperature distribution, i.e. $\left.\frac{\partial T}{\partial r}\right|_{r=0} = 0$. D_i can be fixed by specifying a temperature at some position (although this is not necessary for the simulation as we only require the *gradient* of the temperature field). The external temperature distribution is given by the homogeneous equation

$$\frac{\kappa_o}{r}\frac{\partial T}{\partial r} + \kappa_o\frac{\partial^2 T}{\partial r^2} = 0 \tag{4.78}$$

which is again a first order linear differential equation in $\frac{\partial T}{\partial r}$, with general solution

$$T_o = -C_o \ln r + D_o \tag{4.79}$$

The thermophoretic velocity is determined by the gradient of T, so it is important to find C_o. This can be done through the flux condition at the surface of the particle, which is that the rate of heat leaving the particle and entering the environment are balanced. Fourier's law of heat conduction leads to

$$-k_i \left.\frac{\partial T_i}{\partial r}\right|_{r=r_0} = -k_f \left.\frac{\partial T_o}{\partial r}\right|_{r=r_o} \tag{4.80}$$

$$\Rightarrow \frac{k_i \dot{Q} r_0}{2\kappa_i} = k_f \frac{C_o}{r_0} \tag{4.81}$$

$$\Rightarrow C_o = \frac{k_i}{\kappa_i}\frac{r_0^2 \dot{Q}}{2k_f} \tag{4.82}$$

Note $\frac{k}{\kappa} = \rho c$. From the expression for the heat source $\dot{Q}$ we can determine C_o in terms of the elementary system variables, power of the light source and the thermal conductivity

of the solution.

$$\dot{Q} = \frac{\gamma_j P}{\rho c V_j} \tag{4.83}$$

$$= \frac{3\gamma_j P}{4\rho c\pi r^3} \tag{4.84}$$

$$\Rightarrow C_o = \frac{3\gamma_j P}{8\pi k_f r_0^2} \tag{4.85}$$

where we used $V_j = (4/3)\pi r_o^3$ for spherical particles.

4.5 Evolution of the Temperature Distribution

Next we seek to construct the full temperature field for the system as a superposition of the temperature fields induced by the individual particles. This is an approach that exploits Green's theorem for point particles which heat according to Eqn. 4.72.

The evolution of the temperature field T is given by the heat equation.

$$\frac{\partial T(\mathbf{x}, t)}{\partial t} = \kappa \nabla^2 T(\mathbf{x}, t) + f(\mathbf{x}, t) \tag{4.86}$$

Where $f(\mathbf{x}, t)$ is the function representing the heat sources in the system (the thermophoretic particles). The timescale of heat diffusion is much faster than particle diffusion allowing the temperature field at any given moment to be approximated by a steady state heat distribution (0.143×10^{-6} vs $4.94 \times 10^{-13}\,\mathrm{m^2 s^{-1}}$).

$$\frac{\partial T(\mathbf{x}, t)}{\partial t} = 0 \Rightarrow \kappa \nabla^2 T(\mathbf{x}, t) = -f(\mathbf{x}, t) \tag{4.87}$$

Dimensional analysis shows $-f(\mathbf{x}, t)$ has units of $\mathrm{Ks^{-1}}$ and must be the instantaneous change in temperature at $(\mathbf{x}, t)$. This is the source term due to light absorption by the particles.

$$\kappa \nabla^2 T(\mathbf{x}, t) = -f(\mathbf{x}, t) \tag{4.88}$$

Eqn. 4.88 is the Poisson equation and the steady state temperature is analogous to the electric field of a charge distribution given by $-f(\mathbf{x}, t)$. We can treat the particles as delta sources as, using the heating model for an individual particle in the preceding section, we have fixed the temperature field to be that of the particle it represents at that particle's radius (r_0) from the source. In the case of N point sources $f(\mathbf{x}, t)$ is a

weighted sum of delta functions.

$$f(\mathbf{x}, t) = \sum_{i=1}^{N} \delta(\mathbf{x} - \mathbf{x}_i)\dot{q}_i \tag{4.89}$$

where q_i is the source term for the point particle.

The Green's function for the Poisson equation in 2D is:

$$G(\mathbf{x}, \mathbf{x}') = \frac{-1}{2\pi \|\mathbf{x} - \mathbf{x}'\|} \tag{4.90}$$

and the solution of eqn 4.88 is the convolution with the source term.

$$
\begin{aligned}
T(\mathbf{x}, t) &= \int \frac{1}{2\pi \|\mathbf{x} - \mathbf{x}'\|} \sum_{i=1}^{N} \delta(\mathbf{x}' - \mathbf{x}_i)\dot{q}_i d\mathbf{x}' & (4.91) \\
&= \frac{1}{2\pi} \sum_{i=1}^{N} \dot{q}_i \int \frac{\delta(\mathbf{x} - \mathbf{x}_i)}{\|\mathbf{x} - \mathbf{x}'\|} d\mathbf{x}' & (4.92) \\
&= \frac{1}{2\pi} \sum_{i=1}^{N} \dot{q}_i \frac{1}{\|\mathbf{x} - \mathbf{x}_i\|} & (4.93) \\
&= \sum_{i=1}^{N} \frac{C_o}{\|\mathbf{x} - \mathbf{x}_i\|} & (4.94)
\end{aligned}
$$

Using the fact that the source term must be constant in time and neglecting the constant of integration (T_∞).

We never actually need to calculate $T(\mathbf{x}, t)$, only its gradient at the individual particle positions, for the thermophoretic velocity term in Eqn 4.70.

$$\nabla T(\mathbf{x}_i) = - \sum_{j=1, j\neq i}^{N} \frac{C_o}{r_{ij}^2} \tag{4.95}$$

When calculating the gradient vector at a particle's location, it's own contribution is not included as it is spherically symmetric and hence does not affect the vector (the contribution is also undefined due to the discontinuity at this point in the temperature distribution).

4.6 Simulations

4.6.1 Comparison with the Mean Field Model

The discreteness of the particles in the computer model introduces some differences to the continuum model. Chief amongst these differences is that the particles have a transparency of 0.0, i.e. they are fully opaque and do not reflect or scatter incoming light. This means that it is possible for the interior to be screened from the incoming light by particles further out. Whereas in the continuum model light can always reach the centre (it will however, be considerably reduced in magnitude. This may affect the density profile of the compact state. Also for investigating the compact state, the discreteness of the particles necessitates the introduction of repulsive potentials. However these potentials can affect the density of the simulations if they are too strong or far-reaching.

As previously mentioned that because no promising parameter regimes were located, the repulsive potentials were not included. This meant that the particles could overlap. The discontinuity in the temperature gradient was accounted for by switching off the interaction between 2 particles once they h d overlapped.

4.6.2 Parameters

For explanantions of the dimensional variables in the simulation see table 4.1. The convenient dimensionless quantities arising from the continuum model are defined as follows:

$$\bar{R} = \frac{R}{2r_0 N} \tag{4.96}$$

$$\bar{\psi} = 2r_0 \int_0^R \rho \, dr \tag{4.97}$$

$$\bar{\gamma} = \frac{-D_T P}{\pi k_f D} \tag{4.98}$$

$\bar{R}$ is a dimensionless system size. $\bar{\psi}$ represents the average number of particles between the focus and the boundary contained within a tube of width $2r_0$ and hence is a dimensionless measure of the opacity, i.e. the collection of particels is transparent if $\bar{\psi} \ll 1$, opaque if $\bar{\psi} > 1$ and marginally opaque if $\bar{\psi} \simeq 1$. $\bar{\gamma}$ is a compound variable representing the strength of the thermophoretic interaction relative to the thermal diffusion, dependent upon the energy input through P For physical parameters of the particles refer to values for $500\,\text{nm}$ polystyrene beads in Haynes [2014].

Table 4.1: Parameters used in the 2D simulations.

Parameters	Value	Units
T	298	K
r_0	500	nm
D_T	6.0x10^{-12}	$\mathrm{m^2\,s^{-1}\,K^{-1}}$
D	4.94×10^{-13}	$\mathrm{m^2\,s^{-1}}$
η	8.9×10^{-4}	$\mathrm{kg\,m^{-1}s^{-1}}$
k_f	0.609	$\mathrm{W\,m^{-1}\,K^{-1}}$ [1]
P	0.938	W
A	4.15x10^{-18}	$\mathrm{m\,s^{-1}}$
σ	3.0	r_0
r_max	0.5	r_0

4.6.3 Timesteps

The time discretisation of the numerical Langevin equation leads to a sensitivity to timestep size. If timesteps are too large, then the velocities calculated can be so large as to cause overlaps or particles 'leapfrogging' other particles. If two particles overlap the forces generated at the next timestep can be large enough to move them unphysically large distances (and even ejected from the system). It is therefore necessary to have timesteps small enough that the repulsive and thermophoretic forces between particles will be felt before overlapping occurs.

However, in a diffuse state the interparticle separations will be larger than the length scale of the repulsive potential and very small timesteps will prevent efficient simulation. The obstacle to using standard adaptive time stepping is that the need to avoid these overlaps and the extreme consequences of the singularities in the temperature gradient field (and therefore the induced thermophoretic velocities) results in the timesteps becoming infeasibly small (in compact states). So an adaptive timestepping scheme was implemented that ensured that no particle could move more than a prescribed distance r_max in any given timestep. The timestep length being recomputed from the velocities after each step. The constraint on r_max is implemented as follows:

$$\left|(\mathbf{v}^i_\mathrm{the} + \mathbf{v}^i_\mathrm{rep})\tau + \Delta\mathbf{x}^i_D\right| \leq r_\mathrm{max}, \forall \tag{4.99}$$

where τ is the length of the timestep and $\Delta\mathbf{x}^i_D$ is the thermal noise contribution to the

particle displacement and is consequently proportional to $\sqrt{\tau}$.

$$\left| \begin{pmatrix} V_L^x \\ V_L^y \end{pmatrix} \tau + \begin{pmatrix} \xi^x \\ \xi^y \end{pmatrix} \sqrt{2D\tau} \right| \leq r_{\max} \tag{4.100}$$

$$\Rightarrow |\mathbf{v}_L|^2 \tau^2 + 2D|\xi|^2 \tau + 2\sqrt{2D}(\mathbf{v}_L \cdot \xi)\tau^{3/2} \leq r_{\max}^2 \tag{4.101}$$

This is a quartic equation in $y = \tau^{1/2}$ and can be solved numerically at equality. The Jenkin-Traub algorithm is used to solve the equation in this simulation to yield $\tau_{\max}^i$, the timestep that allows the particle to move distance $r_{\max}$. The shortest of these over all particles is selected to yield $\tau_{\max}$, the longest timestep that guarantees all particle moves are less than $r_{\max}$ and that is the new timestep. $r_{\max}$ has been selected to be $r_0/2$, which is 1/8th the typical particle surface-surface separation, as calculated from the continuum model (see §4.8.1). To prevent particles overlapping and the consequential blow-up in the thermophoretic force between them, due to the singularity in the derivative of temperature field at the particle origin, it is necessary to introduce a repulsive potential. Otherwise as 2 particle centres approach the thermophoretic velocity of each particle increases to infinity.

A soft potential is used as this will not require the very small steps of a hard potential. The small steps are required as the forces generated can be large if the particles overlap too much. There is of course the issue of how to set the length scale and strength of the repulsive potential. This procedure was implemented mostly with regards to the inclusion of the repulsion term. Despite the repulsions being removed for the initial investigations this procedure was still followed as step size is still a concern.

4.7 Results

The aim was to find evidence for the proposed transition from a diffuse state to a highly compact state. The compact state's existence was predicted to depend on a sufficiently dense initial conditions and sufficiently high influx of energy into the system.

Initial attempts were made to find the predicted transition using $N = 1000$ particles and repulsive forces to prevent overlaps. However, the long simulation times required, made it difficult to find a region of the parameter space containing a transition from a diffuse to a compact state (as it did not seem to be in the predicted region). To ease the computational burden, the repulsive forces were discarded and N reduced from 1000 to 500. This allowed the particles to pass through each other in a similar way to the 'phantom' particles in previous chapters.
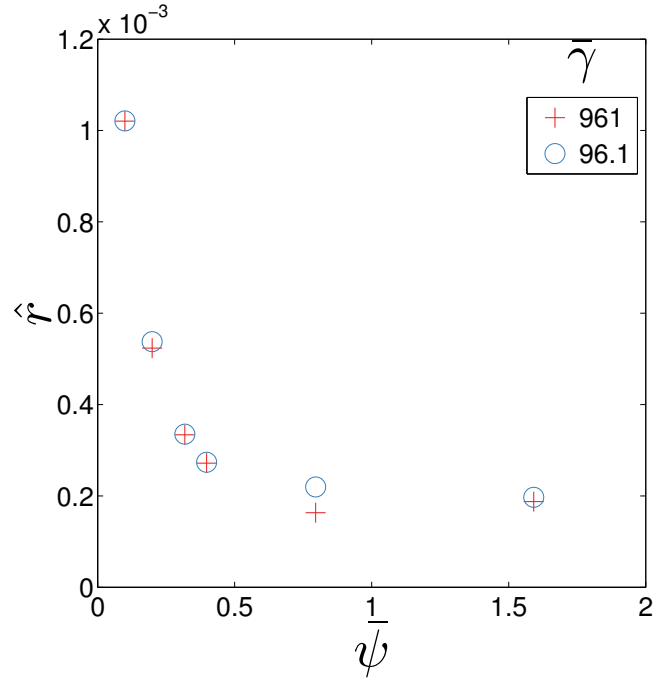
Figure 4.5: Simulation evidence for the transition: Using $N = 500$ particles and $\bar{R} = 3$. $\hat{r}$ is the mean particle distance from the origin and focus. The particles were prepared in states with initial $\bar{\psi}_{t=0}$ given in the figure. The thermophoretic response/energy input into the system is given by $\bar{\gamma}$ in the inset. The simulations were then allowed to reach a steady state (not a true steady state as particles are lost from the aggregation by diffusion, but it is long-lived relative to the individual particle diffusion times). There does appear to be a continuous transition between a diffuse state at low initial density (proxy is $\bar{\psi}$) and a compact state at high initial density, with $\bar{r} \approx 2 \times 10^{-4}$.

Evidence for the transition was found by holding $\bar{\gamma}$ constant and using the initial density as a control parameter and proxy for $\bar{\psi}_{t=0}$ (see Fig. 4.5). The simulated times were between 14322 and 50286 s, which represent millions of simulation timesteps (due to the small $\Delta\mathbf{x}$ moves). It should be noted that particles are gradually lost from the compact mass around the focus, by chance fluctuations. This provides evidence for instability of the compact mass, as the rate of particle loss is greater than that of gain. Hence the radial mean increases over large timescales and is *not* stationary and values will depend on when the measurement occurred.

4.8 Setting the Repulsion

Note this repulsive potential is to be used in future work and was not used in the results in the preceding section. The importance of the repulsive potential is that it prevents unphysically compact particle aggregations from overlapping particles and prevents particles overlapping and the consequential blow-up in the thermophoretic force between them, due to the singularity in the temperature field at the particle origin. A soft potential is used as this will not require the very small steps of a hard potential (computational time for the preceding simulations is already an issue without calculating a repulsive interaction). The small steps are required as the forces generated can be large if the particles overlap too much. There is of course the issue of how to set the lengthscale and strength of the repulsive potential.

4.8.1 Setting the Lengthscale of Repulsion

First we shall determine the mean particle separation in a compact state and ensure that the length scale for the repulsion σ is small compared to this distance. So that the repulsion does not affect the steady state density of the system. If we take the central density of the compact state in the mean field continuum model. A value for the typical distance between particle centres can be estimated as

$$\lambda_d = \frac{1}{\sqrt{\rho_0}} \tag{4.102}$$

From examination of how the central densities vary with the dimensionless parameters, it can be seen that λ_d has a lower bound when $\bar{\gamma} < 10$:

$$\lambda_d \geq 2r_0 \, \frac{\sqrt{N}}{10} \tag{4.103}$$

There is a square root dependence on N and clearly small values of N will have small distances and N must be greater than 25 before the typical distance is greater than 1 particle radius and 100 before it is greater than 2 radii. At a 2 radii distance the particles are all touching and clearly this will be difficult to simulate due to timestepping demands, whereas below this the particles overlap unphysically (see fig. 4.6). Clearly in the preceding simulations $\bar{\gamma} > 10$ were used, this was so that the interparticle separations were larger and hence the average time step in the simulation. $N = 1000$ gives $\lambda_d = 6.3r_0$ and a separation between surfaces of $4.3r_0$ or approximately 2 particle diameters. This is an acceptable particle separation for simulation purposes (remember the effect of
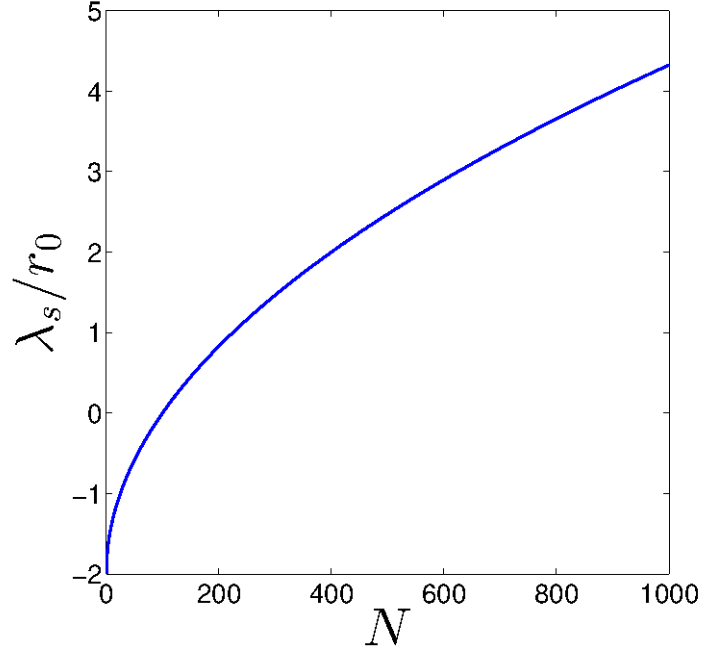
Figure 4.6: The variation in typical particle separation λ_s with N for $\bar{\gamma} < 10$.

interparticle separation on time step size through Eqn 4.99). Another approach is to compute the 2D Wigner-Seitz radius, r_{ws}. That is the radius of a circle of area equal to the mean area per particle. This gives an approximate length scale for the interactions and assumes a uniform density.

$$\pi r_{ws}^2 = \frac{\pi R^2}{N} \tag{4.104}$$

$$r_{ws} = \sqrt{\frac{R^2}{N}} \tag{4.105}$$

For $N = 1000$, $r_{ws} = 6.7r_0$, leading to an approximate λ_s of $4.7r_0$ or, again, just over 2 particle diameters surface to surface. It is clear from these two approaches that the length scale of the repulsion σ must be smaller than $6r_0$ (as the repulsion is from the particle centre), but greater than r_0 so that it is outside the particle. A σ of $4.0r_0$ was selected for the simulations as the repulsion length scale as it represents an interparticle surface-surface separation of $2r_0$ or 1 particle diameter.

Strength of Repulsion

Now the length scale for the repulsion has been fixed, it is necessary to determine the required strength of the repulsion. Diffusion makes the largest contribution to the particles velocities and it therefore seems reasonable to use diffusion as a constraint on the magnitude of the repulsive force. It is required that the maximum diffusive displacement is balanced by the repulsive potential at a separation distance of $3r_0$ from the centres of the particles. The minimum time it takes a particle to diffuse $r_{\max}$ is $\tau_{D,min} = r_{\max}^2/4D$. This is the shortest time it takes for a particle to be displaced distance $r_{\max}$ by diffusion alone. Hence an expression for the amplitude of the repulsive potential can be determined.

$$\mathbf{V}_{rep}(r = 3r_0)\tau_{D,min} \quad = \quad r_{\max} \tag{4.106}$$

$$A\frac{e^{-\frac{3}{4}}}{(3r_0 - 2r_0)^3}\tau \quad = \quad r_{\max} \tag{4.107}$$

$$\Rightarrow A \quad = \quad \frac{4De^{3/4}r_0^2}{r_{\max}} \tag{4.108}$$

The Initial $\bar{\psi}$

The particle positions are initiated in a square grid, such that all particles are within a given radius. For a given initial $\bar{\psi}$ an estimate for the required radius, R' is made based on the area fraction ϕ occupied by the particles positioned within that radius. This is an attempt at a discrete analogue of $\bar{\psi}$ and assumes a constant area fraction within the initial particle grouping. The continuum $\bar{\psi}$ represents the number of particles seen in a tube of width $2r_0$ from the radius to the edge of the system (radius of the system in dimensional units, R'). The occupied volume fraction is $\phi = \frac{Nr_0^2}{R'^2}$. Hence the estimated number of particles seen in a tube of width $2r_0$ and length R' is:

$$\bar{\psi}_{\text{est}} \quad = \quad \frac{2\phi r_0 R'}{\pi r_0^2} \tag{4.109}$$

$$= \quad \frac{2Nr_0}{\pi R'} \tag{4.110}$$

where we have divided the area containing particles by the particle area.

Simulation Times

It is necessary to simulate a sufficiently long time that the system can reach a steady state, if it exists. An estimate for this time can be obtained from the assumption that

diffusion is dominant. A sufficient time to reach steady state is then $\tau_{\text{eq}} = \frac{r_c}{D}$, where r_c is the critical distance. The critical distance should be long enough that any particle in a compact state should (on average) be able to reach any position in the marginally opaque state. This allows the particles to relax to steady positions in the marginally opaque state from the initial compact state. So an estimate of the width of the distribution in that state is required. For $\bar{\gamma} = 8$, $\bar{\psi}$ in the compact state is ≈ 2.4 Hence $R' = r_c \approx 0.00013\,\text{m}$ for our system and $\tau_{\text{eq}} \approx 3.5 \times 10^4\,\text{s}$.

4.8.2 Illumination Algorithm

The most algorithmically challenging part of the model is calculating the fraction of total irradiance falling on each particle.

    The strategy taken was to place a fictitious particle at the centre of the domain and then to sequentially add the real particles from the furthest to the nearest. After each particle addition the irradiance of the fictitious particle was calculated (in the same way as the projected views were, for flock members in the preceding chapters). The difference between the previous irradiance for particle $i - 1$ and the new irradiance is the light absorbed by the ith particle. This is obvious for the first particle, when the previous irradiance is the full irradiance. See Fig. 4.7. The angular size (θ) of the
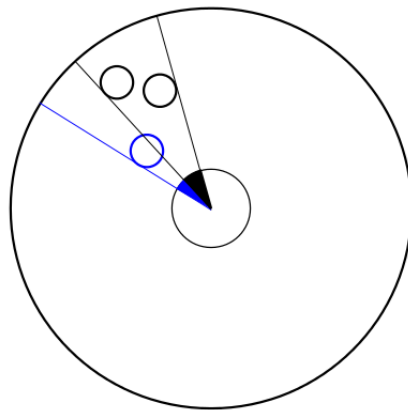
Figure 4.7: The incoming irradiance absorbed by each particle is calculated using the shadows cast onto a fictious particle at the origin. The particles are added from the furthest to the focus, to the nearest. Such that the difference in the area shadowed on the fictious particle after each particle is added, is the proportion of incoming light absorbed by that particle.

shadow of a particle onto the fictitious particle is $2\arcsin(r_0/r)$, where r is the distance
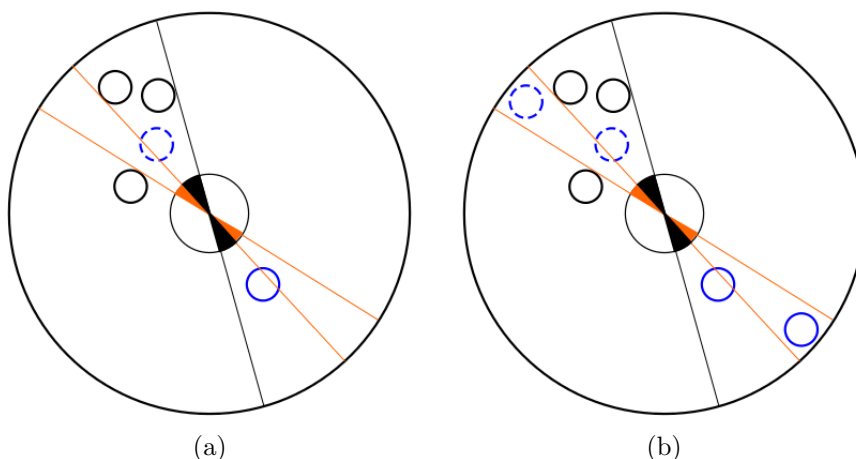
(a)   (b)

Figure 4.8: Similarly to the case for incoming light, the proportion of outgoing light absorbed by each particle is calculated sequentially from nearest to the focus outwards. Light in the orange corridor must pass through to the focus, before it can reach the underside of a particle. Hence if we continue the shadowing algorithm used for inwards light (black particles are from previous step), but now adding the inverted positions (dashed) we calculate the outwards illumination caught by the two blue particles. Note the light that illuminates their undersides must have missed the black particles.

from the origin to the particle. Illumination is isotropic and directed towards the focus (optical centre).

A subtlety is that if there is no particle at the focus, then light can pass through the focus and illuminate the side of the particles nearest to the focus (let's call this the underside). Now that all the particles have been added from furthest to nearest, we repeat the process adding the particles from the nearest to the furthest (keeping those previously added in the incoming irradiance calculation), but reflecting the particles through the focus (as an inversion centre). This works because light irradiating the underside must have passed though the inversion centre (irradiance focus) to reach the particle's underside. Following this procedure, we obtain the fraction of the total irradiance (incoming and outgoing) light absorbed by each particle. See Fig. 4.8.

The only other problem to consider, is what to do if one or more particles overlap the focus. It was chosen that if one particle overlaps the focus, then it absorbs all the incident light. In reality there would be reflection and scattering so this could be a drastic approximation. If more than one particle overlaps the focus, the decision was made to split the irradiance equally between the overlapping particles, as the projection algorithm cannot handle overlap of particles and focus. It should be noted that if a particle or particles are at the focus then there is no outgoing irradiance and the computational

work is halved for the illumination algorithm.

Algorithm 1 Calculating Particle Irradiance: i labels particles ordered by increasing distance from optical focus. Ω stores value of shading on the imaginary particle by the others.

$O \leftarrow$ initialise view {Imaginary particle at the centre of mass of particles.}
for $i = 0$ **to** $N - 1$ **do**
   add projection of i to view of O.
   $\Omega[i] \leftarrow \omega$ {ω is the area of O shadowed by i.}
end for
for $i = N - 1$ **to** 0 **do**
   add projection of i at $-\mathbf{x}_i$ to O.
   $\Omega[2N - 1 + i] \leftarrow \omega$
end for
$I[0] \leftarrow \omega[0]$ {I is particle illumnation}
for $i = 1$ **to** $N - 1$ **do**
   $I[i] \leftarrow \omega\ [i]$-$\omega[i - 1]$
end for
for $i = N - 1$ **to** $2N - 1$ **do**
   $I[i] \leftarrow I[i] + \omega[0] - \omega[i - 1]$ {I is particle illumnation}
   $I[i] \leftarrow \frac{I[i]}{4\pi r^2}$ {r is the radius of the imaginary particle.}
end for

4.9 Conclusion

The results displayed in Fig. 4.5 demonstrate a transition in the compactness of the particles, as measured by $\hat{r}$ the mean focus-particle distance, as $\bar{\psi}_{t=0}$ increases. This is for simulations *without* an included repulsion term, hence the density of the compact state will not correspond with experimental values as the particles can pass through each other. However in the mean field theory the simulation was meant to emulate has no equivalent constraint. The details of working with simulated particles, rather than the mean field theory introduces tunable parameters, such as timesteps and particle sizes. Also the mean field theory has a particle density with a given transparency and the simulation model has discrete particles with discrete shadowing of each other. These differences between the models may explain why the transition to a compact state was only found using much higher values of $\hat{\gamma}$ than expected from the mean field theory.

4.10 Future Work

- The assumption of instantaneous temperature equilibration across the domain of the simulation could be relaxed, if the domain was discretised and the heat allowed to flow between the discretised volumes (this can be done very efficiently on a graphics card). It was not made clear initially that the domain in the analytic work had a fixed boundary and hence this was not implemented.

- A further refinement would be to include self-thermophoresis, perhaps by discretising the boundary for each particle and allowing differential heating between the regions, based on the surface illumination.

- A model of self-thermophoresing particles by Cohen [2013] uses uses a spherical harmonic expansion of each particle's anisotropic temperature field caused by surface-illumination. This method could be generalised from a single source of (linear) illumination, to include multiple light sources and reflections from the particle surfaces. A framework exists in the from of spherical harmonic models of lighting in computer graphics. These calculations can be highly parallelised on a graphics card and would be considerably faster than current approaches, with the potential for tens of thousands of particles with a more accurate illumination (and higher order approximations to the temperature field) using the same spherical harmonic integration code.

Chapter 5

Conclusions

> This is the way the world ends
> This is the way the world ends
> This is the way the world ends
> Not with a bang but a whimper.
>
> ――――――――――――――――――――――――
> T. S. Eliot – *The Hollow Men*

A series of agent-based particle models were created of both animal collective motion and thermophoretic collective motion in 2D and 3D. These models relied on projections of shadows onto the surface of the spherical agents. The projections in 2D were calculated using a very simple algorithm, using interval arithmetic.

The main thread of this thesis that binds it together, is the consideration of light sources and how they shadow circular or spherical particles that respond in some way to the results of this shadowing. In the case of the flocking models movement rules are based directly on the shadowing and illumination of the particles. In the thermophoretic models the heating of the particles is controlled by their shading of each other relative to the optical focus of the system and the particles respond to this through the induced temperature field.

The projections in 3D lead to more difficult computational geometry than the 2D cases, thus requiring more software development time. The resulting algorithm did not have the best known computational complexity $\mathbb{O}(N \log N)$, but was instead $\mathbb{O}(N^2)$. However the algorithm was considerably more robust and faster, as it could be implemented in double arithmetic as opposed to high-precision or exact[1] numerical arithmetic. For the case of 3D bird flocking, the mean view area occluded or opacity, Ω, was an im-

――――――――――――――――――――――――

[1] This is typically through a restriction to rational coordinates and certain geometrical constructions that can be represented in these.

portant measure for comparison with empirical data and hence efficiently calculating the occluded surface area on a sphere was important. An alternative approach would have been to measure less often, but that is not possible when trying to work out correlation times (if you wait too long between samples you may not see a short time correlation and the precision to which you can estimate correlation times is limited by your sampling rate). The surface area integration was achieved through an approximate Green's function approach and it's robustness relies on the arc-finding projection algorithm. The two algorithms were tested together and found to give errors of less than 1% in the test cases compared to the point-wise estimate.

In chapter 2 on 3D animal collective motion (particularly starlings), a simulation model was developed, based on the previous 2D model that reproduces qualitative features of bird flocks such as alignment and cohesion, which is not in itself impressive as many models do that. However, it was found that the opacity scaled with flock size (as measured by $r_{\max}$) in the same way in the model as in the empirically observed starling flocks. Anisotropy in the nearest neighbour distributions very similar to that of the empirical flocks was observed for a set of model parameters. An unexpected anisotropy in the model flock dimensions (leading to relatively flat flocks) was another feature of the model, with similarities to the natural flocks. However in the case of flock dimensions the extension along the axes is different to natural flocks, which is probably due to natural flocks having a special direction for alignment other than the average flock velocity, i.e. the direction defined by gravity. These features are emergent from the visual flocking rules and are not known from other Vicsek-type flocking models. These particular comparisons can only be directly compared with natural flocks in a 3D simulation and hence justifies the effort in creating one for this model.

Chapter 3 developed 2D models of animal collective motion. A different set of models based on an alternative visual paradigm, that of optical flow, were developed. Agent-based simulations derived from the optical flow paradigm are novel models of flocking interactions. These models were designed to correspond to thinking in biology and psychology about how visual perception works, which is in itself an unusual approach. Some features such as rotational motion arise from the directional memory inherent in the rules. This is using isotropic agents, whereas for the 2D version of the model of Pearce et al. [2014] rotational motion was induced with anisotropic agents.

Chapter 4 sought simulation evidence for a predicted transition between a compact state held together by temperature gradients induced by the particles absorbing laser light. Evidence for this transition was found at higher input light energies than predicted from the mean field theory, which is likely because of the discrete nature of the

particle shading in the model and lack of particle transparency compared to the mean field density model.[2]
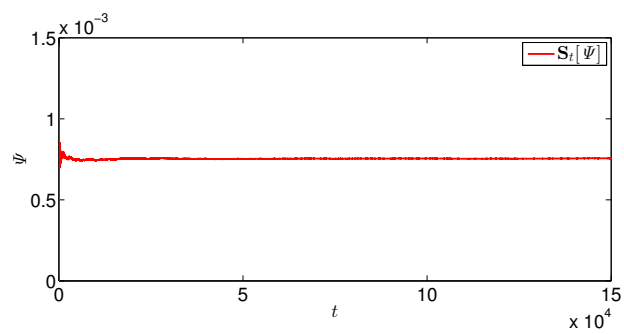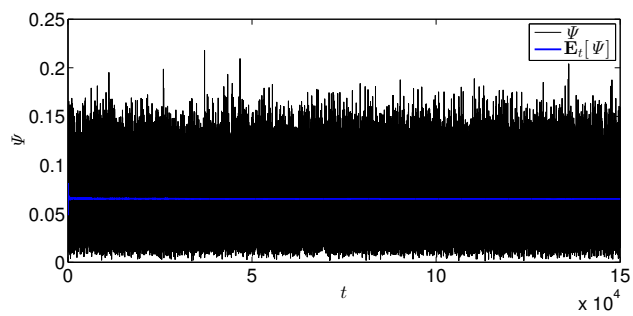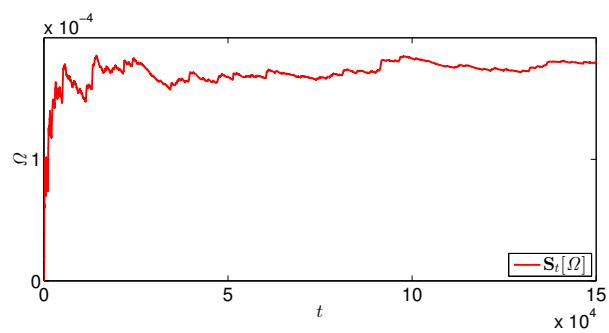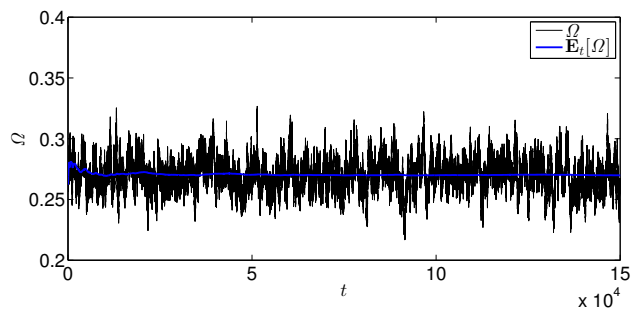
---

[2]So long, and thanks for all the fish.

Appendix A

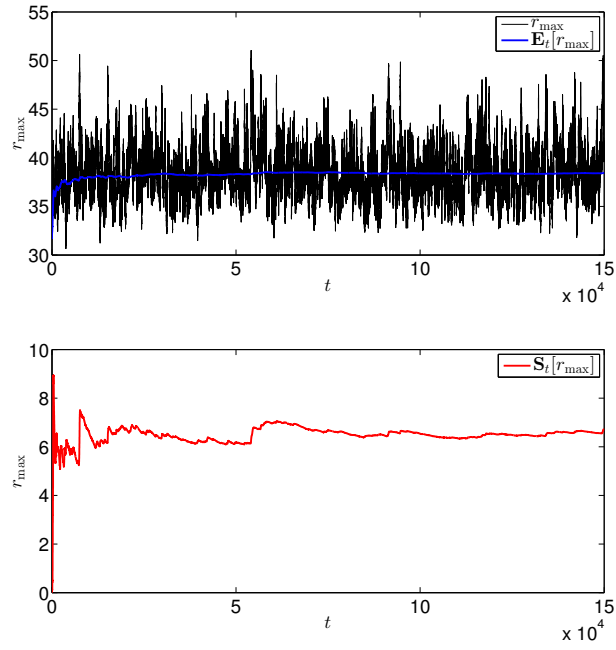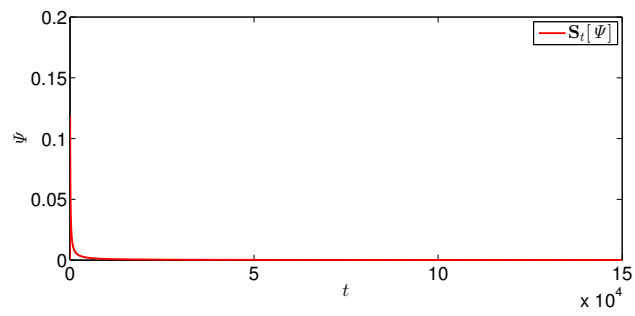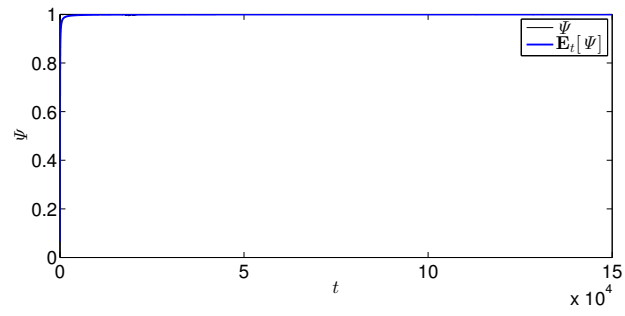# 3D Flock Order Parameter Traces
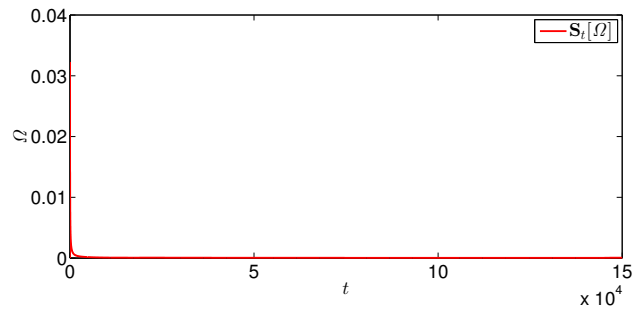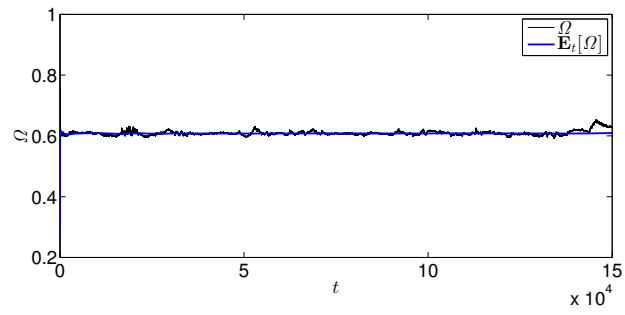
$$\vec{\phi} = (0.0, 0.1, 0.9)$$

Figure A.1: Opacity Ω, velocity order parameter Ψ and flock size r_{max} time traces with running means and variance for an $N = 200$ flock with parameters given in the figure.
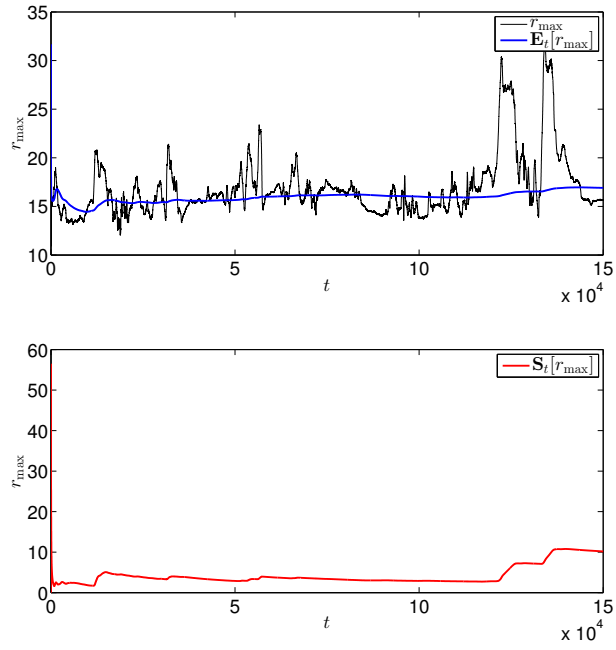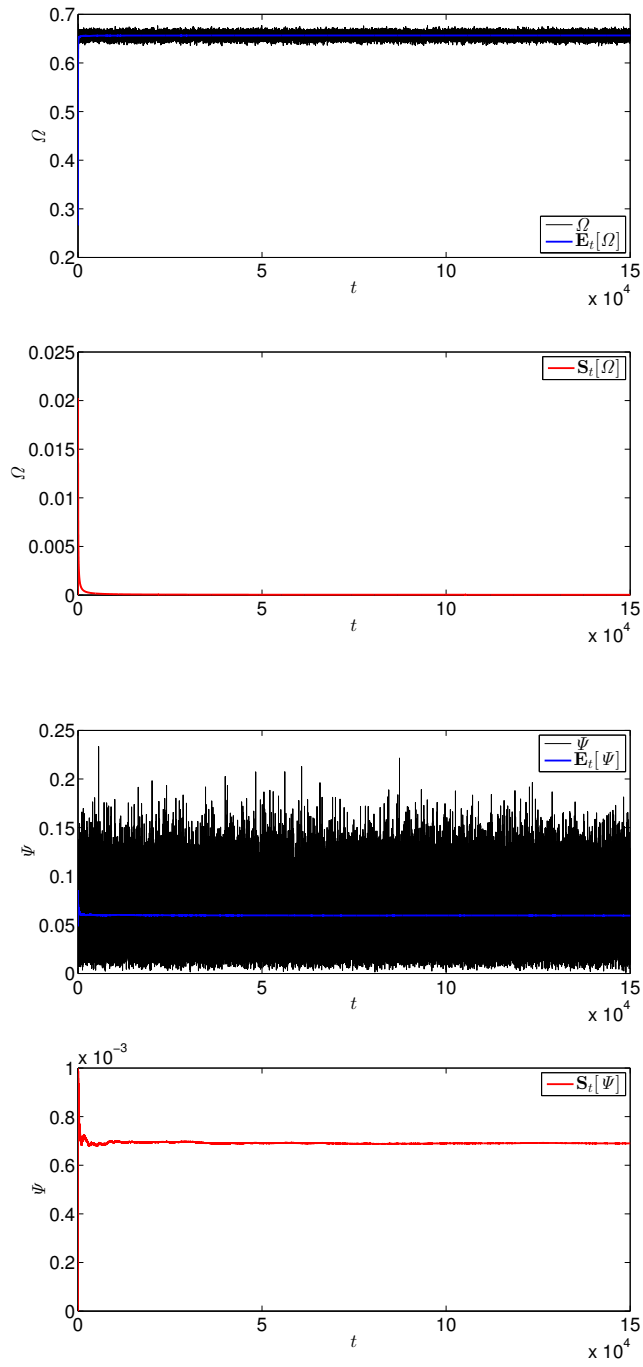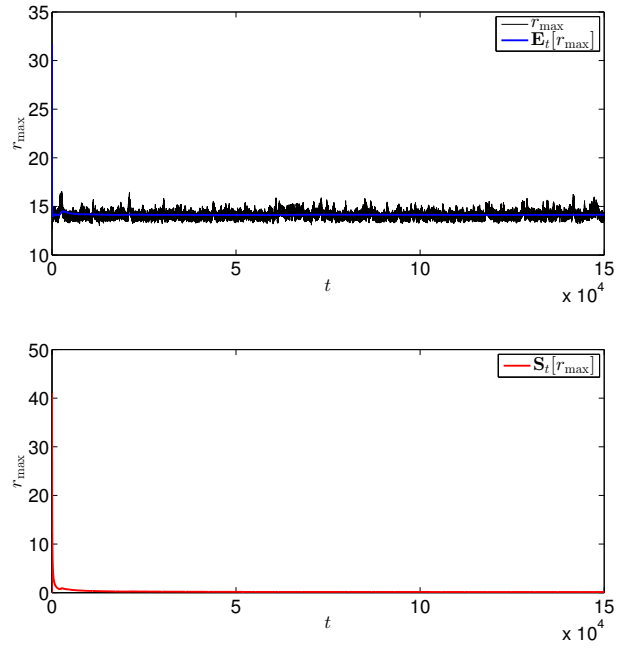
$$\vec{\phi} = (0.495, 0.495, 0.01)$$

Figure A.2: Opacity Ω, velocity order parameter Ψ and flock size $r_{\max}$ time traces with running means and variance for an $N = 200$ flock with parameters given in the figure.
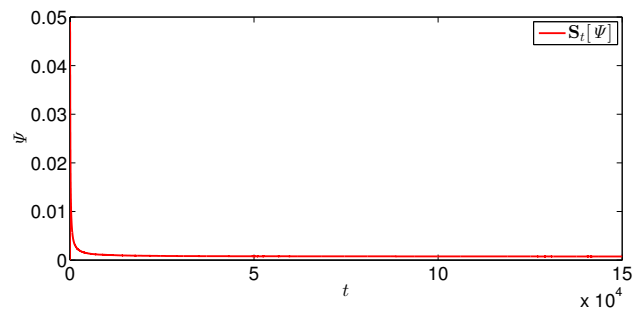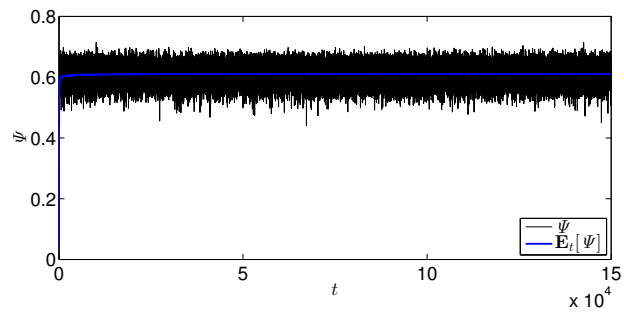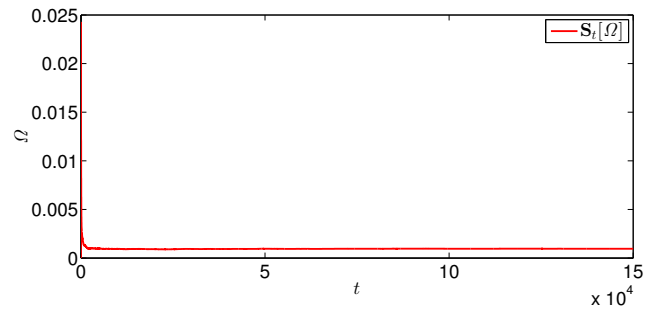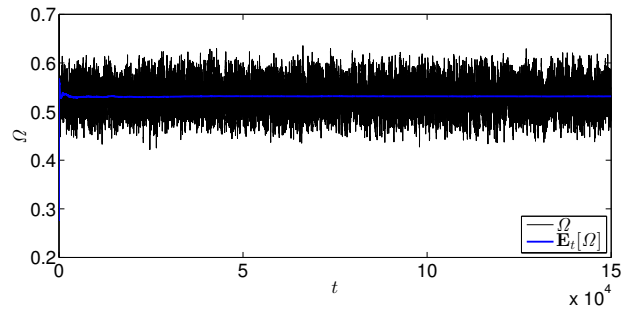
$$\vec{\phi} = (0.0, 0.9, 0.1)$$

145

Figure A.3: Opacity Ω, velocity order parameter Ψ and flock size $r_{\max}$time traces with running means and variance for an $N = 200$ flock with parameters given in the figure.

$$\vec{\phi} = (0.333, 0.333, 0.333)$$
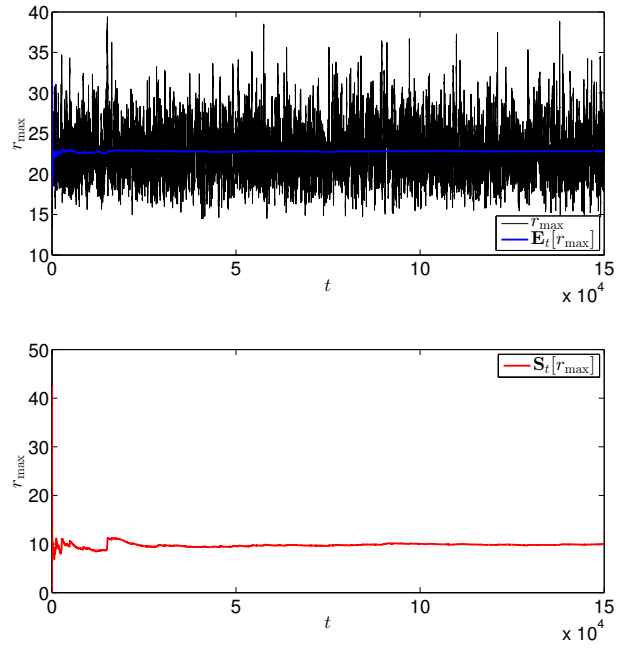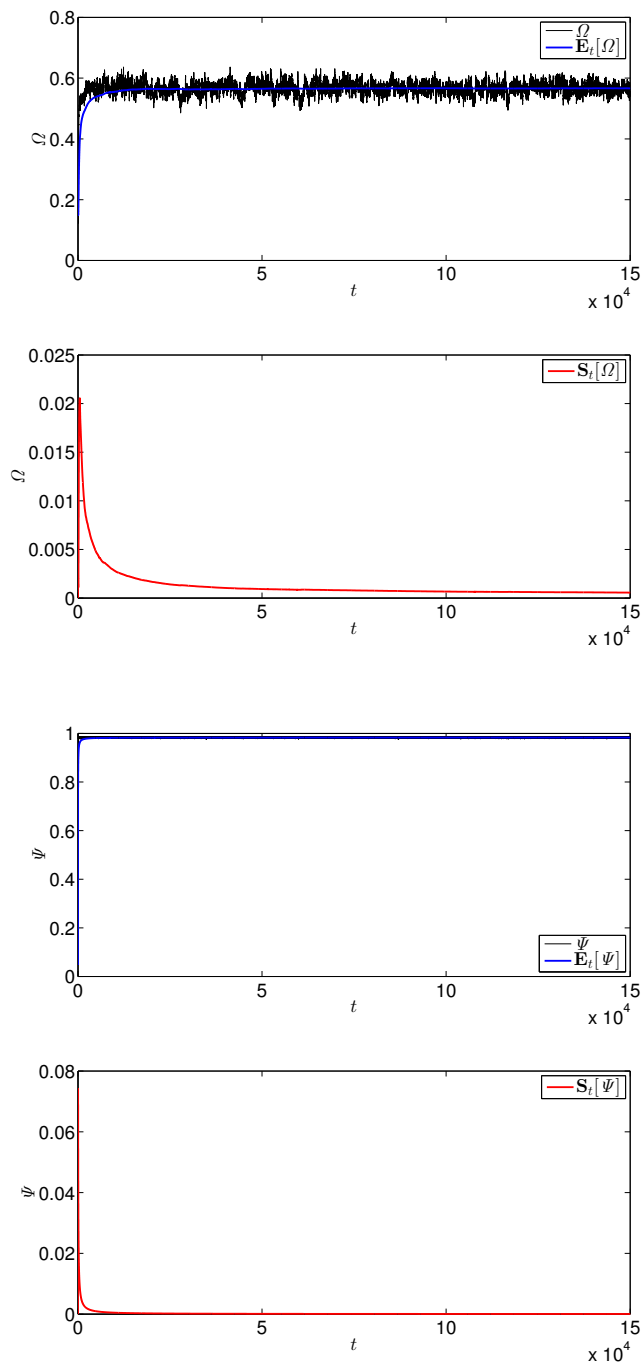
147

Figure A.4: Opacity Ω, velocity order parameter Ψ and flock size r_{max} time traces with running means and variance for an $N = 200$ flock with parameters given in the figure.
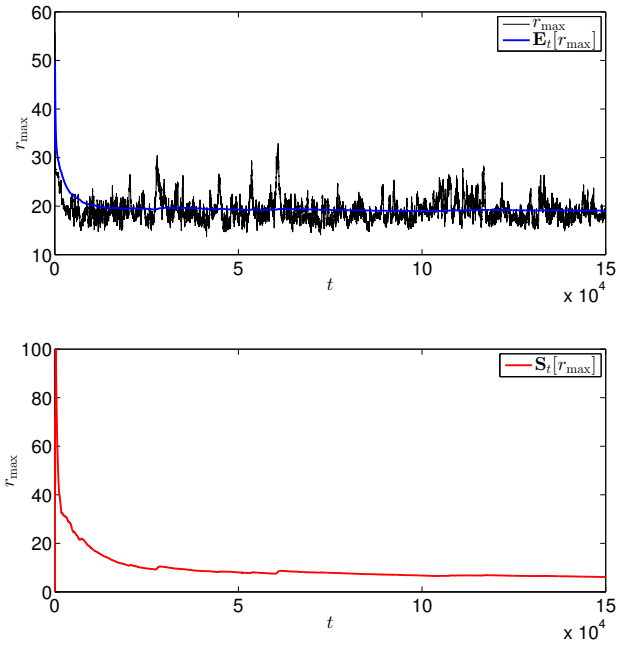
$$\vec{\phi} = (0.8, 0.03, 0.17)$$

Figure A.5: Opacity Ω, velocity order parameter Ψ and flock size r_{max} time traces with running means and variance for an $N = 200$ flock with parameters given in the figure.

Bibliography

John P. Badgerow and F.Reed Hainsworth. Energy savings through formation flight? a re-examination of the vee formation. *Journal of Theoretical Biology*, 93(1):41 – 52, 1981. ISSN 0022-5193. doi: http://dx.doi.org/10.1016/0022-5193(81)90055-2. URL `http://www.sciencedirect.com/science/article/pii/0022519381900552`.

Iztok Lebar Bajec and Frank H. Heppner. Organized flight in birds. *Animal Behaviour*, 78(4):777–789, 2009. ISSN 0003-3472. doi: http://dx.doi.org/10.1016/j.anbehav.2009.07.007. URL `http://www.sciencedirect.com/science/article/pii/S0003347209002966`.

M. Ballerini, N. Cabibbo, R. Candelier, A. Cavagna, E. Cisbani, I. Giardina, V. Lecomte and A. Orlandi, G. Parisi, A. Procaccini, M. Viale, and V. Zdravkovic. Interaction ruling animal collective behavior depends on topological rather than metric distance: Evidence from a field study. *PNAS*, 105(4):1232–1237, 2008a.

Michele Ballerini, Nicola Cabibbo, Raphael Candelier, Andrea Cavagna, Evaristo Cisbani, Irene Giardina, Alberto Orlandi, Giorgio Parisi, Andrea Procaccini, Massimiliano Viale, and Vladimir Zdravkovic. Empirical investigation of starling flocks: a benchmark study in collective animal behaviour. *Animal Behaviour*, 76(1):201 – 215, 2008b. ISSN 0003-3472. doi: http://dx.doi.org/10.1016/j.anbehav.2008.02.004. URL `http://www.sciencedirect.com/science/article/pii/S0003347208001176`.

J. Buhl, D. J. T. Sumpter, I. D. Couzin, J. J. Hale, E. Despland, E. R. Miller, and S. J. Simpson. From disorder to order in marching locusts. *Science*, 312:1402–1406, 2006. doi: 10.1126/science.1125142.

A Cavagna, Giardina, Orlandi I, Parisi A, and Procaccini G. The starflag handbook on collective animal behaviour. 2: three- dimensional analysis. *Animal Behavior*, 76: 237–248, 2008a.

A Cavagna, I Giardina, A Orlandi, G Parisi, A Procaccini, M Viale, and V Zdravkovic. The starflag handbook on collective animal behaviour. 1: empirical methods. *Animal Behavior*, 76:217–236, 2008b.

A. Cavagna, L. Del Castello, S. Dey, I. Giardina, S. Melillo, L. Parisi, and M. Viale. Short-range interaction vs long-range correlation in bird flocks. *ArXiv e-prints*, July 2014.

Andrea Cavagna and Irene Giardina. The seventh starling. *Significance*, 5(2):62–66, 2008. ISSN 1740-9713. doi: 10.1111/j.1740-9713.2008.00288.x. URL `http://dx.doi.org/10.1111/j.1740-9713.2008.00288.x`.

Andrea Cavagna, Alessio Cimarelli, Irene Giardina, Giorgio Parisi, Raffaele Santagati, Fabio Stefanini, and Massimiliano Viale. Scale-free correlations in starling flocks. *Proceedings of the National Academy of Sciences*, 107(26):11865–11870, 2010. doi: 10.1073/pnas.1005766107. URL `http://www.pnas.org/content/107/26/11865.abstract`.

Robert G. Chamberlain and William H. Duquette. Some algorithms for polygons on a sphere. Technical Report JPL Publication 07-3, NASA, JPL, California Institue of Technology, Pasadena California, June 2007.

Jack Andrew Cohen. *Active colloids and polymer translocation.* PhD thesis, Mathematical,Physical & Life Sciences Division - Physics - Condensed Matter Physics, Oxford University, 7 2013.

Iain D. Couzin and Mark E. Laidre. Fissionfusion populations. *Current Biology*, 19(15):R633 – R635, 2009. ISSN 0960-9822. doi: http://dx.doi.org/10.1016/j.cub.2009.05.034. URL `http://www.sciencedirect.com/science/article/pii/S0960982209011695`.

Iain D. Couzin, Jens Krause, Richard James, Graeme D. Ruxton, and Nigel R. Franks. Collective memory and spatial sorting in animal groups. *Journal of Theoretical Biology*, 218(1):1 – 11, 2002. ISSN 0022-5193. doi: http://dx.doi.org/10.1006/jtbi.2002.3065. URL `http://www.sciencedirect.com/science/article/pii/S0022519302930651`.

Tran Kai Frank Da and Mariette Yvinec. 3D alpha shapes. In *CGAL User and Reference Manual.* CGAL Editorial Board, 4.5 edition, 2014. URL `http://doc.cgal.org/4.5/Manual/packages.html#PkgAlphaShapes3Summary`.

B Dawes. Boost c++ libraries. `http://www.boost.org`, 2003. URL `http://www.boost.org`.

Christian F. Doeller, Caswell Barry, and Neil Burgess. Evidence for grid cells in a human memory network. *Nature*, 463:657–661, 2010. doi: http://dx.doi.org/10.1038/nature08704.

Stefan Duhr and Dieter Braun. Why molecules move along a temperature gradient. *Proceedings of the National Academy of Sciences*, 103(52):19678–19682, 2006.

Herbert Edelsbrunner and Ernst P. Mücke. Three-dimensional alpha shapes. *ACM Trans. Graph.*, 13(1):43–72, January 1994. ISSN 0730-0301. doi: 10.1145/174462.156635. URL `http://doi.acm.org/10.1145/174462.156635`.

Jolyon J. Faria, John R. G. Dyer, Romain O. Clément, Iain D. Couzin, Natalie Holt, Ashley J. W. Ward, Dean Waters, and Jens Krause. A novel method for investigating the collective behaviour of fish: introducing robofish. *Behavioral Ecology and Sociobiology*, 64(8):1211–1218, 2010. ISSN 0340-5443. doi: 10.1007/s00265-010-0988-y. URL `http://dx.doi.org/10.1007/s00265-010-0988-y`.

Esteban Fern'andez-Juricic. Sensory basis of vigilance behavior in birds: Synthesis and future prospects. *Behavioural Processes*, 89:143–152, 2012.

M Galassi, J Davies, J Theiler, B Gough, G Jungman, P Allen, M Booth, F Rossi, and R Ulerich. *GNU Scientific Library Reference Manual (3rd Ed.)*. Network Theory Limited, 2009.

Mimi M. Ghim and William Hodos. Spatial contrast sensitivity of birds. *Journal of Comparative Physiology A*, 192(5):523–534, 2006. ISSN 0340-7594. doi: 10.1007/s00359-005-0090-5. URL `http://dx.doi.org/10.1007/s00359-005-0090-5`.

I. Giardina. Collective behavior in animal groups: theoretical models and empirical studies. *HFSP J*, 2(4):205–219, Aug 2008.

James J Gibson. *The Ecological Approach To visual Perception*. Lawrence Erlbaum Associates, New Jersey & London, 1986.

Francesco Ginelli and Hugues Chate. Relevance of metric-free interactions in flocking phenomena. *Physical Review Letters*, 105(16), 2010.

Ramin Golestanian. Debut of a hot fantastic voyager. *Physics*, 3:108, 2010.

Guillaume Grégoire, Hugues Chaté, and Yuhai Tu. Moving and staying together without a leader. *Physica D: Nonlinear Phenomena*, 181(34):157 – 170, 2003. ISSN 0167-2789. doi: http://dx.doi.org/10.1016/S0167-2789(03)00102-7. URL `http://www.sciencedirect.com/science/article/pii/S0167278903001027`.

Daniel Grünbaum. Translating stochastic density-dependent individual behavior with sensory constraints to an eulerian model of animal swarming. *Journal of Mathematical Biology*, 33(2):139–161, 1994. ISSN 0303-6812. doi: 10.1007/BF00160177. URL `http://dx.doi.org/10.1007/BF00160177`.

Shay Gueron and Simon A. Levin. The dynamics of group formation. *Mathematical Bioscience*, 128:243264, 1995.

W.D. Hamilton. Geometry for the selfish herd. *Journal of Theoretical Biology*, 31: 295–31, 1971.

William M Haynes. *CRC handbook of chemistry and physics*. CRC press, 2014.

Dirk Helbing and Péter Molnár. Social force model for pedestrian dynamics. *Phys. Rev. E*, 51:4282–4286, May 1995. doi: 10.1103/PhysRevE.51.4282. URL `http://link.aps.org/doi/10.1103/PhysRevE.51.4282`.

Frank H Heppner. Avian flight formation. *Bird-Banding*, 45:160 – 169, 1974a.

Frank H Heppner. Avian flight formations. *Bird-Banding*, 45:160–169, 1974b.

JJL Higdon and S Corrsin. Induced drag of a bird flock. *American Naturalist*, 112: 724–744, 1978.

H. Hildenbrand, C. Carere, and C.K. Hemelrijk. Self-organized aerial displays of thousands of starlings: a model. *Behav. Ecol.*, 21:1349–1359, 2010.

Hong-Ren Jiang, Natsuhiko Yoshinaga, and Masaki Sano. Active motion of a janus particle by self-thermophoresis in a defocused laser beam. *Physical review letters*, 105 (26):268302, 2010.

Andrew J. King, Alan M. Wilson, Simon D. Wilshin, John Lowe, Hamed Haddadi, Stephen Hailes, and A. Jennifer Morton. Selfish-herd behaviour of sheep under threat. *Current Biology*, 22(14):R561 – R562, 2012.

MF Land. Motion and vision: why animals move their eyes. *J Comp Physiol A*, 185: 341–352, 1999.

Peter F. Major and Lawrence M. Dill. The three-dimensional structure of airborne bird flocks. *Behavioral Ecology and Sociobiology*, 4(2):111–122, 1978. ISSN 0340-5443. doi: 10.1007/BF00354974. URL `http://dx.doi.org/10.1007/BF00354974`.

Graham R. Martin. The eye of a passeriform bird, the european starling (sturnus vulgaris): eye movement amplitude, visual fields and schematic optics. *Journal of Comparative Physiology A*, 159(4):545–557, 1986. ISSN 0340-7594. doi: 10.1007/BF00604174. URL `http://dx.doi.org/10.1007/BF00604174`.

A. Mogilner, L. Edelstein-Keshet, L. Bent, and A. Spiros. Mutual interactions, potentials, and individual distance in a social aggregation. *Journal of Mathematical Biology*, 47(4):353–389, 2003. ISSN 0303-6812. doi: 10.1007/s00285-003-0209-7. URL `http://dx.doi.org/10.1007/s00285-003-0209-7`.

M. E. J. Newman and G. T. Barkema. *Monte Carlo Methods in Statistical Physics*. OUP, Oxford, UK, 2010.

Julia K. Parrish, Steven v. Viscido, and Daniel Grünbaum. Self-organized fish schools: An examination of emergent properties. *The Biological Bulletin*, 202:296–305, 2002.

Daniel J. G. Pearce, Adam M. Miller, George Rowlands, and Matthew S. Turner. Role of projection in the control of bird flocks. *Proceedings of the National Academy of Sciences*, 111(29):10422–10426, 2014. doi: 10.1073/pnas.1402202111. URL `http://0-www.pnas.org.pugwash.lib.warwick.ac.uk/content/111/29/10422.abstract`.

R Piazza and A Parola. Thermophoresis in colloidal suspensions. *Journal of Physics: Condensed Matter*, 20(15):153102, 2008.

Sylvain Pion and Monique Teillaud. 3D triangulations. In *CGAL User and Reference Manual*. CGAL Editorial Board, 4.4 edition, 2014. URL `http://doc.cgal.org/4.4/Manual/packages.html#PkgTriangulation3Summary`.

Craig W. Reynolds. Flocks, herds, and schools: A distributed behavioral model. *Computer Graphics*, 21(4):25–34, 1987.

Lorrin A. Riggs, Floyd Ratliff, Janet C. Cornsweet, and Tom N. Cornsweet. The disappearance of steadily fixated visual test objects. *J. Opt. Soc. Am.*, 43:495–500, 1953.

D.J.T. Sumpter. *Collective Animal Behaviour*. Princeton University Press, New Jersey, 2010.

Alexander S. Szalay, Jim Gray, George Fekete, Peter Z. Kunszt, Peter Kukol, and Ani Thakar. Indexing the sphere with the hierarchical triangular mesh. Technical Report MSR-TR-2005-123, Microsoft Research, Advanced Technology Division, Microsoft Corporation, One Microsoft Way, Redmond, WA 98052, 2005.

Arran Tamsett, Turner Matthew, and George Rowlands. Collective self-thermophoresis with projective heating. unpublished, 2016.

Herbert G. Tanner, Ali Jadbabaie, and George J. Pappas. Stable flocking of mobile agents, part ii: Dynamic topology. In *In IEEE Conference on Decision and Control*, pages 2016–2021, 2003a.

Herbert G. Tanner, Ali Jadbabaie, and George J. Pappas. Stable flocking of mobile agents, part i: Fixed topology. In *proceedings ofthe 42nd IEEE Conference on Decision and Control, Maui, Hawaii USA*, 2003b.

J Toner and Y Tu. Flocks, herds, and schools: a quantitativetheory of flocking. *Physical Review E*, 58:48284858, 1998.

Kolbjørn Tunstrøm, Yael Katz, Christos C Ioannou, Cristián Huepe, Matthew J Lutz, and Iain D Couzin. Collective states, multistability and transitional behavior in schooling fish. *PLoS computational biology*, 9(2):e1002915, 2013.

T. Vicsek, A. Czirok, E. Ben-Jacob, I. Cohen, and O. Shochet. Novel type of phase transition in a system of self-driven particles. *Physical Review Letters*, 75(6):1226–1229, 1995.

Tamás Vicsek and Anna Zafeiris. Collective motion. *Physics Reports*, 517:71–140, 2012.

Steven V. Viscido, Matthew Miller, and David S. Wethey. The dilemma of the selfish herd: The search for a realistic movement rule. *Journal of Theoretical Biology*, 217(2): 183 – 194, 2002. ISSN 0022-5193. doi: http://dx.doi.org/10.1006/jtbi.2002.3025. URL http://www.sciencedirect.com/science/article/pii/S0022519302930250.